

POLYCRYSTALLINE CVD DIAMOND PROBES FOR USE IN *IN VIVO*  
AND *IN VITRO* NEURAL STUDIES

By  
Ho-yin Chan

A DISSERTATION

Submitted to  
Michigan State University  
In partial fulfillment of the requirements  
For the degree of

DOCTOR OF PHILOSOPHY

Electrical Engineering

2008

ABSTRACT  
POLYCRYSTALLINE CVD DIAMOND PROBES FOR USE IN *IN VIVO*  
AND *IN VITRO* NEURAL STUDIES

Microprobes are an effective analysis and stimulation tool for neural studies. Analysis can take place in one of two modes; the microprobe may be used to detect or measure chemical indicators within the brain, or, it may be used to detect electrical signals emanating from firing neurons.

A polycrystalline diamond based probe provides many potential advantages over probes of other materials. Carbon  $sp^3$  bonded diamond exhibits transparency and is a good insulator due to its large band gap (5.5 eV). Diamond is also mechanically versatile due its Young's modulus of  $\sim 10^{11}$  Pa. A boron doped diamond electrode is advantageous when compared to other electrode materials as it is resistive to fouling and chemically inert. Developing a sound design and fabrication process for the diamond probe has proven to be problematic.

In this research, the design, microfabrication and testing of a novel polycrystalline diamond (poly-C) based microprobe, for possible applications in neural prosthesis, are developed and presented for the first time. The associated poly-C micromachining technologies are also developed and discussed in depth. Two types of poly-C probes are realized, which can do electrical and electrochemical measurement. The probe utilizes undoped poly-C with a resistivity in the range of  $10^5 \Omega\text{cm}$  as a supporting material, which has a young's modulus in the range of 400 – 1,000 GPa and is biocompatible. Boron doped poly-C with a resistivity in the range of  $10^{-3} \Omega\text{cm}$  is used as an electrode material, which provides a chemically stable surface for both chemical and electrical detections in neural studies. The poly-C electrode capacitance is approximately  $87 \mu\text{F}/\text{cm}^2$ , which is

small as compared to other metal electrodes. The measured water potential window of the poly-C electrode spans across negative and positive electrode potentials and typically has a total value of 2.2 V in 1M KCl. The smallest detectable concentration of norepinephrine (a neurotransmitter) was on the order of 10 nM. The poly-C probe has also been successfully implanted in the auditory cortex area of guinea pig brain for *in vivo* neural studies. The recorded signal amplitude was 30-40  $\mu$ V and had a duration of 1ms.

## ACKNOWLEDGMENTS

I would like to thank my whole family for their patience, understanding and support during this study. I owe my greatest thanks to Skye Chan for her hard work and sacrifice.

I would like to thank my advisor, Dr. Dean Aslam, for his encouragement, guidance and financial support throughout this research. I also thank my committee members, Dr. Donnie Reinhard, Dr. Tim Hogan, Dr. George Abela and especially Dr. Kensall Wise for the advice and support. Thanks go to the members of our research group for their help and discussion in particular, Zongliang Cao, Jing Lu and Aixia Shao. Thanks also go to the faculties, staffs and friends of the WIMS center at University of Michigan who gave me great help for the probe fabrication, especially, Dr. Ying Yao, James Wiler and Brendan Casey.

## TABLE OF CONTENT

|  |    |
|--|----|
| ABSTRACT.....  | i  |
| Chapter 1 Research Motivation and Goals .....                                    | 1  |
| 1.1 Introduction .....   | 1  |
| 1.2 Microelectrodes/Microprobes .....  | 2  |
| 1.3 Objective of this Work .....   | 5  |
| 1.4 Dissertation Outline.....  | 7  |
| Chapter 2 Microprobe/Microelectrode Technologies.....                            | 8  |
| 2.1 Introduction .....   | 8  |
| 2.2 Cochlear Probes.....   | 9  |
| 2.3 Neural Probes .....  | 10 |
| 2.4 Probes for Drug and Chemical Delivery .....                                  | 14 |
| 2.5 Probes used in Electrochemical Analysis/Detections .....                     | 16 |
| 2.6 Summary .....  | 19 |
| Chapter 3 Monitoring Neural Activities using Microelectrodes .....               | 20 |
| 3.1 Introduction .....   | 20 |
| 3.2 Electrode Model .....  | 21 |
| 3.2.1 Electrical Double Layer.....   | 22 |
| 3.2.2 Electrical Model for Electrode/Electrolyte.....                            | 25 |
| 3.3 Techniques in Monitoring Neural Activities.....                              | 29 |
| 3.3.1 Electrical Recording of Action Potential.....                              | 31 |
| 3.3.2 Neurochemical Detection of Neurotransmitters.....                          | 34 |
| 3.3.3 Summary.....   | 37 |
| Chapter 4 Poly-C Micromachining Technologies Relevant to Probe Fabrication ..... | 38 |
| 4.1 Introduction .....   | 38 |
| 4.2 Properties of Polycrystalline Diamond .....                                  | 39 |
| 4.2.1 Physical and Chemical Properties of Diamond .....                          | 39 |
| 4.2.2 Biocompatibility of Diamond.....   | 41 |
| 4.2.3 Electrochemical Properties of Diamond.....                                 | 42 |
| 4.3 Poly-C Technologies .....  | 45 |
| 4.3.1 Diamond Nucleation.....  | 45 |

|   |  |     |
|---|--|-----|
| 4.3.2   | Diamond Growth and Doping .....            | 47  |
| 4.3.3   | Inadvertent SiO <sub>2</sub> Etching.....  | 49  |
| 4.3.4   | Conductivity in Undoped Poly-C Films ..... | 52  |
| 4.4   | Diamond Etching.....                       | 56  |
| 4.5   | Summary .....                              | 60  |
| Chapter 5 Poly-C Probe Technology .....                             |  | 61  |
| 5.1   | Introduction .....                         | 61  |
| 5.2   | Design.....                                | 62  |
| 5.2.1   | Electrical Neural Probe.....               | 64  |
| 5.2.2   | Electrochemical Neural Probe .....         | 66  |
| 5.3   | Fabrication.....                           | 68  |
| 5.3.1   | Electrical Neural Probe.....               | 68  |
| 5.3.2   | Electrochemical Neural Probe .....         | 73  |
| 5.4   | Probe Mounting and Packaging .....         | 77  |
| 5.5   | Summary .....                              | 78  |
| Chapter 6 Characterizations and Applications of Poly-C Probes ..... |  | 79  |
| 6.1   | Introduction .....                         | 79  |
| 6.2   | Poly-C Site Characterizations .....        | 80  |
| 6.2.1   | Electrical Impedance Spectroscopy.....     | 80  |
| 6.2.2   | Cyclic Voltammetry .....                   | 88  |
| 6.2.3   | EC Probes .....                            | 94  |
| 6.3   | Probe Applications .....                   | 97  |
| 6.3.1   | Electrical Detection .....                 | 97  |
| 6.3.2   | Electrochemical Detection.....             | 102 |
| 6.4   | Summary .....                              | 104 |
| Summary and Recommendations .....                                   |  | 106 |
| 7.1   | Summary of Contributions.....              | 106 |
| 7.2   | Future Research Areas .....                | 107 |
| APPENDIX.....   |  | 109 |
| BIBLIOGRAPHY.....   |  | 117 |

## LIST OF TABLES

|   |    |
|---|----|
| Table 2-1. Summaries of previous works on neural probes.....  | 12 |
| Table 2-2. Summary of the previous work on microprobes for drug delivery. ....  | 16 |
| Table 3-1. Concentrations of ions for mammalian skeletal muscle [85]. ....  | 33 |
| Table 4-1. Properties of silicon and diamond [82]. ....   | 40 |
| Table 4-2. Comparison of double layer capacitance and redox peak separation in 0.1M<br>KCl.....                                 | 44 |
| Table 4-3. Comparison of different seeding methods on seeding density, substrate<br>material and surface morphology [126]. .... | 46 |
| Table 4-4 Conditions for diamond growth using MPCVD.....  | 48 |
| Table 4-5. Etch rates of different types of silicon dioxide (no annealing was done after<br>growth).....                        | 51 |
| Table 4-6. Effect of boron out-diffusion from the neighborhood wafer on the diamond<br>resistivity.....                         | 55 |
| Table 4-7. Effect of process history of the MPCVD chamber on the resistivity of undoped<br>diamond.....                         | 56 |
| Table 4-8 Parameters for diamond etch.....  | 57 |
| Table 5-1. A list of the nine masks used in this project.....   | 62 |
| Table 5-2. The six masks used in the fabrication of EL probes.....  | 65 |
| Table 5-3 The eight masks used in the fabrication of electrochemical neural probes.....   | 68 |
| Table 5-4. AgCl formation on Ag electrodes using FeCl <sub>3</sub> .....  | 77 |
| Table 6-1. Fitted parameters for electrode/electrolyte model.....   | 88 |

## LIST OF FIGURES

|  |    |
|--|----|
| Figure 1-1. An overview of poly-C neural probe technology for neural recording.....  | 6  |
| Figure 2-1. Fabrication process (left) and images (right) of the cochlear probes.....  | 10 |
| Figure 2-2. Schematic of the pathway of information flow for the cognitive-based neural<br>prosthetic paradigm (left) and filtered neural data recorded from a single channel of the<br>probe in a rat's cortex (right). ..... | 11 |
| Figure 2-3. Different types of neural probes: (a) Planar (b) Three dimensional. ....   | 12 |
| Figure 2-4. Fabrication process and images of the microneedles.....  | 15 |
| Figure 2-5. Neural probes with stimulation sites and microchannels.....  | 15 |
| Figure 2-6. Carbon fiber electrode for electrochemical detection. ....   | 17 |
| Figure 2-7. Cyclic voltammetry of the electrodes in 0.5M H <sub>2</sub> SO <sub>4</sub> (a, b) polycrystalline<br>diamond, (c) platinum and (d) highly oriented pyrographite.....  | 18 |
| Figure 2-8. A diamond microprobe with tungsten connected wire [80].....  | 19 |
| Figure 3-1. A typical electrochemical cell which has two electrodes.....   | 22 |
| Figure 3-2. A systematic representation of the double layer structure. ....  | 24 |
| Figure 3-3. Randles' equivalent circuit for the electrode/electrolyte interface. ....  | 26 |
| Figure 3-4. A typical Nyquist plot for the Randles model in both high and low<br>frequencies. ....   | 27 |
| Figure 3-5. Low frequency model of an electrode/electrolyte interface.....   | 28 |
| Figure 3-6. High frequency model of an electrode/electrolyte interface.....  | 29 |
| Figure 3-7. A schematic of a neuron.....   | 30 |
| Figure 3-8. A schematic of the synapse.....  | 30 |
| Figure 3-9. A typical example of an action potential [86].....   | 31 |

|   |    |
|---|----|
| Figure 3-10. A triangular potential waveform used in cyclic voltammetry [68].   | 36 |
| Figure 3-11. A typical cyclic voltammogram [68].  | 36 |
| Figure 4-1. Cyclic voltammograms of diamond films with different C/H source gas mixtures in 0.1M HClO <sub>4</sub> .  | 43 |
| Figure 4-2. Capacitance-potential profiles of GC, HGC, HOPG and diamond in 0.1M HClO <sub>4</sub> .   | 44 |
| Figure 4-3. Seed distribution on (a) a non-treated and (b) an RCA-treated Si surface.   | 47 |
| Figure 4-4. Schematic of the MPCVD system used in this project.   | 48 |
| Figure 4-5. (a) An SEM image of a poly-C surface and (b) its Raman spectrum.  | 49 |
| Figure 4-6. The relationships between the seeding density and time $t_c$ as a function of seeding spin rate.  | 51 |
| Figure 4-7. Diamond seeding density on RCA treated Si surface with different spin rates (the samples have been undergone 40 mins diamond growth).             | 52 |
| Figure 4-8. Schematics of an experimental setup for showing boron-out diffusion from Si substrate in the MPCVD chamber.                                       | 54 |
| Figure 4-9. SEM images of the diamond surface at different stages of the etching process. The bar shown on the lower right corner of each image is 2 $\mu$ m. | 58 |
| Figure 4-10. A rough Si surface which has been over etched caused by CF <sub>4</sub> in the diamond etching recipe.   | 59 |
| Figure 4-11. The diamond sample patterned using 2 step etching. Oxide layer is well protected and its roughness is only 20-30 $\text{\AA}$ .                  | 59 |
| Figure 5-1. Mask layout for different types of diamond probes.  | 63 |
| Figure 5-2. Design of the EL probe.   | 65 |

|   |    |
|---|----|
| Figure 5-3. Design of the EC probe.....   | 67 |
| Figure 5-4. Fabrication process of all-diamond probes.....  | 70 |
| Figure 5-5. Released all-diamond probe on a US penny. The highly doped Si back end was removed in this probe.....   | 71 |
| Figure 5-6. An all-diamond probe was bent in the out-of-plane direction with a pair of tweezers (bending angle was larger than 180°).....   | 72 |
| Figure 5-7. Fabrication process of the EC probe.....  | 74 |
| Figure 5-8. (a) A fabricated EC probe, which has an (b) Au counter electrodes, (c) Ag/AgCl reference electrodes and a (d) poly-C working electrodes.....  | 75 |
| Figure 5-9. Probe mounting.....   | 78 |
| Figure 6-1. Modified Randles model of the electrode/electrolyte interface [85]. .....   | 83 |
| Figure 6-2. Experimental setup for the EIS measurements.....  | 84 |
| Figure 6-3. Impedance spectrum for a diamond electrode with diameter of 30 $\mu\text{m}$ , (a) Nyquist plot of the real and imaginary part of the measured impedance, (b) Bode plot..   | 87 |
| Figure 6-4. Experimental setup for cyclic voltammetry.....  | 89 |
| Figure 6-5. Voltammograms of Au, Pt, IrOx and diamond electrodes in (a) 1MKCl, (b) Krebs, and (c) PBS.....  | 91 |
| Figure 6-6. Cyclic voltammetry current-voltage curve for the diamond probe in 1M KCl. The insert is the CV of the diamond probe in 1 mM $\text{Fe}(\text{CN})_6^{-4}$ in 1M KCl. The scan rate was 100 mV/s. The reference and counter electrodes are Ag/AgCl and platinum, respectively..... | 93 |
| Figure 6-7. A comparison on the cyclic voltammograms in 1M KCl.....   | 95 |
| Figure 6-8. Cyclic voltammograms of the EC probe in 1mM $\text{Fe}(\text{CN})_6^{-3/4}$ + 1M KCl.....   | 96 |

|  |     |
|--|-----|
| Figure 6-9. Acute recording of neural activity using the diamond probe. ....   | 98  |
| Figure 6-10. (a) Recorded neural activity in guinea pig's auditory cortex using the diamond probe with an electrode area of $100\mu\text{m}^2$ , (b) A recorded neural spike. ....                                       | 99  |
| Figure 6-11. A recorded in vivo signal from an all-diamond EL probe. ....  | 101 |
| Figure 6-12. Histograms of the recorded neural signals shown in previous figure. ....  | 101 |
| Figure 6-13. Measured cyclic voltammograms of the poly-C probe for different concentrations of NE in Krebs buffer solution using a scan rate of 100 mV/s. The inset shows the background current in Krebs solution. .... | 103 |
| Figure 6-14. Detection of NE and DA with same concentration. ....  | 104 |

# Chapter 1

## Research Motivation and Goals

### 1.1 Introduction

The study of cellular function and response has been used for decades to better understand the principles of human body function in order to prevent, treat or cure diseases in an effective way. Among all the parts of a human body, the human brain is the core and is also the most complex as it contains an incredibly large amount of neurons. These neurons control body movement, human emotion, reaction, thinking and etc. Due to its complexity, it contains many long-standing mysteries which are of interest to neuroscientists [1]. For instance, it is not yet known how information is encoded in the brain, what emotions really are, or how memories are stored and retrieved. The exploration and understanding of the brain require the study of neural activities and how these signals correlate to human reactions. Thus, it is highly desired to have a way to interact with the human brain in order to extract information from it. As technology continues to advance, the capabilities and sensitivity of cellular studies have greatly improved. Current techniques allow for the examination of a single cell's electrical characteristics either *in vivo* (within the body) or *in vitro* (outside of the body) using glass micropipettes or wire microelectrodes [2]. These tools are able to detect electrical signals and detect chemicals electrochemically.

## 1.2 Microelectrodes/Microprobes

One of the key components in neural prosthetic systems is the microelectrode/microprobe, which interfaces with neurons in order to record electrical signals or detect the presence of a particular chemical. Microprobes can also be used for stimulation. In early *in vivo* studies, metal wires coated with insulating materials [3] were used as electrodes, which are associated with limited spatial resolution. In the late 1960s, microprobes with multiple recording or stimulation sites were fabricated on microprobes with high reproducibility utilizing lithographic thin-film techniques [3]. With the development of Micro-Electro-Mechanical Systems (MEMS) technologies, sophisticated microprobes with electrode arrays have been developed and are now widely used in neural activity studies [4][5][6][7], drug delivery [8][9], and cochlear implants [10][11]. 3D microprobe arrays have been fabricated, microassembled and integrated with a hybrid application specific integrated circuit (ASIC) chip. [12]. Most of today's probes are made out of silicon due to the fact that silicon based bulk micromachining technology is well developed. The silicon microprobes are either fabricated on bulk silicon or silicon on insulator (SOI) wafers. In the former case, highly boron doped silicon is used as the etch stop in the ethylenediamine pyrocatecol (EDP) or Tetramethylammonium hydroxide (TMAH) etching process to release the probe structure. The oxide layer of the silicon on insulator (SOI) wafer is used as the etch stop in deep reactive ion etching (DRIE) for probe release. Due to the biocompatibility and flexibility issues associated with Si probes, recently, researchers have been studying the use of other materials in probe fabrication. For example, parylene C [13][14][15], polyimide [16] and SU-8 [17] are often used as materials for the probe's substrate or for coating.

The most important component on the microprobes is the metal site, which is used for signal recording and electrical stimulation. Commonly used site materials include platinum [18], gold [19], titanium nitride [20] and iridium oxide [21]. The sites should be inert and chemically stable in the working environment-especially in ion- and protein-rich conditions. Otherwise, the corresponding background noise would be too high, or the target signal could be suppressed due to site blocking caused by residues formed or absorbed on the site surface. For stimulation, the electrode should have a large charge storage capacity as well as a large charge delivery capacity in order to deliver a large amount of charge to a small geometric area. Sites for recording, on the other hand, should be associated with relatively low background noise in order to achieve a high signal to noise ratio. The exposed site area should be large for collecting a greater number of signals in the case of electrical recording. Also, thermal noise is reduced because of the low impedance of larger sites [22], but the selectivity (i.e. the ability to discriminate between signals from different neurons) would be low. Thus, the signal received by the probe would be from multiple units but not from isolated unit, which is undesirable. On the contrary, in electrochemical recording, the site area as well as the double layer capacitance must be small in order to minimize non-Faradic currents. These currents are usually caused by the charging of the double layer structure formed at the electrode/electrolyte interface. Therefore, in order to have a good signal to noise ratio ( $>3$ ), the electrode should have low capacitance. The electrode should also exhibit a wide water potential window (potential range in which there is no current caused by oxygen or hydrogen evolution). Carbon fiber [23] is one of the most promising materials for electrochemical detection as it has most of the characteristics mentioned above. However,

one of the main disadvantages of carbon fiber is its fouling which requires constant surface polishing.

In this study, polycrystalline diamond (poly-C) is chosen as the core material in the microprobe due to its unique properties. The presence of unique  $sp^3$  C-C bonds in the diamond lattice leads to its unique mechanical properties (large Young's modulus,  $\sim 10^{11}$  Pa). Poly-C also has a large band gap (5.5 eV) which makes it a good insulating and optically transparent material [24]. The optical transparency of the diamond substrate is important for *in vitro* experiment because it allows the electrode's position on the probe to be easily located under a microscope. In addition, the comparatively wide potential window (the reported values range from 1.4 to 4 V) in an aqueous environment [25][26][27][28], low double layer capacitance (ranging from 5 to 40  $\mu\text{F}/\text{cm}^2$ ) [29], chemical inertness and stability, resistance to fouling of boron doped diamond make it an excellent site material for microprobes [25]. The biocompatibility of diamond surfaces has been studied intensively based on protein adsorption of chemical-vapor-deposited (CVD) diamond [30] and diamond-like carbon (DLC), and cellular responses to each [31]. It is found that CVD diamond absorbed and denatured relatively small amounts of fibrinogen which is commonly used as a biocompatibility indicator, and no cytotoxicity was seen, which is an inflammatory reaction and has adverse effects on cells [32]. In electrochemistry, researchers have extensively studied boron-doped diamond as an electrode material [33][34]. The previously existing boron doped poly-C electrodes, which are used in neural studies [35][36], were fabricated by depositing diamond on the tip of a wire. These electrodes display limited spatial resolution for studying brain

activities. Recently, poly-C sensors and electrodes were integrated in Si cochlear microprobes for the first time [11].

### 1.3 Objective of this Work

An overview of the work done in this project is shown in Figure 1-1. The focus of the current work is to integrate polycrystalline diamond thin films into microprobe fabrication to develop a novel all-diamond probe for neural and biomedical applications. The fabricated all-diamond probes with diamond electrodes would be used for chemical detection (as conductive diamond has a wide potential window) and electrical sensing in biological environments (as diamond chemical inertness is advantageous). For such measurements, a neural probe having precisely positioned arrays of electrodes with micrometer and nanometer dimensions, are needed.

The works addressed the following issues:

- 1) Development of the process for integrating undoped and doped diamond as the probe substrate, and interconnects and electrode/site, respectively.
- 2) Design and fabrication of all-diamond neural probes using silicon existing surface micromachining technologies.
- 3) Design and fabrication of diamond based probes which include sets of three electrode configurations for electrochemical analysis
- 4) Application of the fabricated diamond probes in electrochemical and electrical measurements in neural studies.

Successful accomplishment of these goals is expected to lead to the following unique contributions:

- 1) First fabrication of diamond probes with diamond electrodes, substrate and interconnects in a microprobe structure.
- 2) First fabrication of diamond probes with counter, working and reference electrodes on a single probe
- 3) First application of a diamond probe in neural recording.

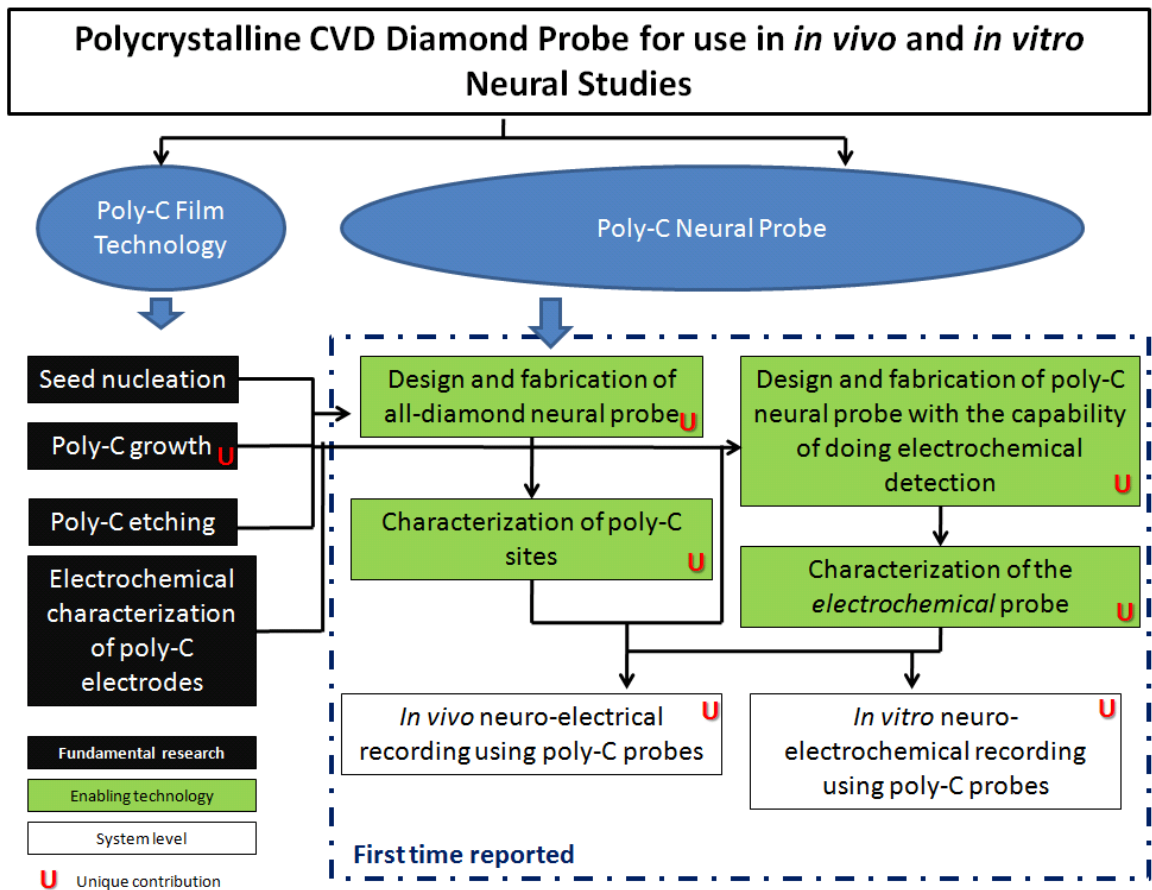


Figure 1-1. An overview of poly-C neural probe technology for neural recording.

## 1.4 Dissertation Outline

This thesis presents the development and characterization of poly-C neural microprobes for neural prosthesis. A literature review on the current microprobe/microelectrode technologies is discussed in Chapter 2. The work on microprobes, which include cochlear, neural and electrochemical probes, are presented and summarized. The key component of these probes is the electrode/site, which is used for stimulation and recording. Thus, an electrode model for an electrode/electrolyte interface is presented in chapter 3, which aids in understanding reactions taking place at the electrode surface. As the focus of this research is to utilize poly-C electrodes for *in vivo* and *in vitro* recording, methods useful in neural recording are also discussed in chapter 3.

All of the work performed in this study is presented in chapters 4, 5 and 6. In chapter 4, poly-C micromachining technologies relevant to probe fabrication are presented, which include diamond nucleation, growth, doping and patterning. In chapter 5, the design and fabrication of two types of novel poly-C probes are presented. The two types include electrical (EL) and electrochemical (EC) probes. Then, the characterization and applications of these two types of poly-C probes are presented in chapter 6. Finally, a summary on the work done and also recommendations for future related research are included in chapter 7.

# Chapter 2

## Microprobe/Microelectrode Technologies

### 2.1 Introduction

Microprobes, sometimes called microelectrodes, have been widely used in chemical and biomedical applications. Depending on the particular applications, microprobes can be involved in chemical or electrical sensing, electrical stimulation or chemical delivery. Microprobes are crucial in any of these aspects because they interface with biological entities (in biochemical applications) and target species (in electrochemistry applications). They are most commonly used in the recording of electrical signals which are associated with reduction-oxidation (redox) reactions involving analytes or action potentials in the brain. Some of them even have the ability to deliver chemicals in order to stimulate cells or aid in healing applications. Most of today's microprobes are made of silicon as silicon lends itself to on-probe CMOS development. Also, processes for surface micromachining of silicon are well-developed. The silicon probes are fabricated using either an ethylenediamine pyrocatechol (EDP) silicon etching process with a deep boron etch stop [37] or a DRIE etch of SOI wafers [38]. Such probes are widely used in biomedical applications for neural simulation, neural activity recording and drug delivery. Microprobes used in electrochemical aspects are simply metal wires coated with a layer of insulator. In this chapter, a brief introduction to various types of microprobes used in both biomedical applications and

electrochemistry is presented. It also highlights the structure of various probes and the materials used for the probes.

## 2.2 Cochlear Probes

Researchers at the University of Michigan have been actively researching the fabrication and design of many different types of microprobes. Prof. K. D. Wise's group has demonstrated the use of microprobes for cochlear prosthesis [37][39]. In cochlear prosthesis, the probe is implanted in the ear in an effort to recover the hearing ability of deaf people. The microprobe, shown in Figure 2-1, was fabricated on a silicon wafer and includes stimulation sites and position sensors. The position sensors on the probe retrieve the shape of the inserted microprobe and the electrodes are used for sending electrical pulses to nerves inside the ear. The probe shaft is defined by boron doped silicon which acted as an etch stop in an EPD process. The probe was around 1.6cm long and 6 $\mu$ m thick. Dr. Yuxing Tang, a member of our group, has integrated polycrystalline diamond (poly-C) strain sensors on the probes which have a higher gauge factor (GF) as compared to those made of polysilicon [40]. However, these probes suffer from two problems. First, silicon is not a biocompatible material—it may perturb cellular environments. Therefore, the probe has to be passivated with silicon dioxide or coated with polymers before insertion. Secondly, the stiffness of the probe limits its flexibility which can cause problems during insertion. Thus, the designs of the probes were modified to rings or ribs substrate. Also in response to the problems outlined above, C. Pang et al have encapsulated probes in parylene so as to increase their flexibility and biocompatibility [41].

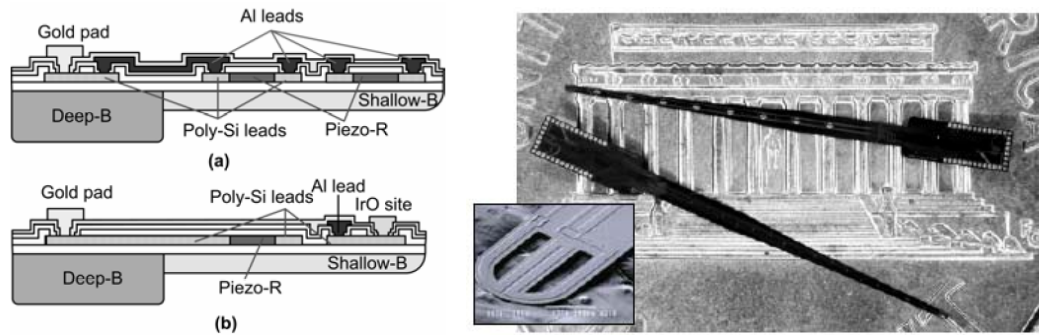


Figure 2-1. Fabrication process (left) and images (right) of the cochlear probes.

## 2.3 Neural Probes

The design and fabrication processes of neural probes must focus minimization of insertion damage, reduction of tissue reactive responses and minimization of perturbing cellular environment. Therefore, the probe's size, material construction and the technique used to package the probe are important. Current probes used in neural prosthesis contain several metal sites for recording neural signals. The process by which these signals are generated and recorded is described in Figure 2-2. There are numerous groups that have been working on the design and fabrication of neural probes [42][43][44][45][46][47][48][49][50][51][52][53][54][55]. T. A. Kovacs et al has briefly summarized the early work on microelectrode arrays for neural recording and stimulation [56].

Table 2-1 summarizes the recent works on neural probes. It is found that silicon is often chosen probe substrate material over the past 10 years. Recently, researchers have been looking for other probe materials and fabrication techniques which could overcome some of the limitations associated with silicon probes. For example, probes made from

polyimide can be very flexible which is critical during insertion. On the other hand, using electroplating technology, probes can be fabricated such that its thickness varies along its length; this increases the stiffness of the probe so that the probe will not break easily. It is seen that, depending on different applications, probes can be in different forms and make use of different substrate materials. However, the materials used in fabricating electrodes are similar in most all probes. Commonly used materials include platinum, gold and iridium because of their associated chemical stability and inertness.

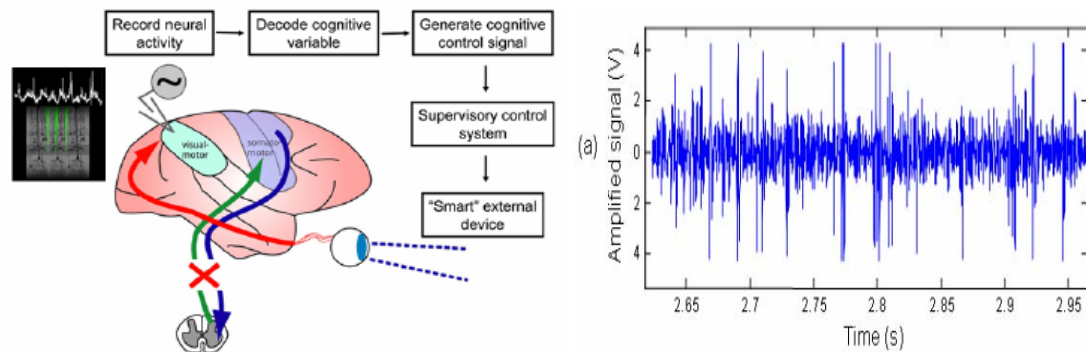


Figure 2-2. Schematic of the pathway of information flow for the cognitive-based neural prosthetic paradigm (left) and filtered neural data recorded from a single channel of the probe in a rat's cortex (right).

A typical design of a neural probe array is shown in Figure 2-3 (a). It consists of several probes each having its own recording site located at the tip of the probe. These arrays provide the ability to record neural signals from various points. Figure 2-3 (b) shows another design of a three dimensional probe array. This probe array provides 3-D spatial resolution.

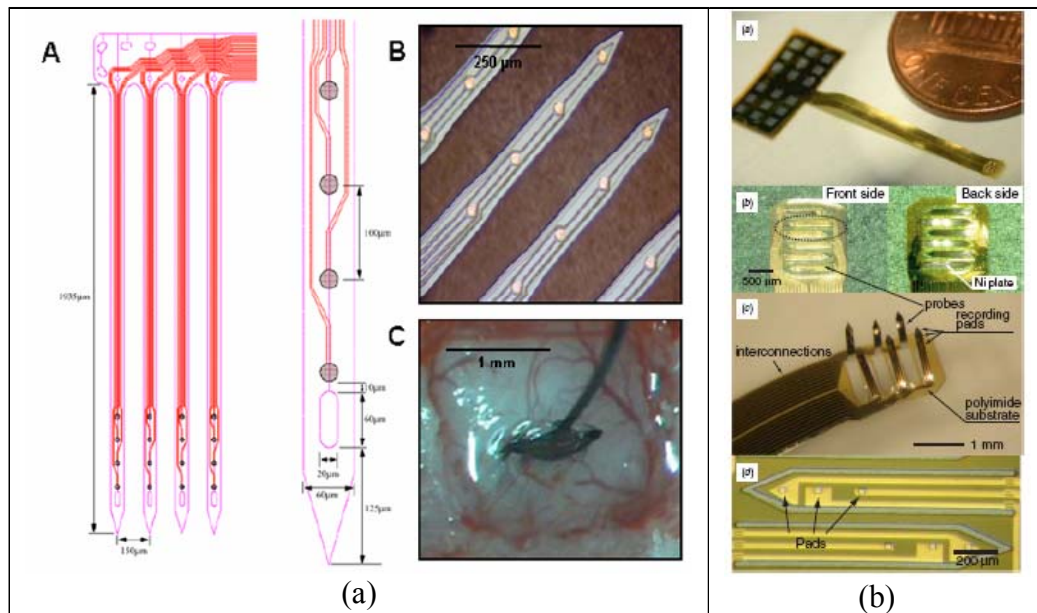


Figure 2-3. Different types of neural probes: (a) Planar (b) Three dimensional.

Table 2-1. Summaries of previous works on neural probes.

| Researchers                                  | Substrate material(s)  | Electrode material(s) | Probe dimensions          | Applications   |
|--|------------------------|-----------------------|---------------------------|--|
| P. K. Campbell et al (U. of Utah, 1991) [46] | Silicon (multi probes) | Au                    | L=1.5mm                   | Electrical recording,  |
| J. H. M. Put et la (Netherlands, 1991) [49]  | Silicon (multi probes) | Pt (10μm x 505μm)     | L=1mm<br>T=45μm           | Electrical stimulation   |
| G. T. A Kovacs et al (Stanford, 1996) [50]   | Silicon (multi-probes) | Cr/Ir                 | L=1mm<br>W=30μm<br>T=25μm | Electrical sensing of the cerebral cortex of an anesthetized rat |
| L. P. Lee et al (UCB, 2000) [51]             | Silicon (multit-probe) | Pt                    | T=25μm                    | Electrical simulation and recording                              |

|  |   |   |   |   |
|--|---|---|---|---|
| S. J. Kim et al<br>(Korea, 2000)<br>[48]                     | Silicon<br>(multi probes)               | Cr/Au   | L=1mm<br>W=100 $\mu$ m<br>T=30 $\mu$ m  | Recording<br>action<br>potentials in rat<br>cortex  |
| P. Norlin et al<br>(Germany, 2003)<br>[45]                   | SOI<br>(multi-probes)                   | Ti/Ir and Ti/Pt<br>(10 $\mu$ m x 10<br>$\mu$ m) | L=1.6mm<br>W=50 $\mu$ m                 | Electrical<br>sensing   |
| H. Fujita et al<br>(Japan, 2004)<br>[42]                     | Polyimide<br>(3D multi<br>probes)       | Ti/Al   | L=1.2mm<br>W=160 $\mu$ m<br>T=5 $\mu$ m | Action<br>potentials<br>recording in<br>rat's visual<br>cortex                                    |
| C. Pang et al<br>(Caltech, 2005)<br>[41]                     | Silicon/parylene<br>C<br>(multi probes) | Ti/Pt   | L=4mm<br>W=45 $\mu$ m<br>T=50 $\mu$ m   | Electrical<br>Neural<br>recording   |
| D. R. Kipke et al<br>(U. of Mich.,<br>2005) [43]<br>[57][58] | Silicon<br>(multi probes)               | Pt, IrOx<br>(D=20 $\mu$ m)                      | L=2mm<br>W=60 $\mu$ m                   | Rat brain<br>cortical neural<br>signal<br>recording and<br>neurochemical<br>sensing<br>(dopamine) |
| J. W. Judy et al<br>(UCLA, 2005)<br>[52]                     | Electroplated Ni<br>(single probe)      | Cr/Pt   | L=22mm<br>T=50 $\mu$ m                  | Deep-brain<br>simulation  |
| W. C. Tang et al<br>(UCI, 2005) [53]                         | Silicon<br>(multi probes)               | Ir  | L=750 $\mu$ m                           | Electrical<br>neural<br>recording   |
| S. H. Cho et al<br>(U. of Texas at<br>Dallas, 2006)<br>[59]  | SU-8<br>(Single probe)                  | Au<br>(D=15 $\mu$ m)                            | L=5mm,<br>W=240 $\mu$ m                 | Electrical<br>recording   |
| Y. Kato et al<br>(U. of Tokyo,<br>2006) [60]                 | Parylene C<br>(Single probe)            | Au<br>(D=20 $\mu$ m)                            | L=3.7 mm,<br>W= 554 $\mu$ m             | Electrical<br>recording and<br>chemical<br>delivery   |

|  |         |  |              |                      |
|--|---------|--|--------------|----------------------|
| J. C. Sanchez et al (U. of Florida, 2006) [61] |         | Polyimide coated tungsten/Au (D=50 $\mu\text{m}$ ) | L=1.6mm      | Electrical recording |
| P. Ruther et al (U. of Freiburg, 2007) [62]    | Silicon | Pt   | L=4mm or 8mm | Electrical recording |

## 2.4 Probes for Drug and Chemical Delivery

In neural activity studies, it is sometimes not just interacting with neurons electrically but also chemically stimulating neurons in order to understand the complex reactions happened inside the brain. Therefore, there are probes which are specially outfitted with embedded microchannels for chemicals delivery. These probes are often called microneedles or microcapillaries [63][64][65][66] and are summarized in Table 2-2. Figure 2-4 shows an example of a fabricated microneedle, which is made of boron doped silicon (12 $\mu\text{m}$ ) and silicon nitride (1 $\mu\text{m}$ ) [64]. Silicon dioxide (8 $\mu\text{m}$ ) was used as the sacrificial layer which was covered by silicon nitride. Numerous etch holes were opened on the nitride surface for sacrificial layer etching. Then, the etch holes were sealed by depositing silicon nitride (1.5 $\mu\text{m}$ ) again.

A sophisticated microprobe reported by J. Chen et al [63] contains both stimulation sites (made of Titanium/Iridium) and microchannels (made of silicon) as shown in Figure 2-5. As mentioned earlier in this section, the delivery capability of microprobes allows scientists to study complex chemical reaction inside neural systems. This probe was used to deliver both kainic acid (a neural stimulant) and  $\gamma$ -aminobutyric acid (a neural depressant) into guinea pig brains *in vivo*.

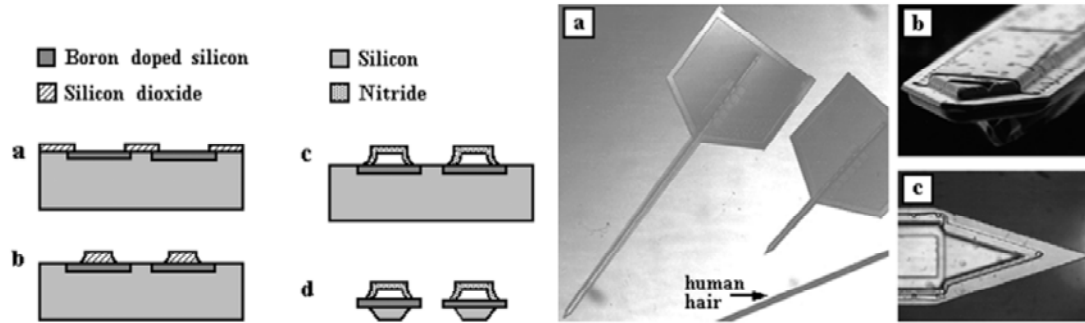


Figure 2-4. Fabrication process and images of the microneedles.

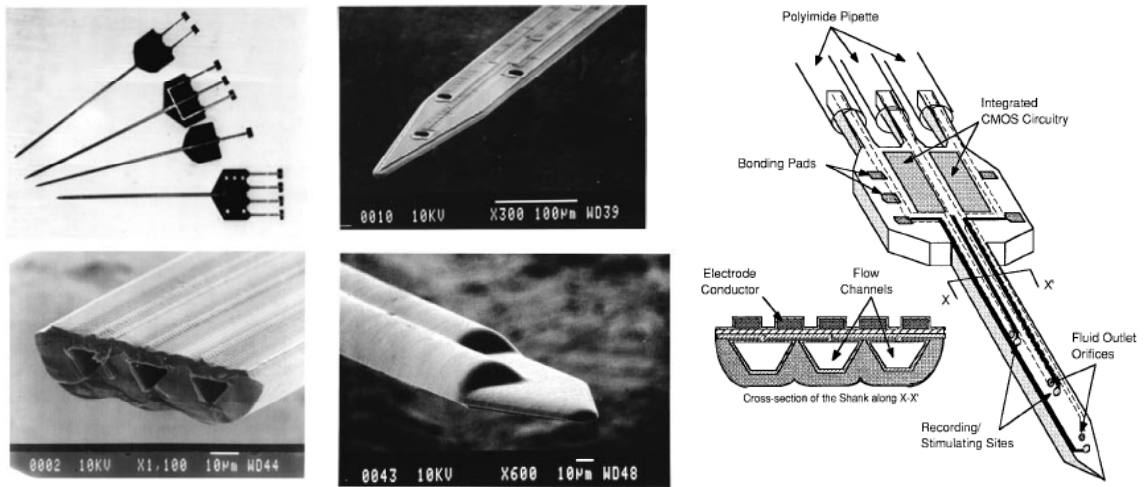


Figure 2-5. Neural probes with stimulation sites and microchannels.

Table 2-2. Summary of the previous work on microprobes for drug delivery.

| Researchers                                   | Substrate material(s) | Channel dimensions and materials                               | Probe dimensions | Applications                                   |
|---|-----------------------|--|------------------|--|
| K.D.Wise et al (U. of Mich, 1994) [63]        | Silicon               | W=10-32 $\mu\text{m}$<br>H=15 $\mu\text{m}$<br>Silicon         | L=4mm            | deliver kainic and $\gamma$ -aminobutyric acid |
| A. B. Frazier et al (Georgia Tech, 1998) [66] | -                     | Palladium<br>H=20 $\mu\text{m}$<br>W=40 $\mu\text{m}$          | L=3mm            | Injection                                      |
| A. P. Pisano et la (UCB, 1999) [65]           | Silicon               | Silicon and nitride<br>W=50 $\mu\text{m}$<br>H=9 $\mu\text{m}$ | L=1-6mm          | Injection                                      |

## 2.5 Probes used in Electrochemical Analysis/Detections

Probes or electrodes are used in electrochemical manner for analytical purposes such as environments monitoring, industrial quality control and biomedical analysis. These applications require electron transfer between electrolytes and electrodes through redox reaction processes [67][68]. Therefore, electrodes must be resistant to fouling. The designs of probes or electrodes used in electrochemistry are simple as compared to MEMS-based microprobes. They are generally thin metal wires coated with insulating materials such as glass. As mentioned in [68], glassy carbon and carbon fiber are the

most common insulating materials used as shown in Figure 2-6. Carbon electrodes are desirable because of their low cost, simplicity of preparation, the possibility of achieving large surface area and a relatively wide potential window of water and their high degree of stability as compared to metal materials [69]. However, electrode fouling limits their long term stability and leads to a need to frequently polish or dispose of the electrode after only a few uses. Thus, diamond, another form of carbon has drawn the attention of researchers because of its extreme chemical stability [70] and resistance to fouling [71][72]. In addition, diamond electrodes exhibit a comparatively wide potential window ([73][74]) for oxygen and hydrogen evolutions (-1.25V to +2.3V vs NHE) as shown in Figure 2-7. This allows us to analyze species (e.g., persulfate ion [75]) which cannot be analyzed using conventional metal electrodes.

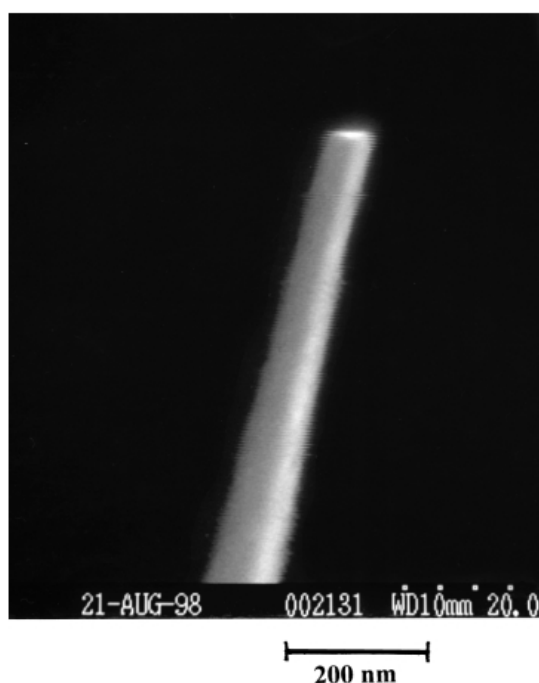


Figure 2-6. Carbon fiber electrode for electrochemical detection.

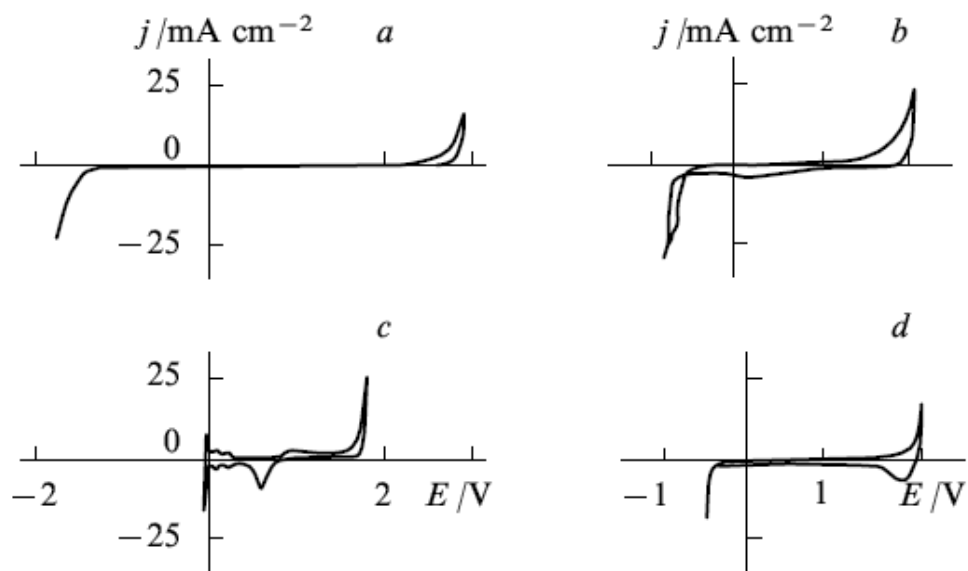


Figure 2-7. Cyclic voltammetry of the electrodes in 0.5M H<sub>2</sub>SO<sub>4</sub> (a, b) polycrystalline diamond, (c) platinum and (d) highly oriented pyrographite.

Several groups have reported using boron-doped diamond as an electrode material for electrochemical detection [76], waste treatment [68], *in vivo* detection of serotonin [77][78] and adenosine [79] and neurodynamic studies [80]. An example of a boron-doped diamond probe used in electrochemistry is shown in Figure 2-8. A tungsten wire was encapsulated by a quartz tube and boron-doped diamond was growth at the tube end using microwave plasma assisted chemical vapor deposition (MPCVD). The diameter of the tube end was around 35 $\mu$ m which is useful for precision *in vivo* detection. Owing to the small effective area of the exposed electrode, the *iR* drop in the electrolyte and the changing capacitive current of the electrode-electrolyte interface, which is undesirable, are small.

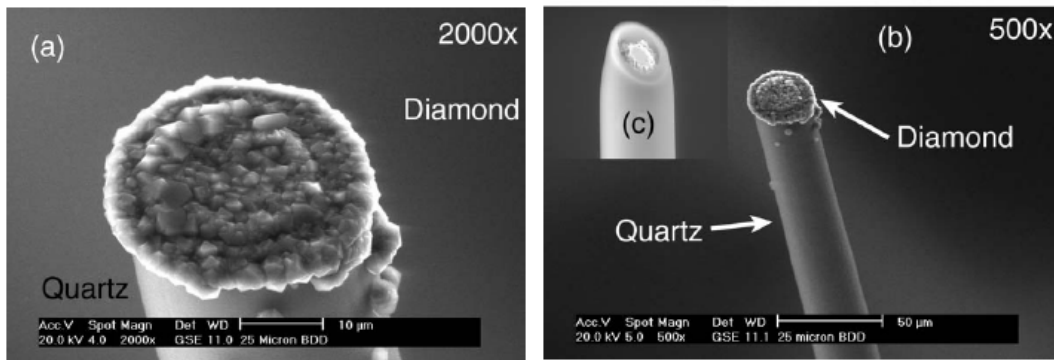


Figure 2-8. A diamond microprobe with tungsten connected wire [80].

## 2.6 Summary

This chapter reviews previous work done on various types of microprobes. Most of the microprobes are made of silicon. The commonly used electrode materials are Pt, Au, TiN and IrO<sub>x</sub>, which can be used either for stimulation or recording. In electrochemistry, the commonly used electrodes are carbon fiber and diamond coated microelectrode. It is found that diamond electrodes are advantageous in chemical detection and analysis because of their chemical inertness and stability. However, to date, there is no integration of diamond electrodes with microprobe fabrication with the exception diamond piezoresistors. The integration of diamond electrodes on a probe will lead to promising applications in both *in vivo* and *in vitro* neural recording.

# Chapter 3

## Monitoring Neural Activities Using

### Microelectrodes

#### 3.1 Introduction

In the first part of this chapter, a review of the electrochemical processes taking place at electrode surfaces when an electrode is immersed in an electrolyte is presented. The behavior of the electrochemical system can be represented by an equivalent circuit consisting of a combination of resistors and capacitors. The model parameters in the circuit can be extracted indirectly by Electrical Impedance Spectroscopy (EIS), which is commonly used to characterize the electrode behavior for small perturbations and high frequency excitations.

In the second part of this chapter, techniques used to monitoring neural activities are discussed. These techniques can be classified into two categories: non-invasive and invasive recording [81]. Non-invasive recording modalities, including functional magnetic resonance imaging (fMRI), electroencephalograms (EEG) and magnetoencephalograms (MEG), can provide most of current data from the brain. However, the data returned from these techniques lack the spatial resolution required to understand physiological processes at the cellular level. On the contrary, the development

of invasive recording allows us to retrieve information down to the cellular level (i.e. local field potential or even action potential generated by a single neuron). In addition, recent advances in micromachining technology have made real-time multichannel monitoring of cellular and molecular dynamics possible both *in vitro* and *in vivo*. Numerous research groups have been working on cell cultures *in vitro* using devices which have single or multi planar electrodes [82][83][84]. These devices have the capability to measure the action potential and impedance of the target cells. Microprobes, on the other hand, allow us to retrieve data from the brain *in vivo*. In summary, in this chapter, two possible ways of neural recording are discussed which include recording of action potential and neurochemical release.

## 3.2 Electrode Model

In an electrochemical system, or any measurement system involving the use of electrodes, there must be at least two electrodes in order to complete the circuit as shown in Figure 3-1. Charge can then be transferred by electrons (in the electrode and external circuit) and by ions (in the electrolyte). At the electrode/electrolyte interface, there are two types of processes which can occur. One of them involves the charge transfer across the electrode/electrolyte interface; this type of process is called a Faradaic process. The other type, a non-Faradaic process, does not involve charge transfer across the interface. For example, adsorption or desorption phenomena. As there are different processes taking place at the electrode/electrolyte interface, an electrical model of the situation

should be developed in order to gain a thorough understanding of the interface and relevant processes.

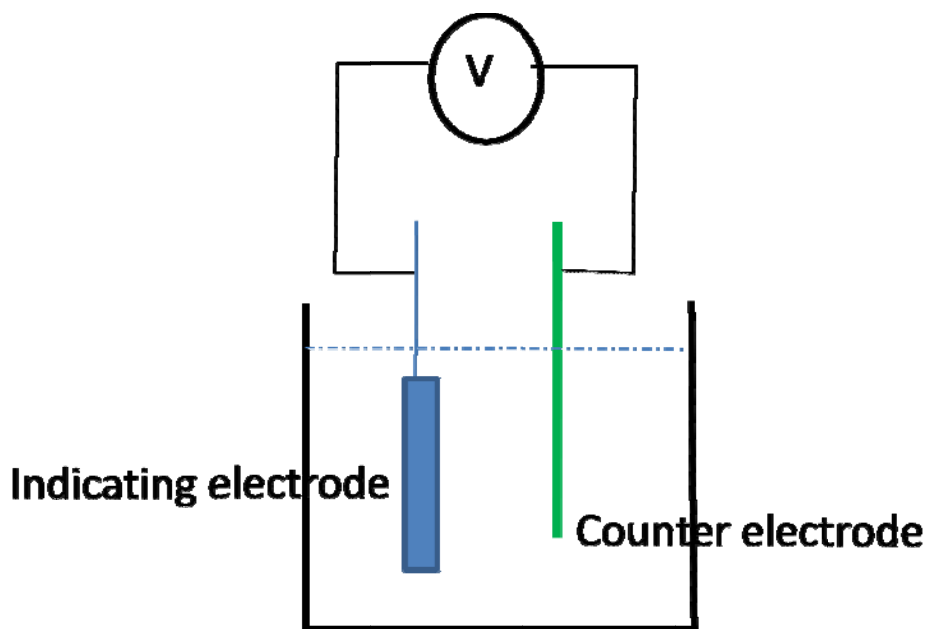


Figure 3-1. A typical electrochemical cell which has two electrodes.

### 3.2.1 Electrical Double Layer

When an electrode is immersed in an electrolyte, an electrical double layer must be formed before any charge may move across the electrode/electrolyte interface. The structure of the electrical double layer formed is shown in Figure 3-2. For a given applied potential, and before any charge can move across the interface, the total charge on the electrode ( $-q^M$ ) and in the solution ( $q^S$ ) must be equal but opposite in magnitude in order to maintain charge neutrality. This region of charge separation is called space charge region.

The region next to the electrode surface (moving away from the electrode) is made of solvent molecules (e.g. water) or adsorbed species. The water dipoles orient

themselves according to an electric field developed across the interface caused by the double layer formed. This layer of dipoles is called the inner Helmholtz plane (IHP). The next layer towards the electrolyte is called the outer Helmholtz plane (OHP), or, sometimes, the plane of closest approach (PCA). This plane defines the nearest locus of centers of solvated ions. These ions, called nonspecifically adsorbed ions, are those which undergo electron exchange with the electrode. The distance of this plane from the electrode surface is  $\sim 10\text{\AA}$ . These nonspecifically adsorbed ions are distributed and extend into the bulk solution. This layer is called the diffuse layer. The thickness of the electrical double layer grows as the time. A typical thickness in the time scale (reaction time) of 1s is  $\sim 30\mu\text{m}$ . Since the cations are mostly concentrated at the OHP, the potential drop occurs mostly across the electrode and OHP. Therefore, when this double layer structure is formed, a large potential field develops at the interface which drives the electron transfer across it.

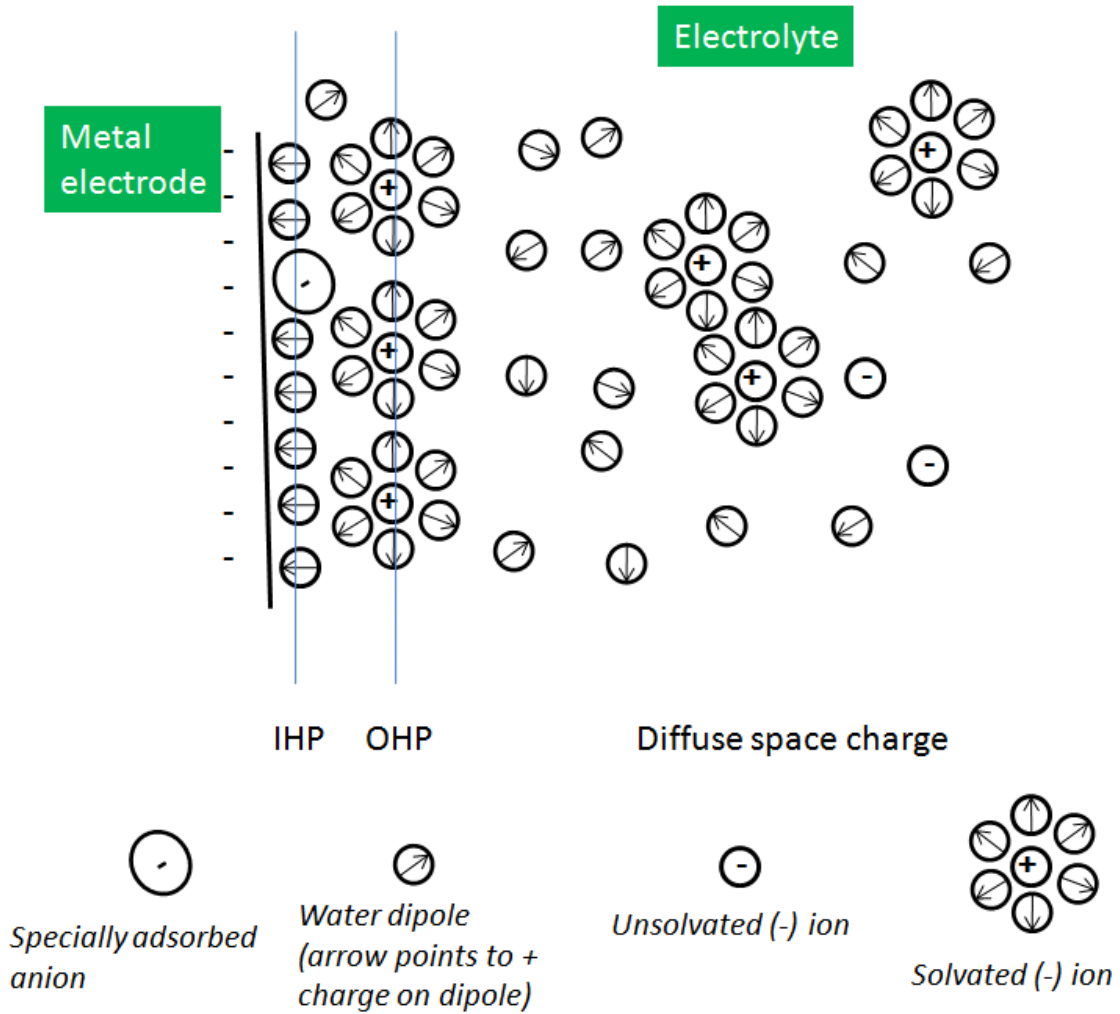


Figure 3-2. A systematic representation of the double layer structure.

As discussed, a space charge region is formed at the electrode/electrolyte interface. As the water dipoles act as a dielectric, the interface should, in theory, behave like a capacitor. However, unlike a simple capacitor, the capacitance of the double layer structure is voltage dependent because ions move in response to an applied potential. The total interfacial capacitance  $C_I$  of the double layer structure is given by

$$\frac{1}{C_I} = \frac{1}{C_H} + \frac{1}{C_G(V)} \quad (1)$$

where  $C_H$  is the Helmholtz capacitance and  $C_G$  is the Gouy-Chapman capacitance [67]. The Gouy-Chapman capacitance  $C_G$  is a voltage dependent term. The idea is that the ions in the diffuse layer are pulled toward the electrode surface when the applied voltage increases. Therefore, the separation of the charge on the electrode and in the electrolyte decreases which leads to an increase in the capacitance.

### 3.2.2 Electrical Model for Electrode/Electrolyte

The electrochemical cell behaves as an impedance. It is therefore possible to represent its behavior by an equivalent circuit. The most commonly used electrode/electrolyte model was developed by Randles in 1973 [85] and is shown in Figure 3-3. All current passes through a resistance called the spreading resistance  $R_s$ . It includes any resistance in the external circuit. For instance, cable resistance, solution resistance and electrode resistance. Then, the parallel elements are introduced because the total current through the interface is the sum of both Faradaic (i.e. current from redox reactions) and non-faradaic processes (i.e. double layer charging). The double layer structure can be modeled by a capacitor  $C_{dl}$ , as discussed in the last section, which has an impedance  $Z_c$ . The Faradaic process is represented by a resistance  $R_t$  (called charge transfer resistance). Another impedance term  $W$ , called the Warburg impedance, is related to the mass transfer resistance. This is due to the fact that solvated ions have to be brought from the bulk to the interface before they can undergo a redox reaction. The impedance  $W$  is defined by

$$W = \frac{1}{(j\omega C_w)^{\frac{1}{2}}} \quad (2)$$

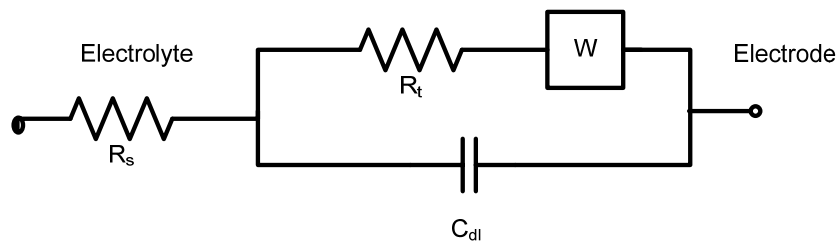


Figure 3-3. Randles' equivalent circuit for the electrode/electrolyte interface.

The total impedance  $Z$  for the Randles model is

$$Z = R_s + \frac{Z_c(R_t + W)}{W + Z_c + R_t} \quad (3)$$

The variation of total impedance  $Z$  with frequency is often of interest. This relationship can be represented in two ways: Bode plots and Nyquist plots. In a Bode plot,  $\log|Z|$  and phase  $\theta$  are plotted against  $\log[\omega]$ . In the Nyquist plot, the imaginary part  $Z''$  of the total impedance  $Z$  is plotted against the real part  $Z'$  of  $Z$  for different values of  $\omega$ . The total impedance  $Z$  can be fitted to the Nyquist plot. In this way, the parameters of the Randles model can be obtained. A typical Nyquist plot of an electrode/electrolyte interface is shown in Figure 3-4.

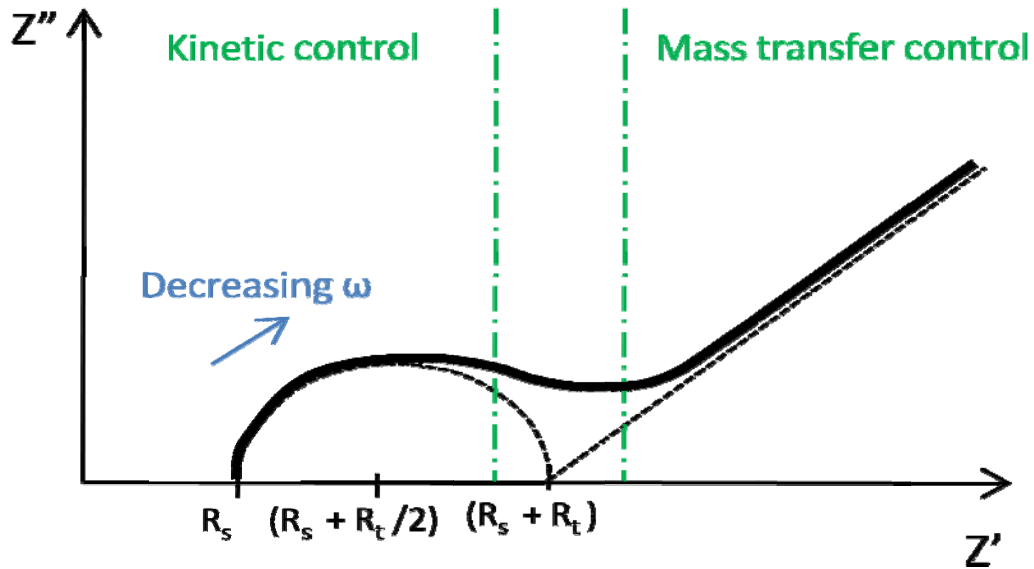


Figure 3-4. A typical Nyquist plot for the Randles model in both high and low frequencies.

The curve can be divided into two regions: low (mass transfer limited) and high frequencies (kinetic limited). At low frequencies, the impedance  $Z_c$  is large enough that it can be approximated as an open circuit. Therefore, the circuit model can be simplified to the form shown in Figure 3-5 for low frequencies.

The low frequency impedance is then:

$$Z = R_s + R_t + \frac{1}{(j\omega C_w)^{\frac{1}{2}}} \quad (4)$$

The real and imaginary parts are

$$Z' = R_s + R_t + (2\omega C_w)^{-\frac{1}{2}} \quad (5)$$

$$Z'' = -(2\omega C_w)^{-\frac{1}{2}} \quad (6)$$

Eliminating  $\omega$ , we get,

$$-Z'' = Z' - (R_s + R_t) \quad (7)$$

This corresponds to a straight line with a slope of 1 (with  $-Z''$  plotted against  $Z'$ ) and an x-intercept of  $R_s + R_t$  in the Nyquist plot.

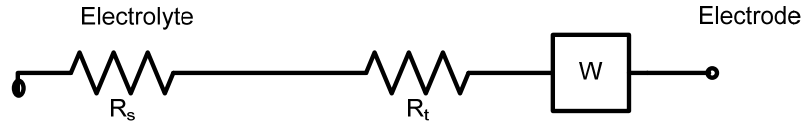


Figure 3-5. Low frequency model of an electrode/electrolyte interface.

At high frequencies, the Warburg impedance is relatively low as compared to  $R_t$  so that it can be considered as a short circuit. The simplified circuit for this case is shown in Figure 3-6.

The high frequency impedance is then:

$$Z = R_s + \frac{R_t}{1 + j\omega R_t C_{dl}} \quad (8)$$

The real and imaginary parts are

$$Z' = R_s + \frac{R_t}{1 + \omega^2 C_{dl}^2 R_t^2} \quad (9)$$

$$Z'' = \frac{\omega C_{dl} R_t^2}{1 + \omega^2 C_{dl}^2 R_t^2} \quad (10)$$

Eliminating  $\omega$ , we get,

$$\left( Z' - \left( R_s + \frac{1}{2} R_t \right) \right)^2 + Z''^2 = \left( \frac{1}{2} R_t \right)^2 \quad (11)$$

This corresponds to a half circle centered at  $Z' = R_s + R_t/2$  with radius  $R_t/2$  in the Nyquist plot.

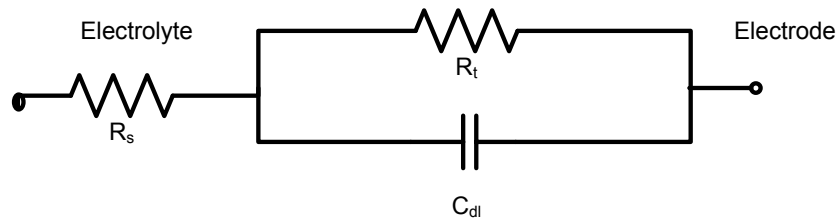


Figure 3-6. High frequency model of an electrode/electrolyte interface.

### 3.3 Techniques in Monitoring Neural Activities

Microprobes are one of the most commonly used devices in studying real-time neural activities. Because information is transmitted and propagates both electrically and chemically between neurons, the microprobes either record extracellular neural activities or electrochemically monitor neurotransmitter synaptic overflow. The microprobes are often brought in close proximity to the cell for extracellular recordings.

The neural signal pathway starts at the stimulated neuron's axon hillock, where an action potential is generated (see Figure 3-7). Then, this electrical action potential is transmitted along the axon until it reaches a junction called the synapse. A schematic representation of a synapse is shown in Figure 3-8. This junction is where neurons

communicate with each other. When the action potential reaches the end of axon, the axon will release certain types of neurotransmitters (e.g. dopamine and/or serotonin). Then, the dendrite of another neuron will collect the released neurotransmitters and fire an action potential. Repeating this process, information can propagate through the neural network. Because of the nature of the information transmission in the brain, the study of neural activities can include both electrical recording, where action potentials are measured and chemical sensing, where neurotransmitters are detected.

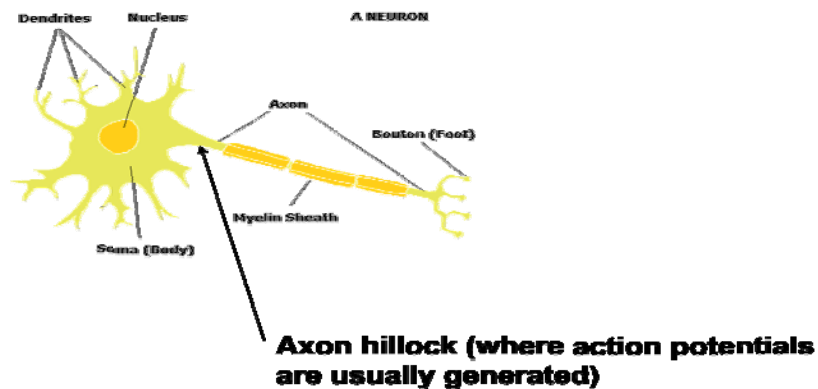


Figure 3-7. A schematic of a neuron.

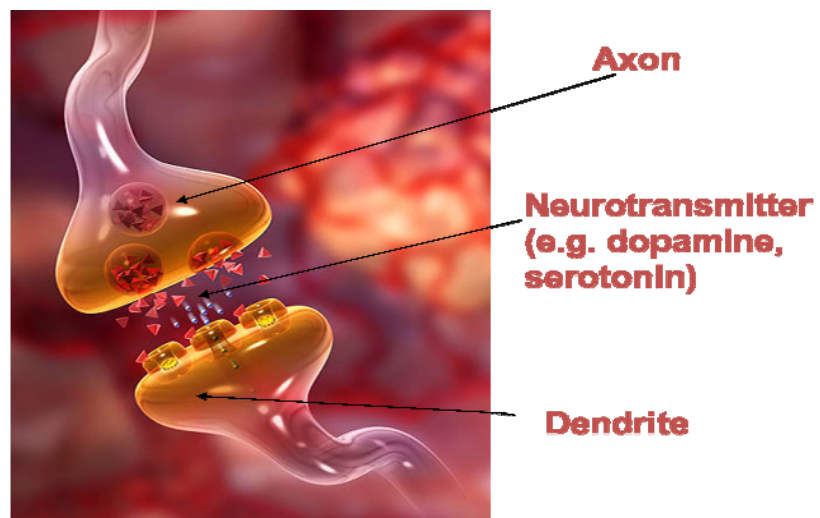


Figure 3-8. A schematic of the synapse.

### 3.3.1 Electrical Recording of Action Potential

The action potential is the electrical signal of interest in the electrical recording. The action potential is a spike of electrical energy that travels along the membrane of a cell, and carries and transmits information along the cell and between different cells. Thus, studying brain activity can be achieved by monitoring and processing the action potentials occurring within cells.

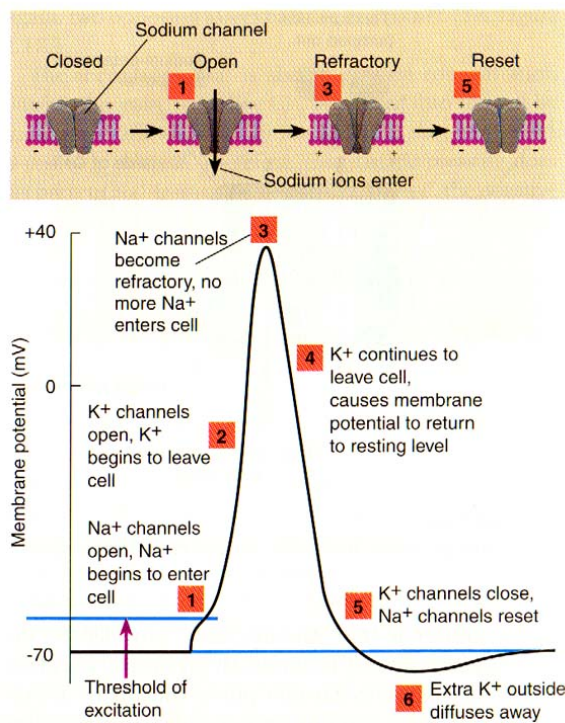


Figure 3-9. A typical example of an action potential [86].

An action potential can be created by many types of cells, but are used most extensively by the nervous system for communication between neurons. They are also used to transmit information from neurons to other body tissues. Action potentials differ based on what type of cell they emanate from. However, a typical action

potential is shown in Figure 3-9. An action potential is caused by an imbalance of ions moving into and out of a cell across its membrane. This membrane is semi-permeable to different ions existing inside and outside of the cell and has many different channels to control the in-flow and out-flow of certain ions. Typically, the common ions found inside and outside of the cell are  $\text{Na}^+$ ,  $\text{K}^+$ ,  $\text{Ca}^{2+}$  and  $\text{Cl}^-$ . An example of the concentrations of these ions is shown in Table 3-1.

The sequences of events that underlie the action potential are shown in Figure 3-9. If there is no excitatory stimulus, the cell is at rest with cell potential  $\sim -70$  mV (measured as the intracellular potential with respect to extracellular potential). This potential is created by the ion concentration difference inside and outside the cell. At this point, the cell is said to be polarized. Upon receiving a stimulus, the cell becomes excited and  $\text{Na}^+$  ion channels on the membrane will be opened to allow  $\text{Na}^+$  ions to enter the cell. At the same time, the voltage-gated  $\text{K}^+$  ion channel opens and  $\text{K}^+$  moves out of the cell due to its concentration gradient. The influx of  $\text{Na}^+$  ion causes the increase in the cell potential to  $\sim +20$  mV. Now, the cell is said to be depolarized. By the time the cell potential reaches  $+50$  mV, the  $\text{Na}^+$  channel will start to close and reduce the inflow of sodium ions. The  $\text{K}^+$  ions continue to diffuse out of the cell and lower the cell potential below the threshold. Then, the voltage-gated channel will close and prevent  $\text{K}^+$  ions from leaving the cell. The cell is now re-polarized. The cell enters a period called the refractory period, at which time it cannot receive any stimulus. The rest potential will then be restored by the active transport of  $\text{K}^+$  into the cell and  $\text{Na}^+$  out of the cell. The actual mechanism is more complex than that discussed here and can be found in most biology textbooks. However, the basic

concept is shown to give a brief understanding of action potentials. After the process outlined here, this action potential propagates along the cell membrane and will be transferred to the other cells.

Microelectrodes/Microprobes, with low input impedances, can be used to capacitively record the action potential, which, as explained earlier, is due to charge movement. The probe must be connected to a high input impedance amplifier and necessary noise filters [87]. Most often, local field potential, which is the sum of action potentials from a number of neurons, is recorded--rather than an individual action potential. As there are numerous electrodes on a given probe, a reliable data acquisition system is desired which can be found in the market [88]. Researchers, on the other hand, have also developed implantable microsystems used to record signals received on a probe. These systems can also transmit data wirelessly and provide more flexibility in neural studies [89].

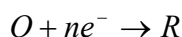
Table 3-1. Concentrations of ions for mammalian skeletal muscle [85].

| <b>Ion</b>             | <b>Extracellular concentration (mM)</b> | <b>Intracellular concentration (mM)</b> |
|------------------------|---|---|
| <b>Na<sup>+</sup></b>  | 145                                     | 12                                      |
| <b>K<sup>+</sup></b>   | 4                                       | 155                                     |
| <b>Ca<sup>2+</sup></b> | 1.5                                     | 10 <sup>-7</sup> M                      |
| <b>Cl<sup>-</sup></b>  | 123                                     | 4.2                                     |

### 3.3.2 Neurochemical Detection of Neurotransmitters

Neurochemical detection is a method used to measure Faradic currents resulting from the oxidation or reduction of neurochemical species released from neurons. These neurotransmitters are highly localized inside the synapse and their concentrations decrease with increasing distance from the synapse. Therefore, the microprobe has to be placed as closely as possible to the synapse. (<50 $\mu\text{m}$ ) [90]. The current is caused by electron transfer to and from an electrode across the electrode/electrolyte interface. This measurement can be performed using electrochemical techniques such as cyclic voltammetry and amperometry. These techniques require three electrodes: a working electrode (WE), reference electrode (RE) and counter (CE) electrode. The oxidation or reduction reaction of the redox couple is forced to occur at the WE by applying sufficient voltage between itself and the CE. The RE is used as the reference for measuring the potential of the WE and does not take any current from the cell. It should have low impedance and be capable of maintaining a constant potential throughout the measurement process. The most commonly used RE is Ag/AgCl. It is stable and able to maintain a constant potential independent of which electrolyte is under examination.. By controlling the potential of the WE (as referenced to the RE) and simultaneously measuring the amount of current passing through it, information concerning the charge transfer processes that occur at the electrode-electrolyte interface is obtained.

Considering the following redox system,



where O and R are the oxidized and reduced forms of the redox couple, respectively.

This reaction will occur in a potential region where the electron transfer is thermodynamically or kinetically favorable. For systems controlled by the laws of thermodynamics, the potential of the electroactive species at the surface  $C_o(0,t)$  and  $C_R(0,t)$  vary according to the Nernst equation

$$E = E^\circ + \frac{2.3RT}{nF} \log \frac{C_o(0,t)}{C_R(0,t)} \quad (12)$$

where  $E^\circ$  is the standard potential for the redox reaction,  $R$  is the universal gas constant ( $8.314 \text{ J K}^{-1} \text{ mol}^{-1}$ ),  $T$  is the temperature in Kelvin,  $n$  is the number of electrons transferred in the reaction, and  $F$  is the Faraday constant ( $96487 \text{ coulombs}$ ). If the potential  $E$  is smaller than  $E^\circ$ , the oxidized form tends to be reduced. But if the potential  $E$  is larger than  $E^\circ$ , the reduced form tends to be oxidized. Therefore, current flows due to the electron transfer between the electrode and redox couple. Every redox couple has its own standard potential which can be found in electrochemistry textbooks.

Cyclic voltammetry is the most widely used technique for acquiring qualitative and quantitative information about electrochemical reactions. A triangular potential waveform as shown in Figure 3-10 is applied to the working electrode. The amplitude of the final and initial potentials and the scan rate can be adjusted depending on the particular application. The voltage-current plot, called a cyclic voltammogram, is shown Figure 3-11. For the forward scan, there is no significant current measured until the potential reaches  $E^\circ$ . As the applied voltage reaches  $E^\circ$ , the oxidized form of the redox couple starts to be reduced and thus, current flow from the WE to the CE increases as the voltage increases. The peak current represents the voltage where the rate of oxidation equals the rate of redox couple reaching the surface. For the reverse scan, it is simply the reverse of the process--the reduced form of the redox couple is oxidized to its oxidized

form. As mentioned earlier, different redox couples have different standard potentials,  $E^\circ$ . Since these standard potentials can be obtained from a cyclic voltammogram, cyclic voltammetry is a powerful tool in indentifying redox couples. For example, it can be used in detecting neurotransmitters *in vivo*, which are indicative of neural activity.

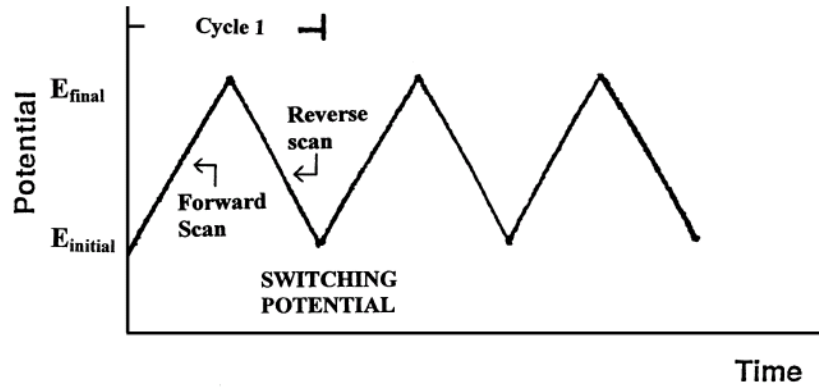


Figure 3-10. A triangular potential waveform used in cyclic voltammetry [68].

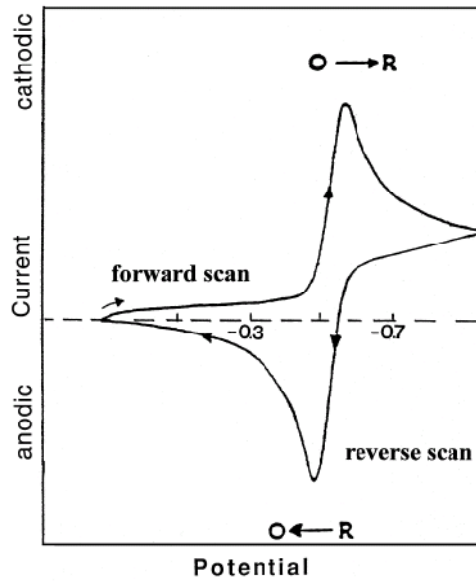


Figure 3-11. A typical cyclic voltammogram [68].

### 3.4 **Summary**

This chapter reviews the basic electrode/electrolyte model which aids in the understanding of reactions taking place on an electrode surface. It is found that a double layer is formed at the electrode/electrolyte interface. The interface can be modeled by an equivalent circuit, which is a combination of resistors and capacitors. In addition, two techniques used for monitoring neural activities are discussed. These include the monitoring of action potentials and the detection of the release of neurotransmitters.

# Chapter 4

## Poly-C Micromachining Technologies

### Relevant to Probe Fabrication

#### 4.1 Introduction

CVD poly-C is becoming a more and more attractive material for MEMS applications due to its unique properties. MEMS applications, for example, sensors [91], packaging [92] and electronics [93], have already been fabricated using diamond. However, the difficulty in growing  $sp^3$  bonded carbon, which usually requires high temperature as a growth condition, is currently causing a delay in the development of a reliable and economical diamond micro-fabrication technology that is compatible with conventional microsystems/MEMS technologies. An alternative to diamond is diamond-like carbon (DLC) which can be deposited at room temperature. Unfortunately, the quality of the film (i.e. its mechanical strength) is not as strong as that of diamond as there is no long-range order of the position of atoms.

In this study, CVD poly-C is used as the core material for probe fabrication. In order to integrate CVD poly-C into Si MEMS, several important issues must first be addressed. These issues include seeding, growth and etching of CVD diamond. In this chapter, physical, chemical and biomedical properties of CVD poly-C films and its

associated micromachining technologies are presented. Combined, these properties and technologies have made the development of a diamond neural probe possible.

## **4.2 Properties of Polycrystalline Diamond**

### **4.2.1 Physical and Chemical Properties of Diamond**

Some of the mechanical and electrical properties of poly-C diamond are listed in Table 4-1. It is well known that diamond is the hardest and strongest material found in nature. Its mechanical strength comes as a result of the diamond lattice; each carbon atom is covalently bonded with its four neighboring atoms by hybridized  $sp^3$  atomic orbitals. Thus, it is a good candidate for high temperature (due to its large band gap), high speed (owing to its high carrier mobility) and high power (because of its high thermal conductivity) applications. Compared with silicon, diamond has a much higher Young's modulus which indicates its higher strength. In addition to Young's modulus, fracture toughness is also a good indicator of structural integrity. Fracture toughness is a property which describes the ability of a material containing a crack to resist fracture.. Diamond exhibits a high fracture toughness as shown in Table 4-1. If a material has a large value of fracture toughness, it will likely undergo ductile fracture. Typical values for fracture toughness are  $\sim 150 \text{ MPa m}^{1/2}$  for ductile metals,  $25 \text{ MPa m}^{1/2}$  for brittle ones and  $1-10 \text{ MPa m}^{1/2}$  for glasses and brittle polymers. Thus, compared to silicon, diamond is more resistant to fracture.

Diamond also exhibits good chemical properties. It is found that diamond films are stable during anodic polarization in acidic fluoride, alkaline, acidic chloride and neutral

chloride media [70][112]. Also, diamond is resistant to fouling compared to graphite as mentioned in the previous section. For all of these reasons, diamond film is an excellent material for use in harsh environments.

Table 4-1. Properties of silicon and diamond [82].

| <b>Properties</b>                                    | <b>Silicon</b>    | <b>Poly-C Diamond</b> |
|--|-------------------|-----------------------|
| Density (g/cm <sup>3</sup> )                         | 2.329             | 3.52                  |
| Melting point (K)                                    | 1412              | --                    |
| Young's Modulus (GPa)                                | 130-180           | 800-1180              |
| Fracture toughness (MPa m <sup>1/2</sup> )           | 1-2.5 [94][95]    | 3-6 [96][97]          |
| Poisson's ratio                                      | 0.22-0.24         | 0.07-0.148            |
| Band gap (eV)  | 1.12              | 5.45                  |
| Carrier Mobility                                     |                   |                       |
| Electron (cm <sup>2</sup> /Vs)                       | 1450              | 23                    |
| Hole (cm <sup>2</sup> /Vs)                           | 500               | 10-1000               |
| Dielectric constant                                  | 11.7              | 6.5                   |
| Breakdown voltage (MV/cm)                            | 0.37-0.5          | 0.1-1                 |
| Intrinsic resistivity (Ωcm)                          | 1x10 <sup>3</sup> | 1x10 <sup>16</sup>    |
| Thermal conductivity (W/cmK)                         | 1.5               | 4-20                  |
| Thermal expansion coefficient (10 <sup>-6</sup> /°C) | 2.6               | 2.6                   |

## 4.2.2 Biocompatibility of Diamond

Diamond has been called the “biomaterial of the 21<sup>st</sup> Century” due to its excellent biocompatibility [98]. With recent advances in industrial synthesis of diamond and diamond-like carbon film bringing prices down significantly, researchers are increasingly willing to experiment with diamond coatings for medical implants, for example. Examples of diamond use in implants includes artificial heart valves [99], prosthetic devices [100] and joint replacements [101]. Diamond is advantageous in these situations because of its excellent wear resistance and high resistance to blood platelet adhesion. Diamond has also been used as the material for biosensors [77][102][103]. Diamond-like carbon (DLC) coated orthopedic pins implanted in sheep also demonstrate low diamond bioactivity [104]. Even more, CVD diamond coatings for artificial joints are said to have “low immunoreactivity”[105].

The first study of protein adsorption on CVD diamond was performed in 1995, and focused on the absorption of fibrinogen [106]. Fibrinogen is the major protein involved in the initiation of coagulation and inflammation including fibrosis around implanted biomaterials. It has been found that the CVD diamond absorbed and denatured relatively small amounts of fibrinogen. Also, *in vitro* and *in vivo* experiments showed less cell adhesion to the diamond surface and activation on the surface of CVD diamond when compared to both titanium and 316 stainless steel. In addition, CVD diamond has also shown that it has no cytotoxic effect, no hemolytic effect or any complementary

activation [98][107]. More detailed studies on diamond biocompatibility can be found in [108][109][110][111].

Although diamond is reported to be a biocompatible material, it is important to point out that biocompatibility is highly application-specific. Some applications require a non-adhesive interface, while other applications will require complete tissue integration with the implanted devices.

### **4.2.3 Electrochemical Properties of Diamond**

Boron-doped diamond is found to have a very wide potential window (the anodic evolution potential is especially high) as compared to other materials which is advantageous in electroanalysis of substances which have a similar or higher oxidation potential than oxygen. A high potential for oxygen evolution permits electrogeneration of oxidants such as hydroxyl radicals from water.. The potential window of the diamond depends heavily on its growth conditions. The relationship between potential window and the C/H ratio during diamond growth is shown in Figure 4-1 [112][113]. The potential window decreases and the background current magnitude increases with increasing C/H ratio.

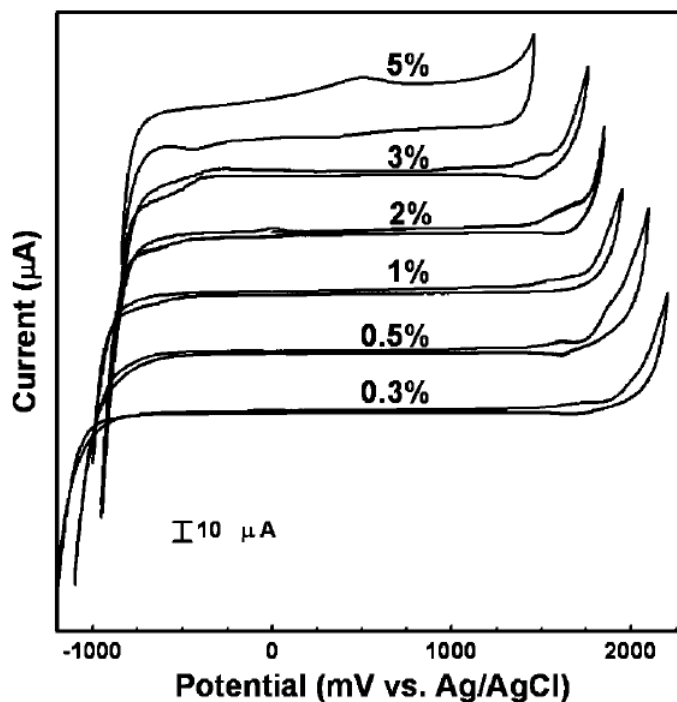


Figure 4-1. Cyclic voltammeteries of diamond films with different C/H source gas mixtures in 0.1M HClO<sub>4</sub>.

In addition, when immersed in an electrolyte, diamond also displays low background current, low double layer capacitance, chemical and mechanical stability and resistance to fouling. It also shows the lack of a surface oxide, and a controllable surface termination [98][114]. These characteristics have led to the application of diamond in electrochemical sensors, for electroanalysis, for electrochemical synthesis, and for anodic destruction of organic wastes. Other properties such as low  $iR$  drop and high sensitivity are discussed in detail in [115].

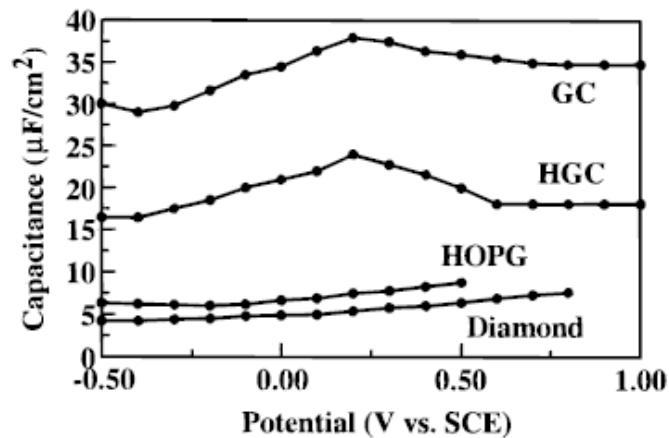


Figure 4-2. Capacitance-potential profiles of GC, HGC, HOPG and diamond in 0.1M HClO<sub>4</sub>.

Table 4-2. Comparison of double layer capacitance and redox peak separation in 0.1M KCl.

| Electrode                  | Double layer capacitance (μF/cm <sup>2</sup> ) | ΔE <sub>p</sub> (mV) |
|----------------------------|--|----------------------|
| Glassy carbon              | 35   | 115                  |
| Hydrogenated glassy carbon | 20   | 107                  |
| HOPG                       | 6  | 165                  |
| Diamond                    | 5  | 152                  |

## 4.3 Poly-C Technologies

### 4.3.1 Diamond Nucleation

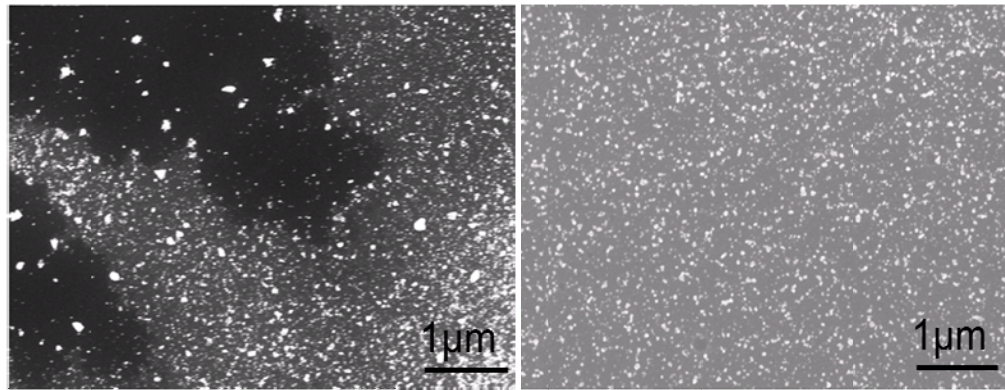
The CVD growth of poly-C on non-diamond substrates such as Si requires a pretreatment step to generate seeds (or nuclei) on the substrate. One of the following are typically used for the pretreatment: surface abrasion [116][117][118] followed by the sonication of diamond powder loaded solution [119], bias enhanced nucleation (BEN) [120][121][122], spinning of diamond-powder-loaded photoresist (DPR) [123], spraying of diamond-loaded fluids [124][125] or diamond-loaded water (DW) [126]. Table 4-3 summarizes these pretreatments and their effects on seeding.

The DW pretreatment has been used in previous studies covering the integration of poly-C piezoresistors into Si cochlear probes [126]. During the probe fabrication process, poly-C diamond piezoresistors are fabricated on top of SiO<sub>2</sub>. This surface is hydrophilic. In contrast to growth on SiO<sub>2</sub>, in the development of poly-C probes, poly-C films are sometimes grown on directly on an Si substrate--which is a hydrophobic surface. A surface treatment is required for more uniform seeding on the Si substrate. In this study, RCA-clean has been used to treat the Si surface. This cleaning process increases the contact angle between a water droplet and the Si surface. In fact, this process gives the smallest contact angle 5° (i.e. more hydrophilic surface) among all other surface treatments listed in [127]. Therefore, RCA-clean was performed on the Si sample before nucleation throughout this study.

Table 4-3. Comparison of different seeding methods on seeding density, substrate material and surface morphology [126].

| <b>Seeding Method</b>                   | Sonication /Abrasion                    | BEN                                 | DPR                                 | Spray/paint             | DW  |
|---|---|-------------------------------------|-------------------------------------|-------------------------|---|
| <b>Seeding Density</b>                  | Up to $10^{10}$                         | Up to $10^{11}$                     | $\sim 10^8$                         | Up to $10^{11}$         | $10^8 \sim 10^{11}$   |
| <b>Substrate Selectivity</b>            | Most dielectric & metal                 | Conductive Si or Metal,             | Most dielectric & metal             | Most dielectric & metal | Hydrophilic surface like ( $\text{SiO}_2$ & $\text{Si}_3\text{N}_4$ ) |
| <b>Surface Affection</b>                | scratch surface, not good for thin film | No damage                           | No damage                           | No damage               | No damage   |
| <b>Uniformity &amp; Controllability</b> | Not uniform                             | Uniform & repeatable on whole wafer | Uniform & repeatable on whole wafer | Not uniform             | Uniform & repeatable on whole wafer                                   |

A comparison of nucleation on a non-treated and RCA-treated Si surface is shown in Figure 4-3. The DW is supplied by Advanced Abrasives Corporation and was diluted to contain 0.5% diamond powder in water. The average seed size was 1 $\mu\text{m}$ . Then, the DW was applied to the substrate with a 500 rpm pre-spin for 10 sec followed by a 2000 rpm phase for 30 sec. As shown in the Figure 4-3, the RCA-treated surface shows a better and more uniform seeding density as compared to the non-treated surface. This is due to the fact that the Si surface becomes hydrophilic after RCA cleaning. The resulting seeding density is in the range of  $10^9 - 10^{10}$  seeds/cm<sup>2</sup>.



(a)

(b)

Figure 4-3. Seed distribution on (a) a non-treated and (b) an RCA-treated Si surface.

### 4.3.2 Diamond Growth and Doping

Microwave Plasma Chemical Vapor Deposition (MPCVD) was used for poly-C growth in this project. A schematic of the MPCVD system is shown in Figure 4-4. This MPCVD (Wavemat™ MPDR 313EHP) system has a chamber (D = 9") and quartz bell jar (D = 5"). A 2.45 GHz, 5 kW microwave power supply (Sairem™, GMP60KSM) and the large chamber size mentioned above ensured the uniformity of the plasma in the vicinity of wafers up to 2"x 2". To ensure this, a sample wafer was heated by the plasma and its temperature was monitored by a pyrometer outside the chamber. Typical deposition conditions used in this study are listed in Table 4-4.

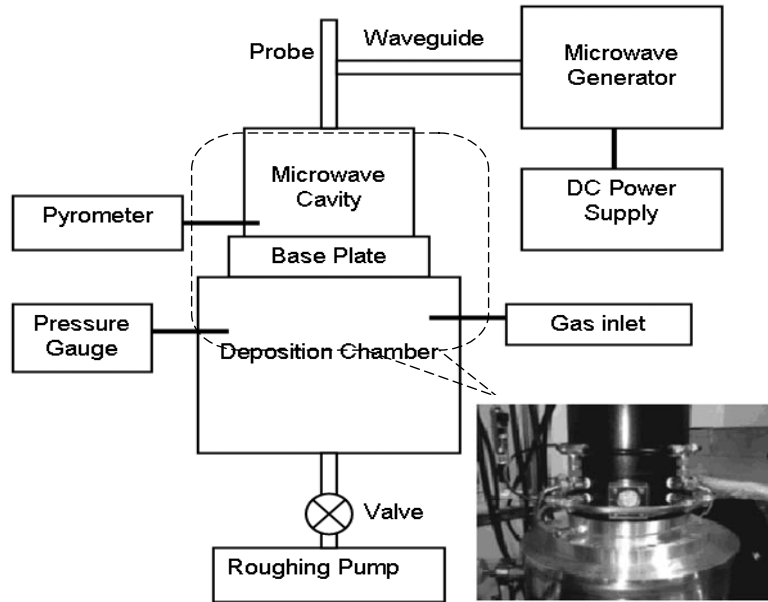


Figure 4-4. Schematic of the MPCVD system used in this project.

Table 4-4 Conditions for diamond growth using MPCVD

| Parameter(s)                         | Value(s)   |
|--------------------------------------|--|
| Growth Temperature                   | 750 °C   |
| Growth Pressure                      | 40 Torr  |
| Gases Used for Growth                | Methane: 1 sccm<br>Hydrogen: 100 sccm  |
| Dopant Used for B-doped Poly-C       | Trimethylboron diluted in H <sub>2</sub><br>(0.1% of B(CH <sub>3</sub> ) <sub>3</sub> by volume in H <sub>2</sub> ): 5-10 sccm |
| Microwave Power Used for Growth      | 2.3 kW, 2.4 GHz  |
| Growth Rate                          | 0.10 - 0.15 μm/h   |
| Poly-C Film Thickness; Undoped/Doped | 3 μm/ 0.5 μm   |

Diamond film was in-situ boron-doped by introducing trimethylboron (TMB),  $(B(CH_3)_3)$ , gas diluted in hydrogen. The boron doping level, according to the data presented in [126], is in the range of 3000 - 7000 ppm (B/C ratio in gas phase) and resistivities are in the range of  $10^{-1}$  -  $10^{-3}$   $\Omega\text{cm}$ . The average grain size on the surface of poly-C film is approximately 2  $\mu\text{m}$  for a growth time of 20 h. The film quality, as indicated by the  $sp^3/sp^2$  C-C bond ratio, is very good as indicated by a sharp Raman peak at  $1332\text{ cm}^{-1}$  as shown in Figure 4-5.

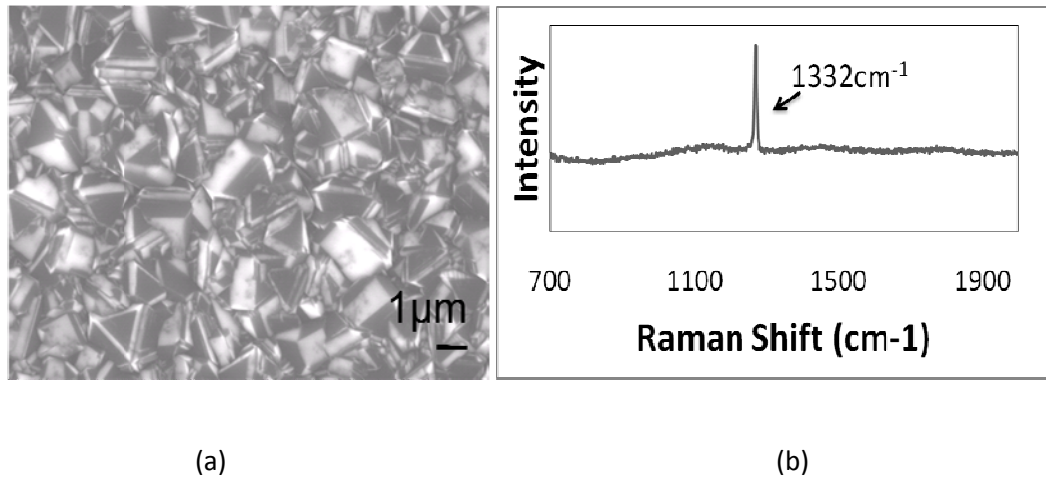


Figure 4-5. (a) An SEM image of a poly-C surface and (b) its Raman spectrum.

### 4.3.3 Inadvertent SiO<sub>2</sub> Etching

As shown in Table 4-4, the growth temperature is high enough that it can melt most of the metals which have low melting temperature (e.g. Al). In addition, the high power of the hydrogen plasma is another factor that limits the use of metals in the MPCVD system. Metals (e.g. Au and Cu) can be etched or deformed mechanically

during the growth of diamond. Therefore, the harsh environment in the MPCVD chamber during diamond growth limits the integration of poly-C into conventional Si or semiconductor micromachining technology. Also, it is found in this work that SiO<sub>2</sub>, which is commonly used in semiconductor fabrication, can be etched significantly during diamond growth. The hydrogen plasma continues to etch SiO<sub>2</sub> through the holes between the diamond seeds until the SiO<sub>2</sub> is fully covered by poly-C. This can cause problems if the SiO<sub>2</sub> layer is used as an insulating layer. Since the etching of SiO<sub>2</sub> happens only when there are pin-holes in the poly-C film, increasing seeding density can help in minimizing the effect of this etching issue. Increased seeding density can be achieved by either lowering the spin rate for nucleation or by increasing the concentration of DW. However, with this method, pin-holes still exist before a continuous diamond film is formed, and the SiO<sub>2</sub> can still be etched. Thus, it is important to characterize the etch rate of SiO<sub>2</sub> in the MPCVD chamber so that the amount of SiO<sub>2</sub> etched becomes a known factor and can be taken into consideration in any process design. The etch rate of different types of commonly used SiO<sub>2</sub> layers during diamond growth at 750°C are listed in Table 4-5.

Besides the etch rate of SiO<sub>2</sub>, the time  $t_c$  for obtaining a pin-hole free poly-C film should be known in order to calculate the total thickness of oxide etched. This time  $t_c$  is plotted as a function of spin speed during the DW seeding as shown in Figure 4-6. The resulting density is also plotted. It is noted that as the spin speed increases, the seeding density decreases leading to a longer time necessary for obtaining a pinhole free poly-C film. The total thickness of SiO<sub>2</sub>  $t$  is then calculated by the following equation,

$$t = t_c \times \text{etch rate.}$$

Table 4-5. Etch rates of different types of silicon dioxide (no annealing was done after growth)

| Types of silicon oxide /growth temperature | Growth temperature (°C) | Etch rate (nm/min) at 750°C |
|--|-------------------------|-----------------------------|
| Thermal / 1000°C                           | 1100                    | 1.0-3.0                     |
| LPCVD / 450°C                              | 450                     | 1.4-3.1                     |
| PECVD / 380°C                              | 380                     | 2.8-4.4                     |

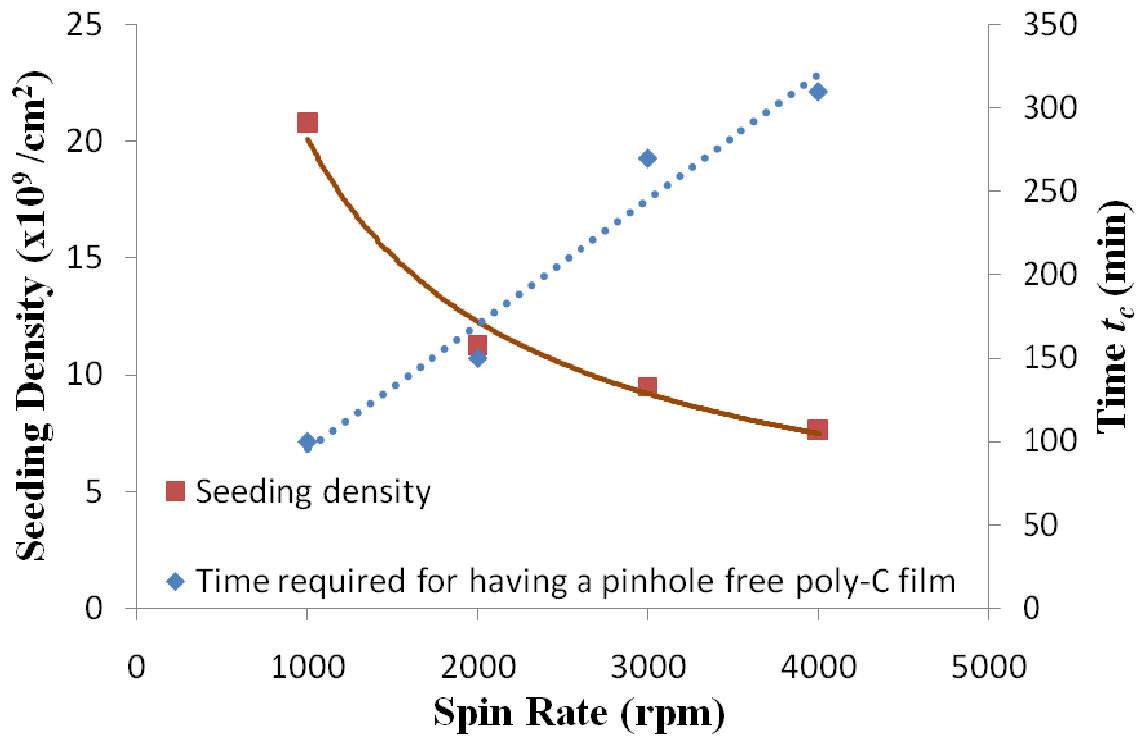


Figure 4-6. The relationships between the seeding density and time  $t_c$  as a function of seeding spin rate.

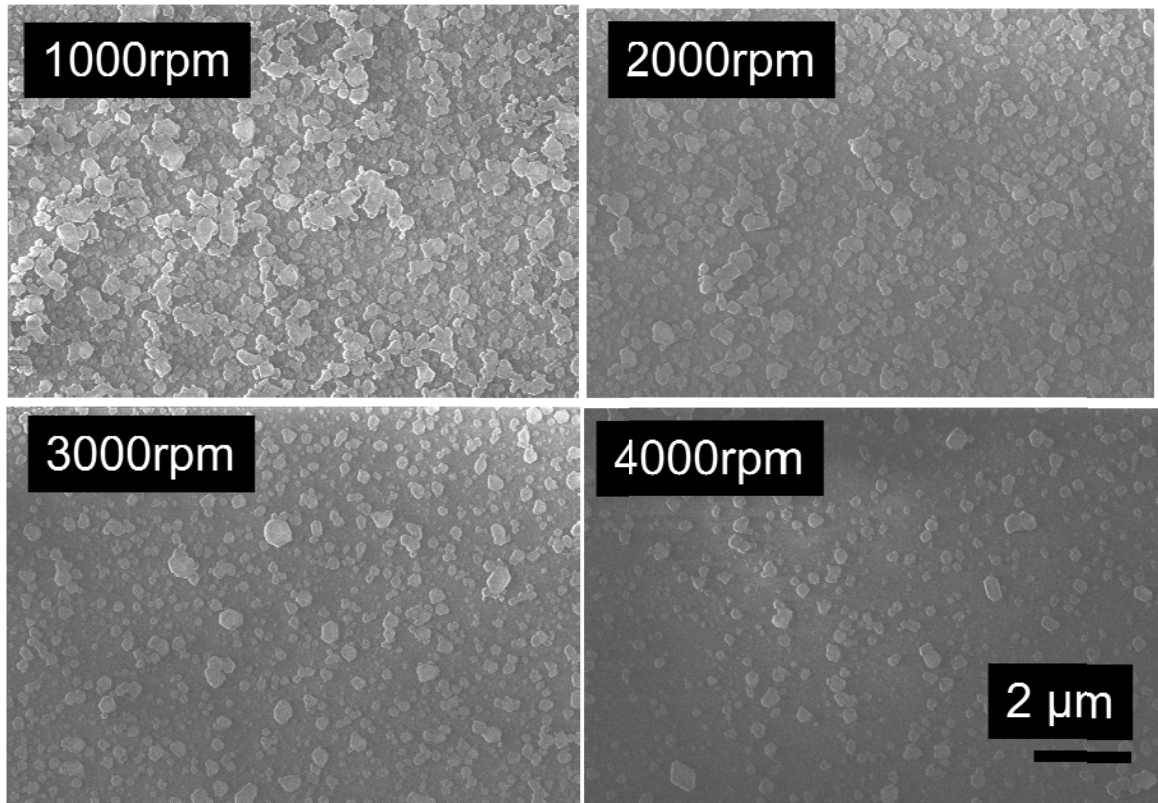


Figure 4-7. Diamond seeding density on RCA treated Si surface with different spin rates (the samples have been undergone 40 mins diamond growth).

#### 4.3.4 Conductivity in Undoped Poly-C Films

Ideally, undoped diamond is a large band gap material with a value of 5.5 eV. It should not be conducting in any case. However, it is also a fact that polycrystalline diamond can show conductivities (low resistivities) due to many factors. For example, growth conditions, grain boundaries, impurities and etc. In this project, undoped poly-C diamond is used as the probe substrate and the conducting interconnects are fabricated on top of the poly-C. In this study, as-grown diamond exhibited finite conductive, which,

given its purpose in the probe, is undesirable. Therefore, it is important to find the cause of the conductivity of the as-grown undoped poly-C.

There are several possible causes for the undesired conductivity. First, impurities in the chamber may incorporate into the diamond film during its growth. Obviously, hydrogen is one of the main sources which contributes to the conductivity of diamond. The surface of an as-grown poly-C film is hydrogen-terminated. Because of the hydrogen termination, the surface becomes conductive after exposure to the atmosphere. This conductive surface layer can be removed by annealing in oxygen at 600°C or by oxygen plasma etching [128][129]. In addition to its role in increasing surface conductivity, hydrogen may incorporate deep into the poly-C film and cause bulk conduction. The hydrogen trapped in the poly-C film can be released by annealing under nitrogen at 800°C for an hour [130]. Also, the intrinsic defects in poly-C films can be a factor which contributes to the conductivity of undoped diamond, for example, the  $sp^2$  C-C bond. These defects appear mostly on the grain boundaries [131][132] and unfortunately, cannot be avoided in poly-C film as grain boundaries must always exist.

In this project, it is found that there are other factors affecting the conductivity of undoped diamond. They are in the form of impurities (i.e. boron) which originate from Si substrates and the MPCVD chamber and can be incorporated into the diamond film during growth. The effect of boron impurities from Si substrates can be verified by the following experiment. Two samples (*a* & *b*) were placed next to each other in the MPCVD chamber as shown in Figure 4-8. Sample *a* is the control sample, which has a layer of SiO<sub>2</sub> (2µm) on top of Si in each experiment. The layer on top of sample *b* is varied in different experiments as listed in Table 4-6. The resistivity (after removing the

conductive surface layer) of sample *a* was monitored for each experiment. It is found that the resistivity of sample *a* is related to the previous treatment on sample *b*. If sample *b* is highly boron doped and not covered with SiO<sub>2</sub>, the resistivity of sample *a* is lower. But, sample *a*'s resistivity seems unaffected b sample *b* is n-type Si and even without SiO<sub>2</sub> layer on top. It is likely that the boron in sample *b* got diffused out and incorporate into sample *a*. Also, the SiO<sub>2</sub> can help in blocking the boron out diffusion.

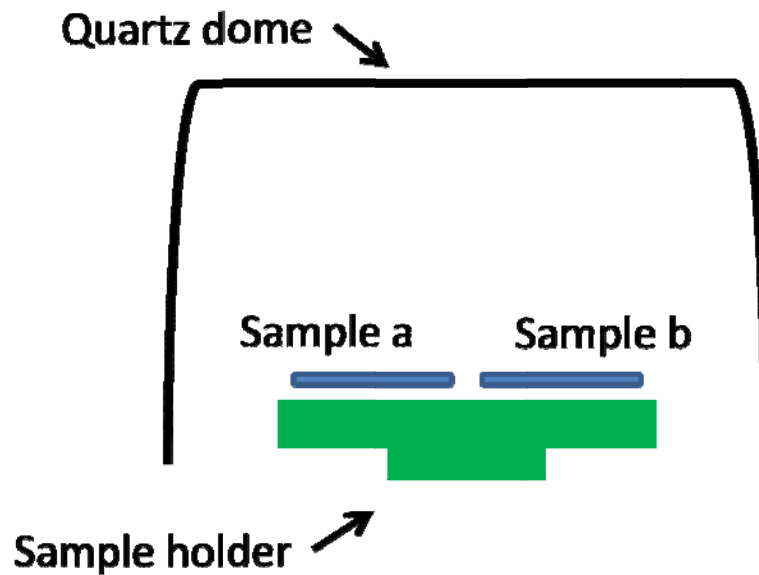


Figure 4-8. Schematics of an experimental setup for showing boron-out diffusion from Si substrate in the MPCVD chamber.

Table 4-6. Effect of boron out-diffusion from the neighborhood wafer on the diamond resistivity.

| Resistivity of sample a (plasma etched for 10mins and annealed at 750°C for 10mins) | Types of wafers put in the same growth (sample b) |
|---|---|
| $\sim 10^5$   | SiO <sub>2</sub> /p <sup>+</sup> Si               |
| $\sim 10^4$   | SiO <sub>2</sub> /p <sup>++</sup> Si              |
| $\sim 10^3$   | p <sup>+</sup> Si                                 |
| $\sim 10^3$   | p <sup>++</sup> Si                                |
| $\sim 10^5$   | n <sup>-</sup> Si                                 |

Another factor is the impurities coming from the chamber. In this experiment, sample *a* and *b* were put in the MPCVD chamber for diamond growth separately. Poly-C film was grown on sample *a* first. It is followed by undoped diamond on sample *b* immediately. It is observed that if doped diamond is grown on sample *a*, the resistivity of sample *b* (undoped diamond) will be lower. This is due to the fact that boron atoms are either stick on the dome or the sample holder and ruin the next sample. Therefore, it is not recommended to have a single system doing both doped and undoped diamond growth. Or, the chamber has to be cleaned using hydrogen or more effectively oxygen plasma before each run.

Table 4-7. Effect of process history of the MPCVD chamber on the resistivity of undoped diamond.

| Sample <i>a</i> 's history     | Sample <i>b</i> 's resistivity |
|--------------------------------|--------------------------------|
| Undoped diamond 20hrs          | $\sim 10^5$                    |
| Doped diamond 10hrs (1.5% TMB) | $\sim 10^1$                    |
| Doped diamond 10hrs (10% TMB)  | $\sim 10^1$                    |

#### 4.4 Diamond Etching

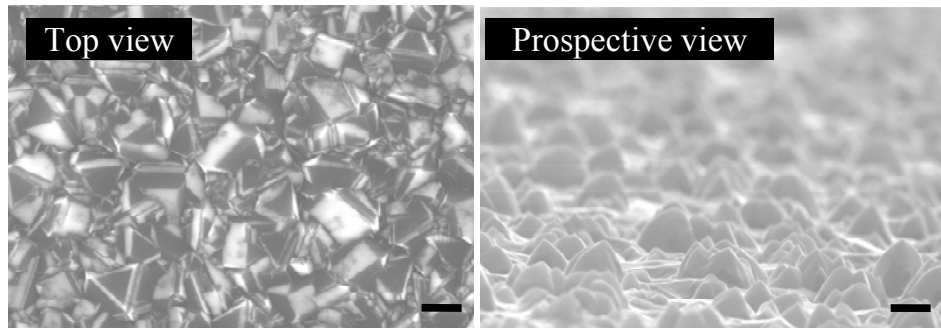
Although the reactive ion etching of diamond has been studied intensively [133][134][135], poly-C dry etching used in the neural probe fabrication in the current work has led to some problems. The recipe used for the diamond etch is shown in Table 4-8. The problem comes as a result of the  $CF_4$  in the etching gases--Si or  $SiO_2$  will be etched in any etching gases which contain fluorine. In the poly-C probe fabrication, poly-C film is either grown on top of the Si or  $SiO_2$  surface. Due to these facts, Si or  $SiO_2$  will be inadvertently etched during poly-C etching.

An example is shown in Figure 4-9. This figure is a group of SEM micrographs taken at different stages of poly-C dry etching. As the etching of poly-C continues to reach the seeding depth of the poly-C film, holes appear in the poly-C film as seen in Figure 4-9 (c). At this stage of the etching process, if the etching gases contain fluorine, etching of the underlying substrate (Si or  $SiO_2$ ) takes place leaving the substrate surface very rough. Also, it is well known that micro columns (due to micromasking) would be formed in the absence of fluorine in the etching gases [136], which is due to the sputtering of Al by  $O_2$  plasma. The showering of sputtered Al particles on the surface being etched leads to micromasking.

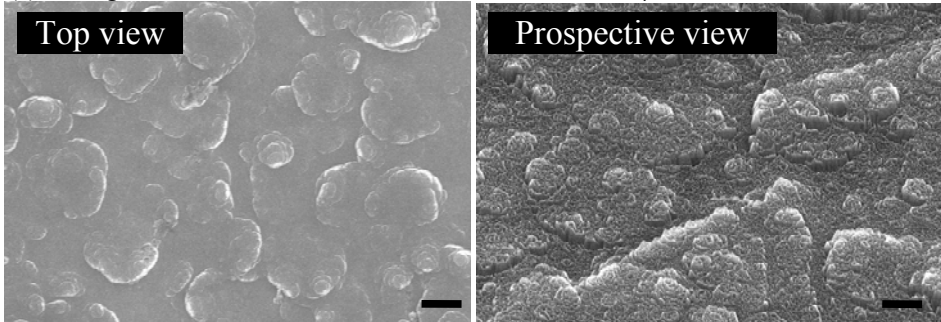
A two step etching process was developed to eliminate the problems of micromasking and the substrate etching [137]. First, poly-C is etched in the presence of only CF<sub>4</sub> until a very thin poly-C film is left on the surface. Then, the final etching stage is performed in pure oxygen. This process leads to a smooth Si or SiO<sub>2</sub> surface.

Table 4-8 Parameters for diamond etch

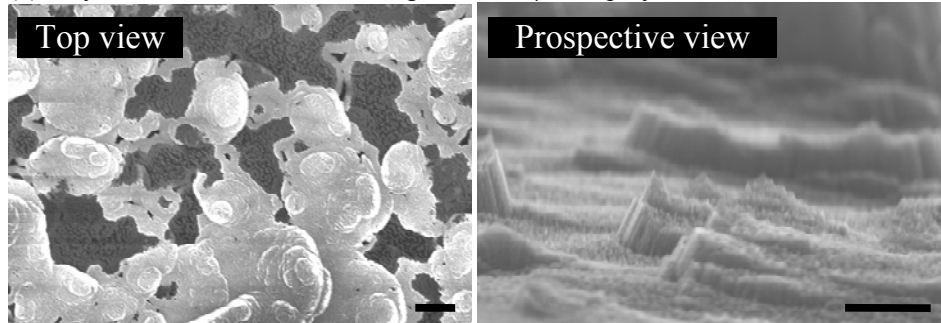
| <b>Parameter(s)</b> | <b>Value(s)</b>   |
|---------------------|---|
| Power               | 300 W   |
| Pressure            | 50 Torr   |
| Gases               | O <sub>2</sub> : 40 sccm<br>Tetrafluoromethane (CF <sub>4</sub> ): 1 sccm |
| Bias                | 293V  |
| Etch rate           | 1.2 μm/h  |



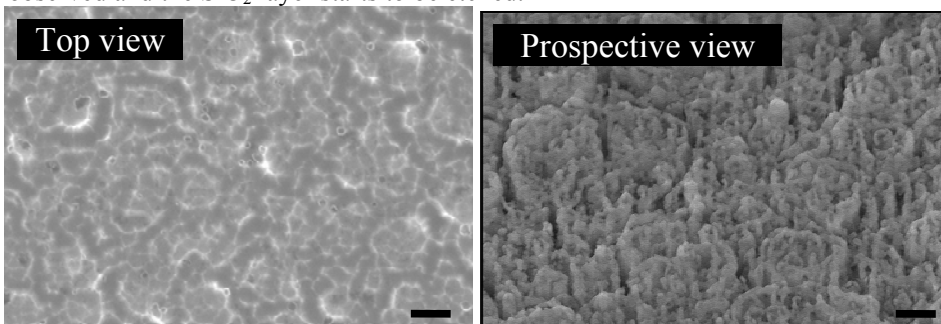
(a) As-grown diamond surface for a film thickness of 3  $\mu\text{m}$ .



(b) Poly-C surface after 1h of etching when 1.2  $\mu\text{m}$  of poly-C has been etched.



(c) Poly-C surface after 2h of etching when 0.6  $\mu\text{m}$  of poly-C remains; pinholes can be observed and the  $\text{SiO}_2$  layer starts to be etched.



(d) Poly-C surface after 3h of etching when the poly-C is fully etched and a rough  $\text{SiO}_2$  surface is left due to the presence of fluoride in the etching gases.

Figure 4-9. SEM images of the diamond surface at different stages of the etching process. The bar shown on the lower right corner of each image is 2  $\mu\text{m}$ .

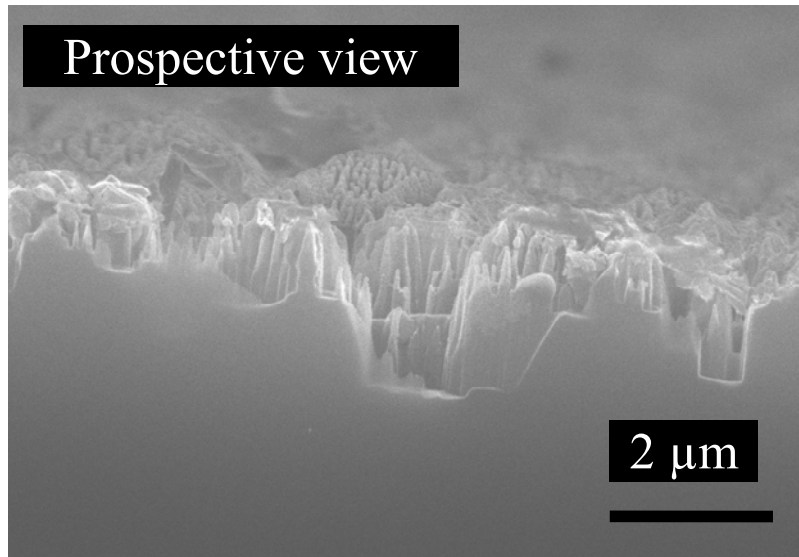


Figure 4-10. A rough Si surface which has been over etched caused by  $\text{CF}_4$  in the diamond etching recipe.

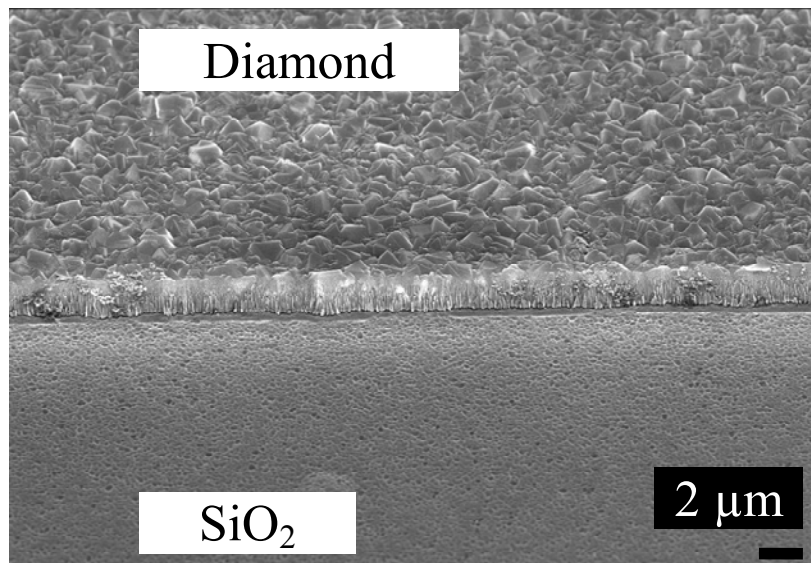


Figure 4-11. The diamond sample patterned using 2 step etching. Oxide layer is well protected and its roughness is only 20-30 Å.

## 4.5 **Summary**

In this chapter, poly-C micromachining technologies are developed and discussed in detail. These technologies are specially developed in order to address the problems associated with poly-C probe fabrication and also diamond MEMS. Examples include diamond nucleation on Si and SiO<sub>2</sub> surfaces, and inadvertent SiO<sub>2</sub> etching during diamond growth and etching. This is the first time that these issues, which are important in poly-C probe fabrication, are discussed.

# Chapter 5

## Poly-C Probe Technology

### 5.1 Introduction

A Poly-C probe is a novel idea in both MEMS and neuroscience. It utilizes, for the first time, polycrystalline diamond as the probe substrate, interconnect material and electrode material. As discussed in the last section, the harsh environment in the MPCVD chamber during growth limits the integration of diamond into MEMS technologies. Therefore, the design and fabrication processes of poly-C probes must be specifically developed as presented in this chapter.

In this chapter, the design and fabrication processes of two types of poly-C probes are presented. The first type is a probe which is to be used for electrical recording of neural activity, called the *EL probe*. This probe has eight poly-C electrodes. The other type of probe is to be used for electrochemical recording and is called the *EC probe*. This probe has Au counter electrodes, Ag/AgCl reference electrodes and poly-C working electrodes.

## 5.2 Design

In total, nine masks have been designed for the fabrication of the EL and EC probes as listed in Table 5-1. Depending on the type of probe (e.g. EL or EC) and the materials used for the interconnects/leads (e.g. poly-C or Au), a different number of masks are needed. Specifics are discussed in later sections. An example of the mask layout is shown in Figure 5-1. In the layout, there are different types of poly-C probes; there are EL, EC, cochlear and cholesterol probes. The EL probe has eight poly-C sites; the EC probe has 2 sets of three-electrodes (poly-C, Ag/AgCl and Au) for a total of six electrodes. The cochlear and cholesterol probes have poly-C piezoresistors along their probe shank. In this research, EL and EC probes are the major focus. In the mask design, there are also regions for resistivity testing and contact resistance testing.

Table 5-1. A list of the nine masks used in this project.

| <b>Mask gds #</b> | <b>Layer name</b> | <b>Description</b>                                       |
|-------------------|-------------------|--|
| 1                 | BDD               | Deep boron diffusion for the definition of probe backend |
| 2                 | BDP               | Define highly doped diamond electrodes/interconnects     |
| 3                 | PP                | Define diamond piezoresistors                            |
| 4                 | UDP               | Define undoped diamond probe patterns                    |
| 5                 | REP               | Define reference electrodes                              |
| 6                 | CEP               | Define counter electrodes                                |
| 7                 | IP                | Define metal or diamond interconnects                    |
| 8                 | TIP               | Define top layer insulators                              |
| 9                 | CPP               | Define contact pads for the probe                        |

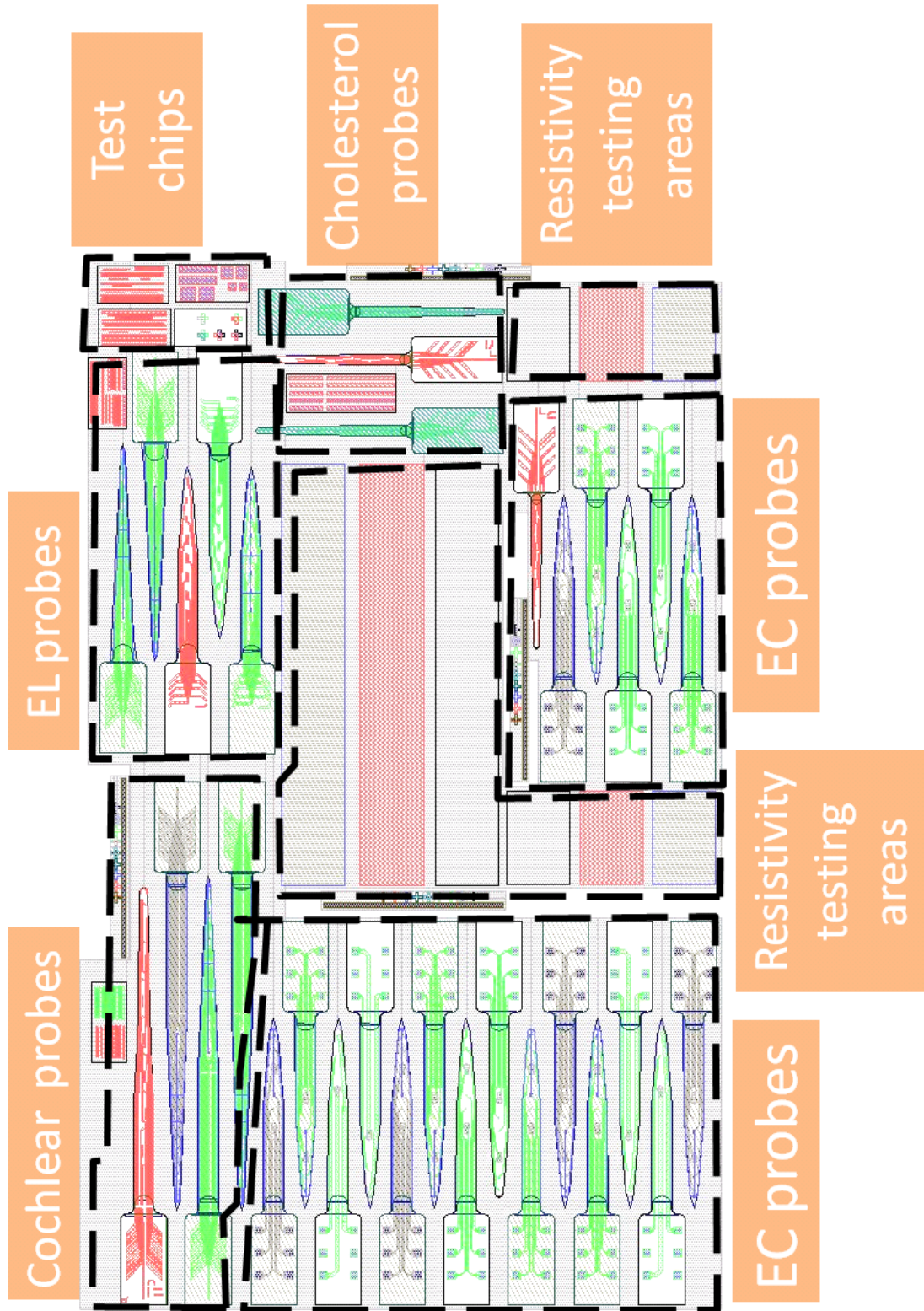


Figure 5-1. Mask layout for different types of diamond probes.

### 5.2.1 Electrical Neural Probe

A schematic of the probe (depicted in Figure 5-2) reveals details of the probe's dimensions used in the design, which requires a six-mask fabrication process. The front end of the fabricated probes is semitransparent and flexible. Several designs of the diamond probes have been studied ranging from all-diamond (in which the front end is made out of poly-C only) to diamond-based (in which the front end is not completely made out of poly-C).

Usually, the structural material of the probe, as shown in Figure 5-2, is poly-C (thickness = 3  $\mu\text{m}$ ) which provides strong mechanical support which is important during *in vivo* insertion. The probe has a pointed tip with a tip angle of  $30^\circ$  which enhances the penetration abilities of the probe in terms of biological entities. It has eight highly boron doped poly-C electrodes with diameters ranging from 2 to 150  $\mu\text{m}$  [138]. These electrodes, which are made of poly-C, act as the sites for physiological signal recording. Leads connected between the sites and metal (i.e. Ti/Au) bonding pads communicate with outside circuits and systems. The resistivity of the poly-C films used as electrode and lead material is in the range of  $5 \times 10^{-2} - 10^{-3} \Omega\text{-cm}$  [138][139]. The undoped poly-C resistivity is in the range of  $10^5 - 10^8 \Omega\text{cm}$ . The backend of the probe is also made of undoped poly-C supported by thick (thickness = 15  $\mu\text{m}$ ) highly boron doped silicon. Shown in the Table 5-2 are the selected masks needed for the fabrication of EL probes.

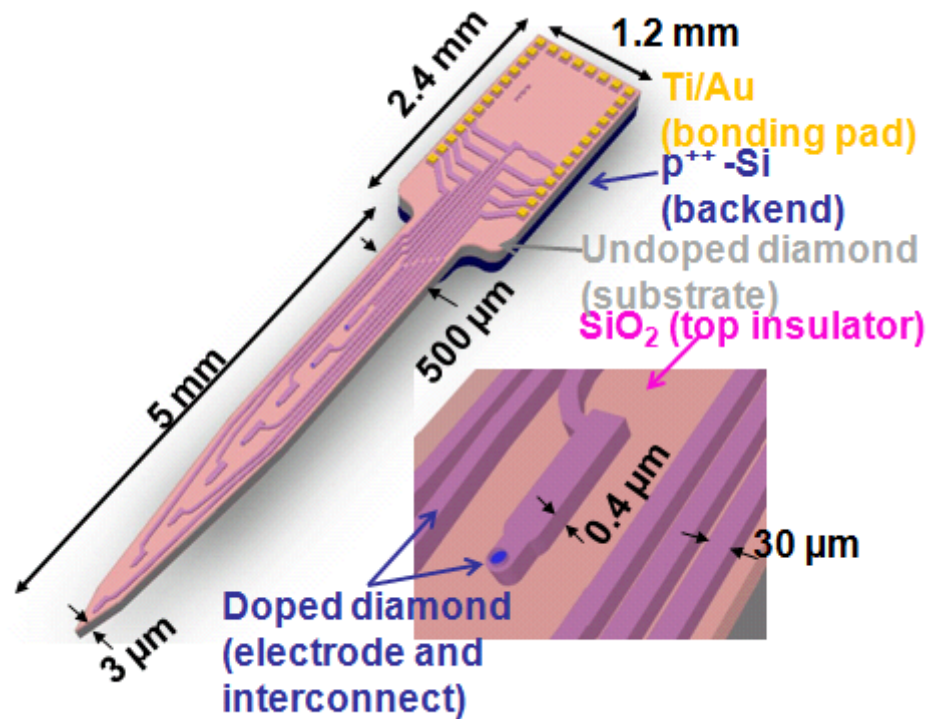


Figure 5-2. Design of the EL probe.

Table 5-2. The six masks used in the fabrication of EL probes.

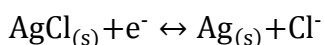
| Mask gds # | Layer name | Description   |
|------------|------------|---|
| 1          | BDD        | Define backend of a probe   |
| 2          | BDP        | Define interconnects and boron doped poly-C electrodes                |
| 4          | UDP        | Define undoped poly-C probe shank/ SiO <sub>2</sub> layer             |
| 8          | TIP        | Define top SiO <sub>2</sub> insulator which exposes poly-C electrodes |
| 9          | CPP        | Define bonding pads on the probe backend                              |

## 5.2.2 Electrochemical Neural Probe

The design of the EC probe is similar to that of the EL probe. This probe is used for electrochemical detection and thus, it contains three different types of electrodes: the counter electrodes (Au), reference electrodes (Ag/AgCl) and working (poly-C) electrodes. Each probe has two sets of these three electrode setups. The interconnects are made of Au. The schematic of the electrochemical probe is shown in Figure 5-3, and the masks required are listed in Table 5-3.

Gold is chosen as the material for the counter electrode because of its inertness. The Au electrode is used to complete the circuit in an electrochemical setup and therefore, any reaction taking place at its surface is not of interest. However, the size of the counter electrode should be big enough in order to prevent any electron transfer limitations in the electrochemical circuit. The magnitude of current, and thus the rate of electron transfer, depends on the electrode area. If it is too small as compared to the working electrode, it will impose a limitation on the current across the working electrode. Therefore, as compared to the poly-C electrode ( $D = 4 \mu\text{m}$ ), the Au electrode is larger ( $D = 80 \mu\text{m}$ ) in the electrochemical probe design. Its position on the probe is not a crucial issue as compared to the reference electrode.

Ag/AgCl is used as the material for the reference electrode. One of the most important reasons for this choice of material is the ease of fabrication as compared to other reference electrodes such as standard hydrogen reference electrode. It can provide a constant potential reference (0.222 vs. NHE) for the poly-C electrode regardless of the electrolyte. The reaction that takes place is:



Since the Ag/AgCl electrode draws no current from circuit, it acts as a potential reference. It must be positioned near the poly-C electrode on the probe. Otherwise, the measured potential between the working and reference electrodes is the sum of the potential of poly-C electrode (as referenced to the reference electrode) and the voltage ( $iR$ ) drop in the electrolyte between the poly-C and Ag/AgCl electrodes. In this probe design, the Ag/AgCl electrode is placed close to the working electrode as compared to the Au electrode.

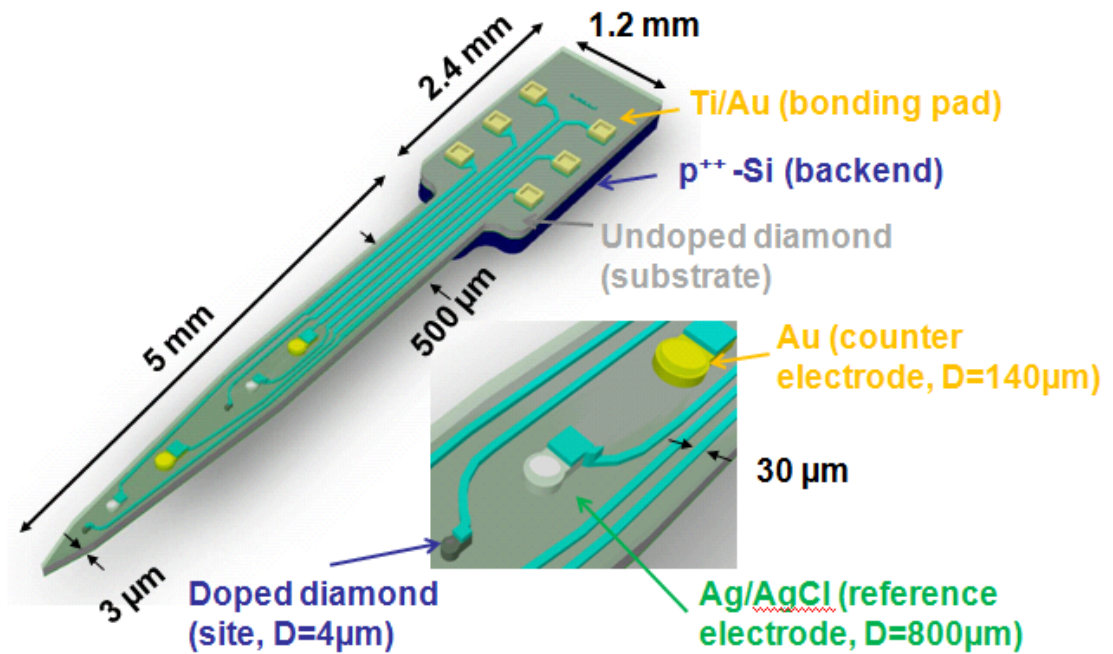


Figure 5-3. Design of the EC probe.

Table 5-3 The eight masks used in the fabrication of electrochemical neural probes

| Mask gds # | Layer name | Description  |
|------------|------------|--|
| 1          | BDD        | Define backend of a probe  |
| 2          | BDP        | Define poly-C working electrodes   |
| 4          | UDP        | Define undoped poly-C probe shank/ SiO <sub>2</sub> layer                          |
| 5          | REP        | Define Ag/AgCl reference electrodes  |
| 6          | CEP        | Define Au counter electrodes   |
| 7          | IP         | Define Ti/Au interconnects   |
| 8          | TIP        | Define top SiO <sub>2</sub> insulator which exposes Ag/AgCl, Au, poly-C electrodes |
| 9          | CPP        | Define bonding pads on the probe backend   |

## 5.3 Fabrication

### 5.3.1 Electrical Neural Probe

Shown in Figure 5-4 is the fabrication process of EL probes (i.e. all-diamond probes and poly-C probes with metal leads). A more detailed procedure can be found in Appendix A. The process starts with a bare n-type silicon wafer. A layer of 1.2  $\mu\text{m}$  thick thermal oxide was grown on top of the wafer as an intermediate step for patterning the highly boron doped Si areas, which served as the backends of the diamond probes. As undoped poly-C growth directly on boron doped Si increases the conductivity of the poly-C due to boron out diffusion (during diamond growth) from Si and the corresponding boron incorporation into poly-C as discussed in the last section, a layer of silicon dioxide (SiO<sub>2</sub>) was grown on top of the Si wafer to prevent boron out diffusion. It is found that the difference in the resistivities of poly-C films grown on Si substrates with and without SiO<sub>2</sub> protection can be 2 orders in magnitude. Therefore, SiO<sub>2</sub> is an essential

layer for diamond growth on a boron doped silicon substrate (Figure 5-4a). Next, undoped (3  $\mu\text{m}$ ) and doped (1  $\mu\text{m}$ ) poly-C films were grown using the method mentioned in the previous section with resistivities of  $\sim 10^5 \Omega\text{cm}$  and  $\sim 10^{-3} \Omega\text{cm}$ , respectively (Figure 5-4b). Aluminum (700nm) was used as the mask for etching as mentioned above (Figure 5-4c). The Al mask was washed away by Aluminum Etch Type A solution. The undoped poly-C film served as the substrate for the probe, while the doped poly-C film was used as the electrodes and leads.

In the case of using metal as the lead material, an additional step is added to pattern a Ti/Au (50 nm/300 nm) layer (Figure 5-4 (c')). Then, a 1.4  $\mu\text{m}$   $\text{SiO}_2$  layer is deposited using GSI plasma enhanced chemical vapor deposition (PECVD). This layer was patterned and etched using buffered oxide solution in order to expose the contact pads located on the backend and the poly-C electrodes (Figure 5-4d). A layer of titanium/gold (50 nm/300 nm) was then deposited and patterned to form the contact pads (Figure 5-4e). Finally, the Si substrate was thinned by HF-nitric (HNA) down to 200  $\mu\text{m}$  and the probes were released by the ethylene-diamine-pyrocatechol (EDP) process (Figure 5-4f) with boron etch stop. A fabricated all-diamond probe is shown in Figure 5-5.

. The all-diamond front end of the probe is flexible in the out-of-plane direction (Figure 5-6(a)) and also it can easily be twisted without breaking (Figure 5-6(b)). The flexibility is advantageous in terms of brain implants since the probe must not break during insertion.

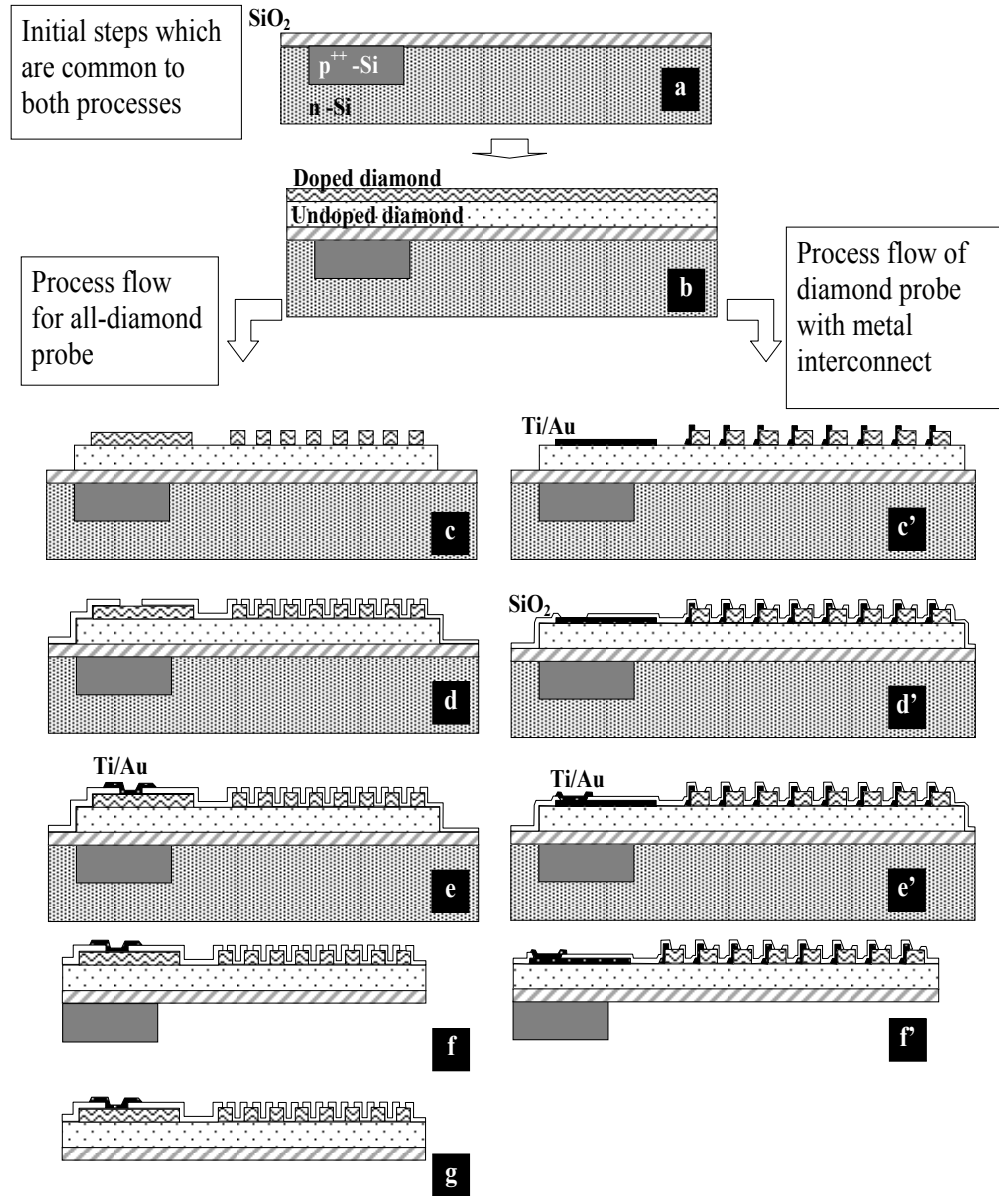


Figure 5-4. Fabrication process of all-diamond probes.

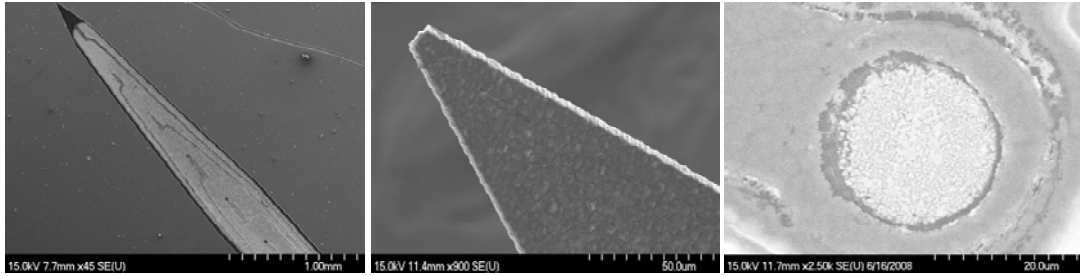
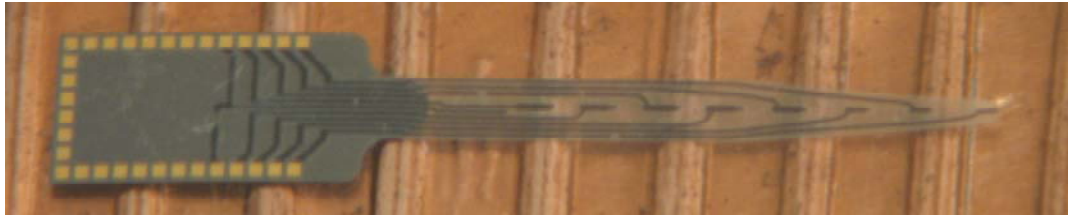
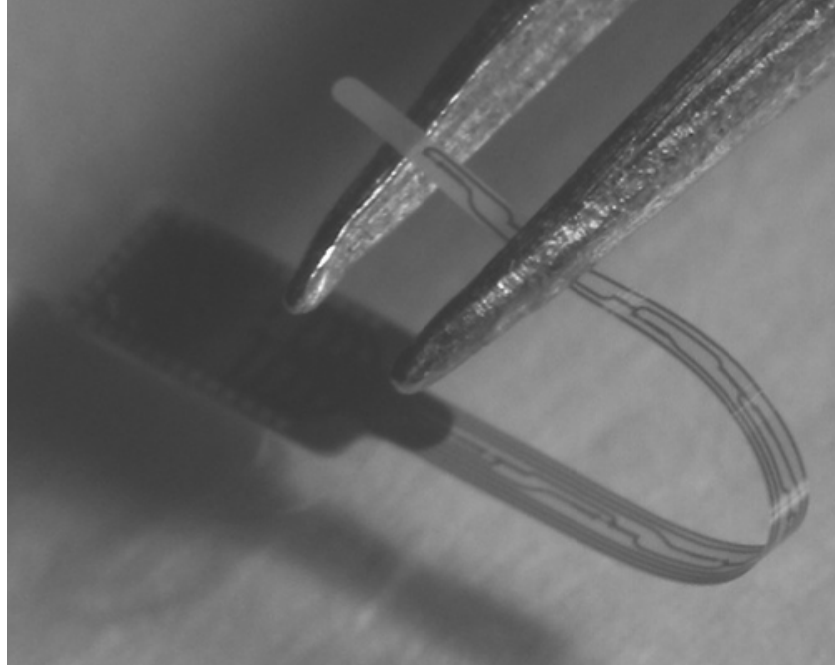
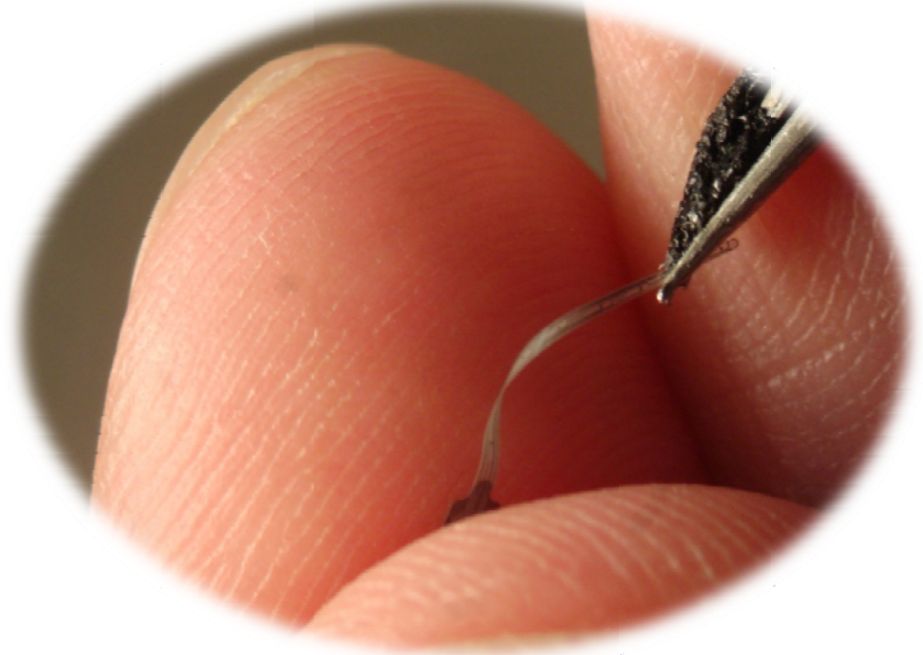


Figure 5-5. Released all-diamond probe on a US penny. The highly doped Si back end was removed in this probe.



(a)



(b)

Figure 5-6. An all-diamond probe was bent in the out-of-plane direction with a pair of tweezers (bending angle was larger than  $180^\circ$ ).

### 5.3.2 Electrochemical Neural Probe

The fabrication process used for the EC probe is shown in Figure 5-7. The first four steps of the process are exactly the same as that of the EL probe. In summary, a group of undoped/doped diamond layers is grown on top of an SiO<sub>2</sub> substrate. Then, these layers are etched using RIE with aluminum (1 μm) as the masking layer. For the EL probes, highly boron doped diamond is used as the working electrode (Figure 5-7d). The metal stack for the reference electrode is Ti/Au/Ag which have thicknesses of 40 nm/10 nm/300 nm and are patterned using sputtering and a lift off process. The Ti/Au layer underneath the Ag is used to provide adhesion between doped diamond and Ag. Formation of Ag/AgCl is performed after the probe release. The materials for counter electrode and leads are Ti/Au using lift off process. Then, a layer of PECVD oxide was deposited on top with the three electrodes and bonding sites exposed. Ti/Au bonding pads were patterned on the very top layer. Finally, the probe was released by HF-nitric and EDP process. Shown in Figure 5-8 is a fabricated EC probe which has two sets of electrodes (i.e. working, counter and reference).

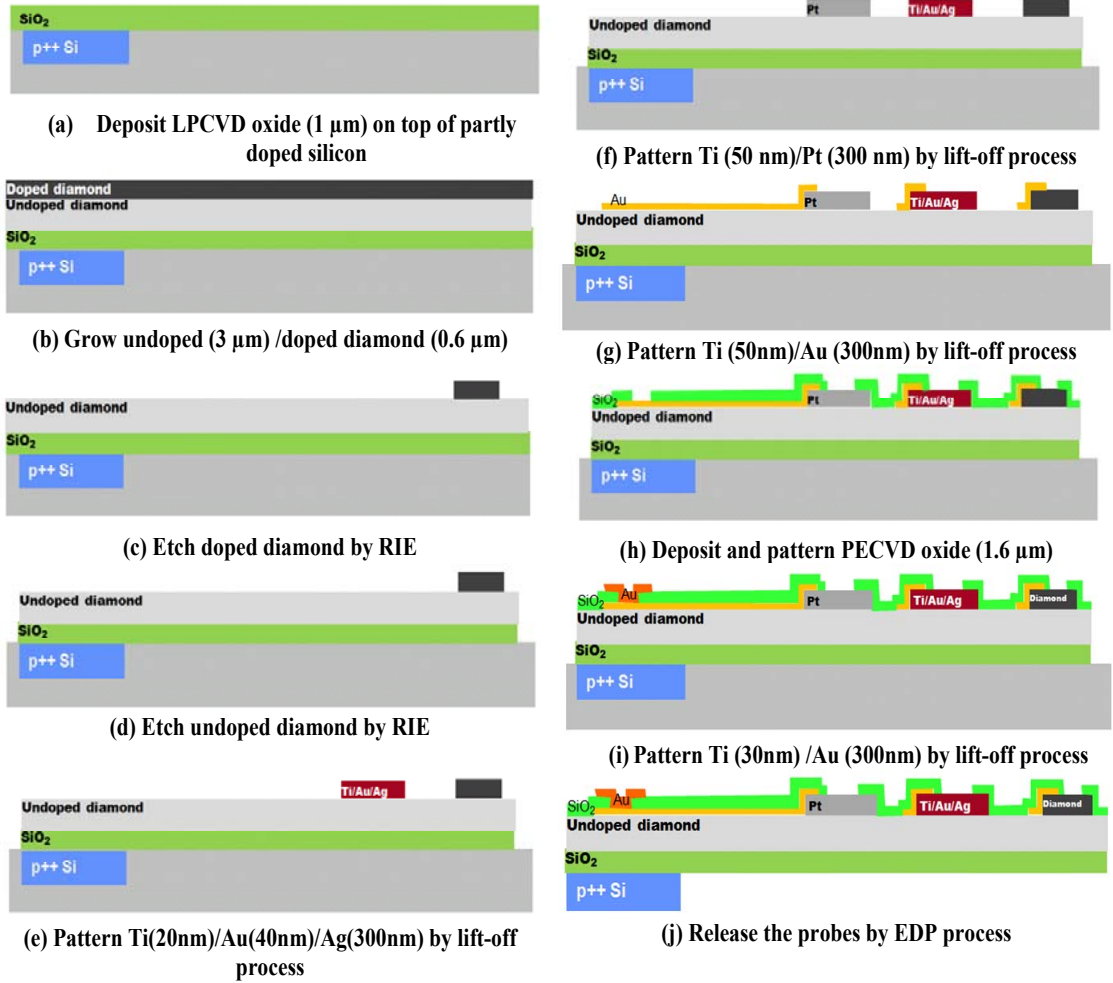


Figure 5-7. Fabrication process of the EC probe.

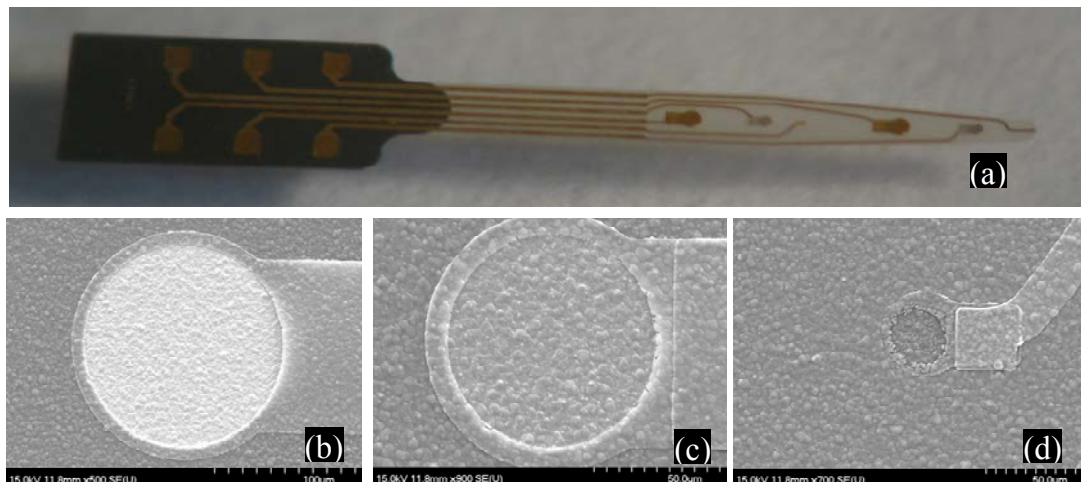


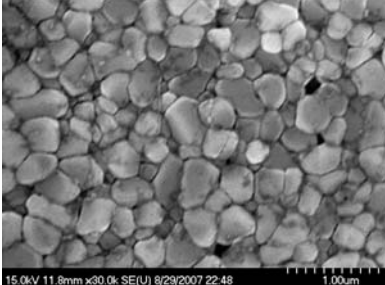
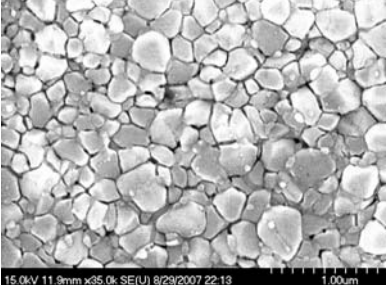
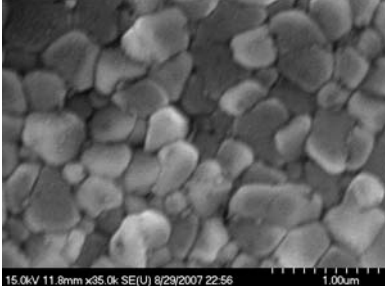
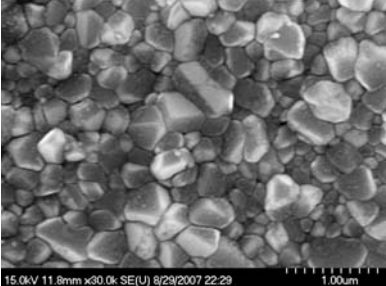
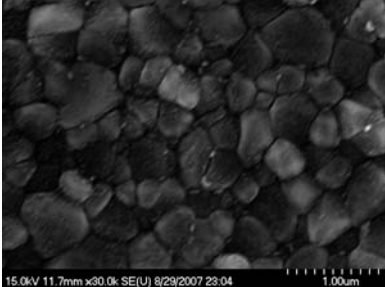
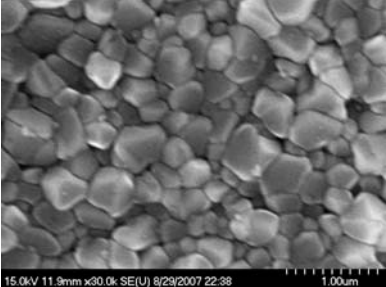
Figure 5-8. (a) A fabricated EC probe, which has an (b) Au counter electrodes, (c) Ag/AgCl reference electrodes and a (d) poly-C working electrodes.

After the EC probe is released, the last step of the fabrication process is the formation of AgCl on top of Ag electrode surface. There are different ways to form AgCl from Ag [140]. For example, anodization of Ag in chloride-containing solutions, chemical oxidation, and thermal or plasma treatment in chloride-containing atmospheres. The chemical oxidation of Ag in aqueous  $\text{FeCl}_3$  is chosen as the formation method in this project because this process is compatible with the probe fabrication process and is easily performed. The EC probe was immersed in ferric chloride  $\text{FeCl}_3$ . SEM images of AgCl formation on Ag electrodes under different  $\text{FeCl}_3$  concentrations and immersion times are shown Table 5-4. It is observed that the average grain size of AgCl increases with increasing  $\text{FeCl}_3$  concentration and reaction time.

One of the problems associated with the use of an Ag/AgCl electrode is that it requires a constant source of chloride in order to maintain its constant potential. In other

word, it must always be immersed in a chloride rich solution (e.g. KCl) to maintain its potential. Otherwise, the AgCl may dissolve completely if the probe is immersed for a long period of time. These facts suggest a stability problem relating to the Ag/AgCl electrode in an aqueous environment. If the stability of the electrode cannot be maintained, its potential will change with respect to time and therefore, there will no longer be a fixed reference for electrochemical measurements. Typically, it is observed that the Ag/AgCl electrode is stable for a time period in the range of a few minutes to a few hours [141]. One way to lengthen the electrode's maximum immersion time is to coat the Ag/AgCl electrode with a gel or polymer material (e.g. Nafion or polyurethane) [142][143][144]. This creates a diffusion barrier between the Cl<sup>-</sup> ions dissolved from the electrode to the electrolyte, and therefore, lowers the rate at which the AgCl dissolves.

Table 5-4. AgCl formation on Ag electrodes using FeCl<sub>3</sub>.

| Dipping Time (s) | 1M FeCl <sub>3</sub>   | 50mM FeCl <sub>3</sub>   |
|------------------|--|--|
| 30               |  <p>15.0kV 11.9mm x30.0k SE(U) 8/29/2007 22:48 1.00um</p>   |  <p>15.0kV 11.9mm x35.0k SE(U) 8/29/2007 22:13 1.00um</p>   |
| 60               |  <p>15.0kV 11.8mm x35.0k SE(U) 8/29/2007 22:56 1.00um</p>  |  <p>15.0kV 11.8mm x30.0k SE(U) 8/29/2007 22:29 1.00um</p>  |
| 120              |  <p>15.0kV 11.7mm x30.0k SE(U) 8/29/2007 23:04 1.00um</p> |  <p>15.0kV 11.9mm x30.0k SE(U) 8/29/2007 22:38 1.00um</p> |

## 5.4 Probe Mounting and Packaging

To increase the ease of accessing sites on the poly-C probe, the probe is mounted on a printed circuit board (PCB) which extends the leads and connects easily with outside circuits or systems as shown in Figure 5-9. The probe is mounted on the PCB using Crystalbond 200 which is a low temperature adhesive gel. Then, the wire bonding is

performed using an aluminum wedge bonder which connects the pads on the probe to that of the PCB. Finally, for the purpose of *in vivo* testing, the wires and the backend of the probe are encapsulated by an optically transparent silicone elastomer from Silicone Technology. This encapsulation provides electrical and chemical isolation of the wires and the backend from the working environment.

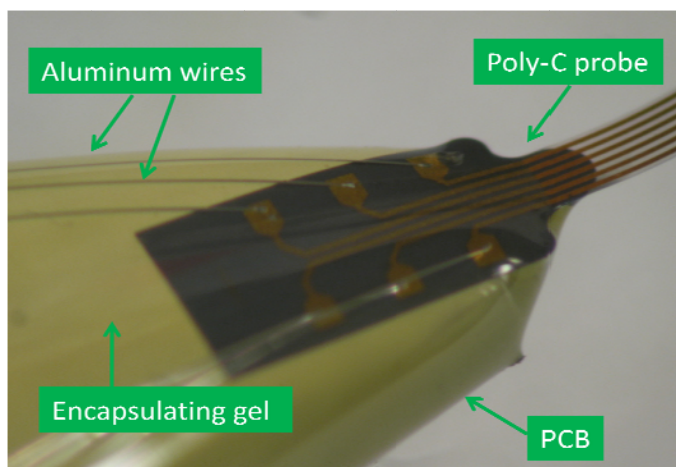


Figure 5-9. Probe mounting.

## 5.5 Summary

Two types of poly-C probes, EL and EC probes, are presented for the first time. The EL probe consists of eight poly-C sites (with resistivities of  $\sim 10^{-3} \Omega\text{cm}$ ) which are used for electrical recording. The lead material can be either doped poly-C or Au. The EC probe, on the other hand, has three types of electrodes (i.e. Ag/AgCl reference electrodes, Au counter electrodes and poly-C working electrodes) used for electrochemical recording. The probe shank is undoped poly-C with a resistivity of  $\sim 10^5 \Omega\text{cm}$  in both cases. The fabricated poly-C probes are then mounted on a PCB in order to interface with external systems.

# Chapter 6

## Characterizations and Applications of Poly-C Probes

### 6.1 Introduction

The common techniques for characterizations of an electrode include Electrical Impedance Spectroscopy (EIS) and Cycle Voltammetry (CV). Electrical Impedance Spectroscopy is used for electrode electrical modeling which characterizes the electrode's behavior across a wide range of frequencies [85][145]. Cyclic Voltammetry, on the other hand, is used for studying electrode reactions, which yield information not only on the thermodynamics of reactions but also on kinetic parameters (e.g. heterogeneous electron-transfer rate constant). In this chapter, EIS and CV will be discussed in detail in the first two sections. In the later two sections, two applications of the poly-C neural probes will be discussed: electrochemical recording of neurotransmitters and electrical recording *in vivo*.

## 6.2 Poly-C Site Characterizations

### 6.2.1 Electrical Impedance Spectroscopy

Electrical Impedance spectroscopy (EIS) is a technique used to characterize an electrode, in an electrical sense, for small signal perturbations ( $V_{pp} < 0.05$  V). Together with an appropriate equivalent circuit model for the electrode/electrolyte interface, parameters such as interfacial capacitance and charge transfer resistance can be obtained. Since a small perturbation is applied to the electrode, the electrode is working close to equilibrium and thus, a linear current-voltage response is obtained. The measurement is performed over a wide range of frequencies (1 Hz to 100 kHz). The magnitude of the electrical impedance  $Z$  and phase angle  $\theta$  are recorded at each frequency. The impedance,  $Z$ , can be represented as,

$$Z = Z' - jZ'' \quad (13)$$

where  $Z'$  ( $>0$ ) and  $Z''$  ( $>0$ ) are the real and imaginary parts of the total impedance  $Z$ , respectively. It is realized that the definition of  $Z$  always has a negative imaginary part. This is because the electrode impedance is almost always capacitive as discussed in chapter 3. The phase  $\theta$  is represented by,

$$\theta = \tan^{-1}\left(\frac{Z''}{Z'}\right). \quad (14)$$

As discussed in chapter 3, an electrical double layer is formed when an electrode is placed in an electrolyte. The electrons in the metal and the charged ions close to the electrode surface are attracted to each other and separated by solvent molecules (usually water). This interface acts like a capacitor which charges or discharges depending on the

imposed voltage. The capacitance of this double layer structure governs the electrode's ability to deliver charge (in electrical stimulation) and its background current (in electrical and electrochemical detection).

For the model used in this project, the Warburg impedance and the double layer capacitance in the Randles model are replaced by two constant phase elements (CPE,  $W$  and  $Q$ ) which results in a better curve fitting, and therefore a more accurate representation of the electrode in this study. The constant phase element has a constant phase different from an ideal capacitor and its impedance is defined by the following equation.

$$Z_{CPE} = \frac{1}{(j\omega C)^n} \quad (15)$$

The modified equivalent circuit for the electrode/electrolyte model is shown in Figure 6-1. The total impedance is given by,

$$Z = R_s + \frac{Q(R_t+W)}{W+Q+R_t} \quad (16)$$

$$\text{where } Q = \frac{1}{(j\omega C_{dl})^\alpha}, W = \frac{1}{(j\omega C_w)^\beta} \text{ and } 0 \leq \alpha, \beta \leq 1.$$

After  $Q$  and  $W$  are substituted in, the total impedance is given by,

$$Z = \underbrace{\left( R_s + \frac{B^2 R_t + ABR_t \sin\left(\frac{(\alpha+\beta)\pi}{2}\right) + B \sin\left(\frac{(2\alpha+\beta)\pi}{2}\right) + A \sin\left(\frac{(\alpha+2\beta)\pi}{2}\right) + R_t \cos\left(\frac{(\alpha+\beta)\pi}{2}\right) + BR_t^2 \cos\left(\frac{\alpha\pi}{2}\right)}{B^2 + A^2 + R_t^2 + 2AB \sin\left(\frac{\alpha+\beta}{2\pi}\right) + 2BR_t \cos\left(\frac{\alpha\pi}{2}\right) + 2AR_t \cos\left(\frac{\beta\pi}{2}\right)} \right)}_{Z'} + \underbrace{j \frac{ABR_t \sin\left(\frac{(\beta-\alpha)\pi}{2}\right) - B \sin\beta - A \sin\alpha - R_t \sin\left(\frac{(\alpha+\beta)\pi}{2}\right)}{B^2 + A^2 + R_t^2 + 2AB \sin\left(\frac{\alpha+\beta}{2\pi}\right) + 2B_t \cos\left(\frac{\alpha\pi}{2}\right) + 2AR_t \cos\left(\frac{\beta\pi}{2}\right)}}_{Z''} \quad (17)$$

The phase of  $Z$  can be computed by  $\tan^{-1}\left(\frac{Z''}{Z'}\right)$ , which becomes,

$$\theta = \tan^{-1} \frac{ABR_t \sin\left(\frac{(\beta-\alpha)\pi}{2}\right) - B\sin\beta - A\sin\alpha - R_t \sin\left(\frac{(\alpha+\beta)\pi}{2}\right)}{B^2 R_t + ABR_t \sin\left(\frac{(\alpha+\beta)\pi}{2}\right) + B\sin\left(\frac{(2\alpha+\beta)\pi}{2}\right) + A\sin\left(\frac{(\alpha+2\beta)\pi}{2}\right) + R_t \cos\left(\frac{(\alpha+\beta)\pi}{2}\right) + BR_t^2 \cos\left(\frac{\alpha\pi}{2}\right)}$$

(18)

where  $A = (\omega C_{dl})^\alpha$  and  $B = (\omega C_w)^\beta$ .

At low frequencies, the total impedance  $Z$  is dominated by the Warburg impedance, which represents the mass transfer of ions to and from the electrode, and becomes approximately,

$$Z_l = R_s + R_t + \frac{1}{(j\omega C_w)^\beta} \quad (19)$$

This corresponds to a straight line with a slope of  $\tan\left(\frac{\pi\beta}{2}\right)$  in the Nyquist plot.

On the other hand, at high frequencies, the effect of the Warburg impedance is no longer significant as compared to that of the double layer capacitance. Therefore, the total impedance becomes approximately,

$$Z_h = R_s + \frac{R_t}{1 + R_t(j\omega C_{dl})^\alpha} \quad (20)$$

This corresponds to the semi-circle in the high frequency range of the Nyquist plot as discussed in chapter 3.

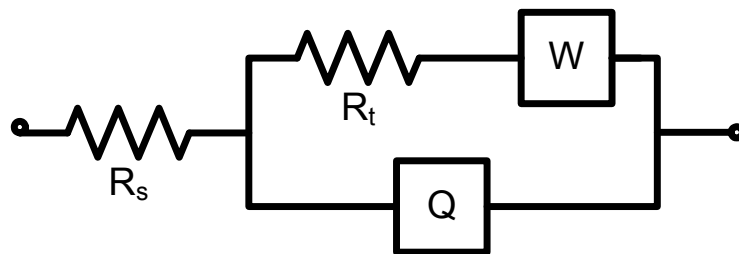


Figure 6-1. Modified Randles model of the electrode/electrolyte interface [85].

To measure the impedance spectrum, the poly-C probe is mounted as explained in the previous chapter and placed in 0.9% saline solution (9000 mg NaCl: 1000 ml DI H<sub>2</sub>O); the poly-C site acts as the working electrode. The reference and counter electrodes are commercially available Ag/AgCl and platinum electrodes, respectively. The measurement is performed inside a Faraday cage in order to minimize noise from external sources as shown in Figure 6-2. The electrochemical station CH 750C from CH Instruments which has the ability to do EIS was used.

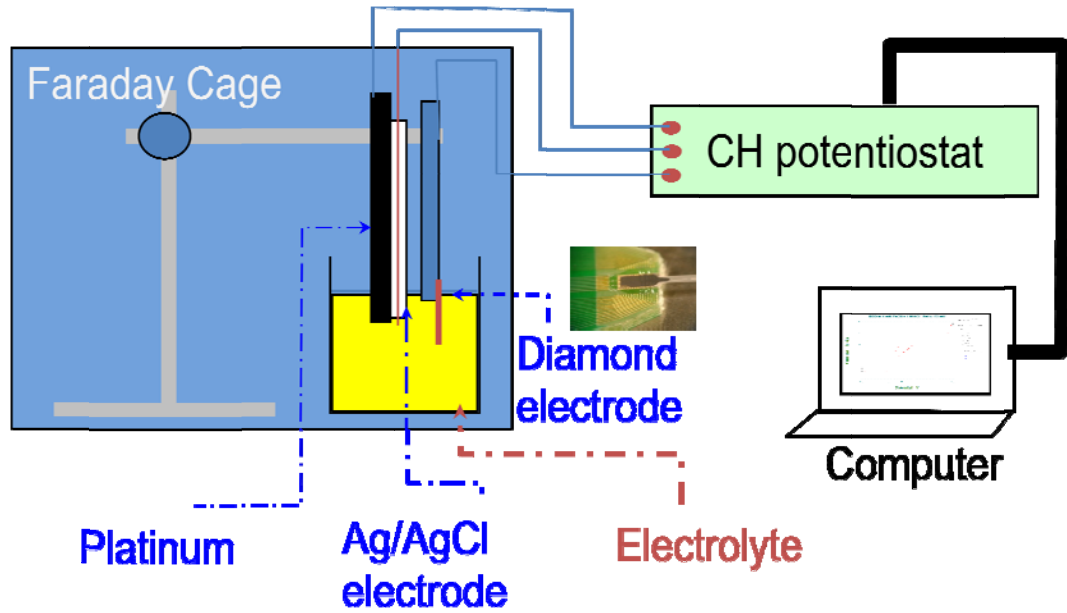


Figure 6-2. Experimental setup for the EIS measurements.

In this measurement, a small signal of (5 mVpp) was applied to the poly-C electrode, and divided by the induced current to find  $Z'$  and  $Z''$ . The Nyquist and Bode plots in the frequency,  $\omega$ , range of 0.1 – 100 kHz are shown in Figure 6-3. The predicted total impedance is described by (16). Least squares curve fitting was performed to obtain the model parameters ( $R_s$ ,  $R_t$ ,  $W$  and  $Q$ ). The error is defined as:

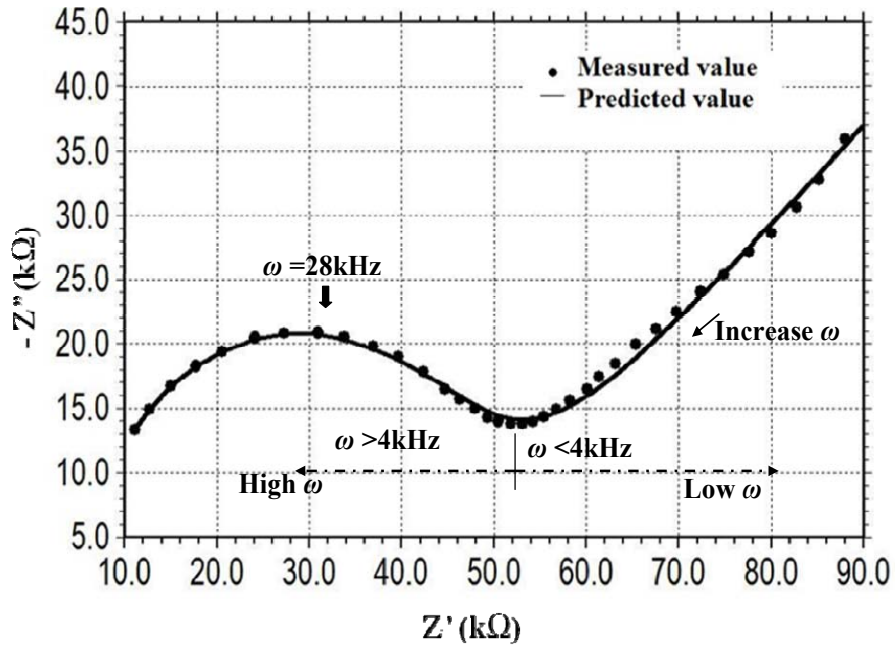
$$e = \sum_{i=1}^N \frac{(Z_{\text{predicted},i} - Z_{\text{measured},i})^2}{Z_{\text{measured},i}^2} \quad (21)$$

where  $N$  is the total number of data points.

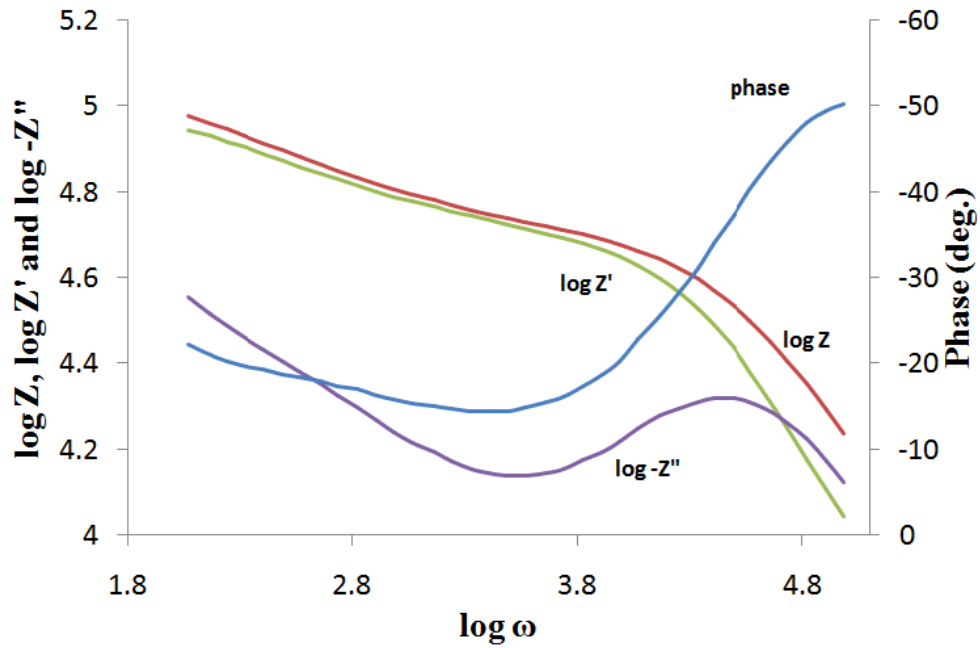
In this method, the function  $e$  is minimized by adjusting the model parameters; the optimal parameters obtained are listed in Table 6-1. At low frequencies ( $< 4$  kHz), both the real and imaginary parts of the total impedance  $Z$  decrease with increasing frequency, and  $Z$  has a negative phase  $\theta$  throughout the spectrum as shown in Figure 6-1(a). This

indicates that the electrode behaves capacitively. This low frequency behavior is described by the Warburg impedance term, in (4), which is defined as a constant phase element ( $\beta=0.43$ ). This element describes the ions movement in the bulk solution to and from the electrode interface. The impedance becomes more resistive (i.e.  $\theta$  changes from  $-23^\circ$  to  $-15^\circ$ ) as the frequency increases as shown in Figure 6-1(b). The cutoff frequency is around 4 kHz at which point the impedance enters the high frequency regime which can be described by (5);  $\theta$  reaches its minimum. The impedance becomes more capacitive again (i.e.  $\theta$  changes from  $-15^\circ$  to  $-50^\circ$ ) at high frequencies ( $> 4$  kHz) as shown in Figure 6-1 (b). In this region, the double layer capacitance  $Q$  and charge transfer resistance  $R_t$  dominate in the total impedance  $Z$ . In other words, the current is mainly due to the charging of the double layer at the electrode/electrolyte interface at high frequencies. It is noted that there is no further decrease in  $\theta$  within the measurable frequency range of the equipment. Thus, the poly-C electrode behaves similar to a capacitor within the frequency range of 0.1 – 100 kHz for small signal perturbations. The double layer capacitance  $C_{dl}$  as obtained from fitting the measured data to the electrical model, is  $\sim 87 \mu\text{F}/\text{cm}^2$  which is within the range of reported values (3 - 100  $\mu\text{F}/\text{cm}^2$ ) [146][147]. This normalized capacitance is calculated using the geometric area of the electrode. In the case of a poly-C site, the effect of its surface roughness on the double layer capacitance can be significant-- especially in the high frequency regime. This is because the thickness of the interfacial double layer structure can be less than 5 nm [8]. Thus, the true double layer capacitance can be lower by a factor of 3 to 10 if the roughness of diamond is considered [146]. Polishing the diamond surface is one way to address this issue. Despite their roughness, diamond electrodes are known to have low double layer capacitance as compared to most

metal electrodes [148]. This helps keep the RC time constant low. Therefore, the time needed to charge and discharge the double layer structure is small which is important in terms of *in vivo* electrochemical detection as fast scan voltammetry is often used. Also, the background current, as discussed in the next section, can be lower due to the small double layer capacitance.



(a)



(b)

Figure 6-3. Impedance spectrum for a diamond electrode with diameter of 30  $\mu\text{m}$ , (a) Nyquist plot of the real and imaginary part of the measured impedance, (b) Bode plot.

Table 6-1. Fitted parameters for electrode/electrolyte model.

| Parameters  | Values   |
|---|--|
| Spreading resistance $R_s$ ( $\Omega$ )                         | 4953(=0.03 $\Omega\text{cm}^2$ )                 |
| Charge transfer resistance $R_t$ ( $\Omega$ )                   | $4.02 \times 10^4$ (=0.284 $\Omega\text{cm}^2$ ) |
| Warburg impedance $W$ ( $\text{S sec}^\beta$ )                  | $2.22 \times 10^{-6}$ ( $\beta=0.43$ )           |
| Constant phase impedance $Q$ ( $\text{S sec}^\alpha$ )          | $1.12 \times 10^{-9}$ ( $\alpha=0.95$ )          |
| Double layer capacitance $C_{dl}$ ( $\mu\text{F}/\text{cm}^2$ ) | 87.45  |

## 6.2.2 Cyclic Voltammetry

As discussed in earlier chapters, cyclic voltammetry is a useful tool in studying electrode kinetics and characterizing the electrode's performance. In this section, CV is used to compare the potential window of different materials: diamond, gold, platinum and iridium oxide when they are used as the working electrode. The experimental setup is shown in Figure 6-4. As shown in the figure, a specially designed 25 ml glass flask which has 4 openings is used. The CE and RE electrodes are placed at the top and are immersed in the electrolyte. The third opening at the top can be used to purge oxygen which has dissolved in the electrolyte. The WE is placed such that it covers the bottom opening of the flask. The opening on the bottom of the flask has an area of  $0.2 \text{ cm}^2$ . The metal or diamond films are prepared on top of an Si substrate. These three electrodes are then connected to the potentiostat as mentioned in the last section. The experiment is performed inside the faraday cage.

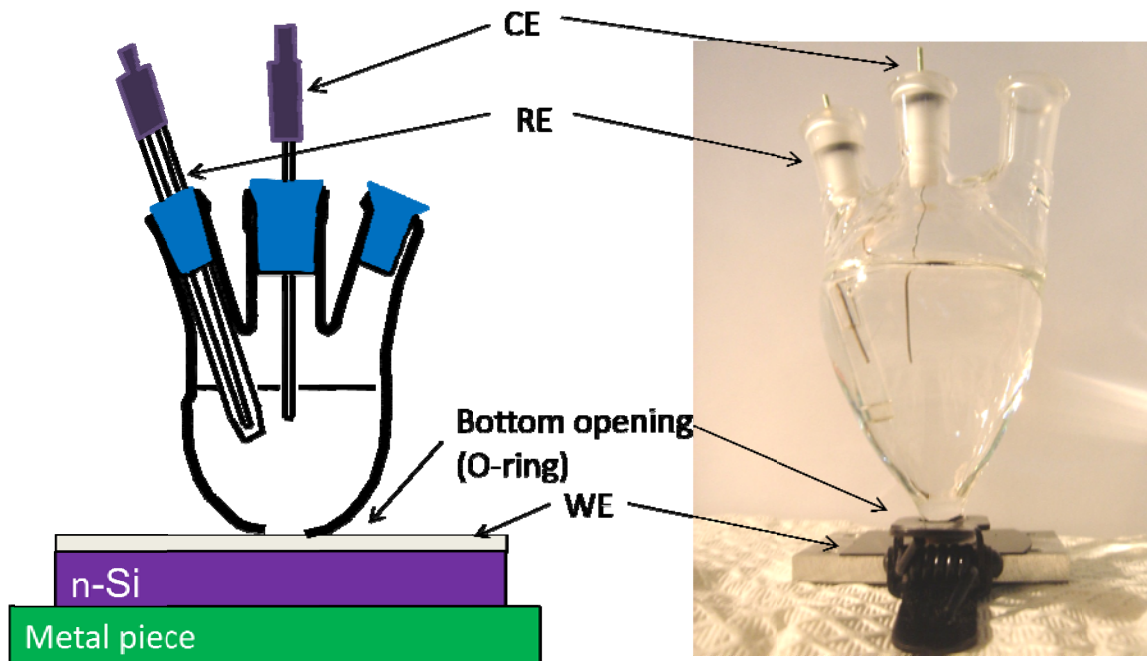


Figure 6-4. Experimental setup for cyclic voltammetry.

In order to compare the performance of diamond electrodes with other electrodes commonly used in neural studies such as Au, Pt and IrO<sub>x</sub> electrodes, a 300 nm thick film of Au, Pt or Ir was deposited on a highly doped Si substrate. IrO<sub>x</sub> was formed by activating Ir in phosphate buffered saline (PBS) solution [149]. The complete procedure for IrO<sub>x</sub> activation is listed in Appendix B. The background current of the electrodes in potassium chloride (KCl), Krebs and PBS solutions are shown in Figure 6-5. It is found that IrO<sub>x</sub> has the largest background current in each of the solvents and exhibits several peaks due to reduction-oxidation reactions that involve the transfer of electrons across the interface [150]. As evidenced by Figure 6-5, IrO<sub>x</sub> not only has a high charge storage capacity and also a large charge injection ability. Therefore, IrO<sub>x</sub> is a material of choice for cell stimulation applications. The reason of the high  $Q_{in}$  associated with IrO<sub>x</sub> is that

the mechanism of its charge injection is the Faradaic reduction and oxidation between the  $\text{Ir}^{3+}$  and  $\text{Ir}^{4+}$  states of the oxide at the electrode surface which correspond to the peaks seen in the CV in Figure 6-5 [27]. Poly-C, on the other hand, shows no peaks and also shows the lowest background current among the materials. This is an advantage- especially for electrochemical detection because the low background current and lack of peaks implies that its surface is chemically inert and stable.

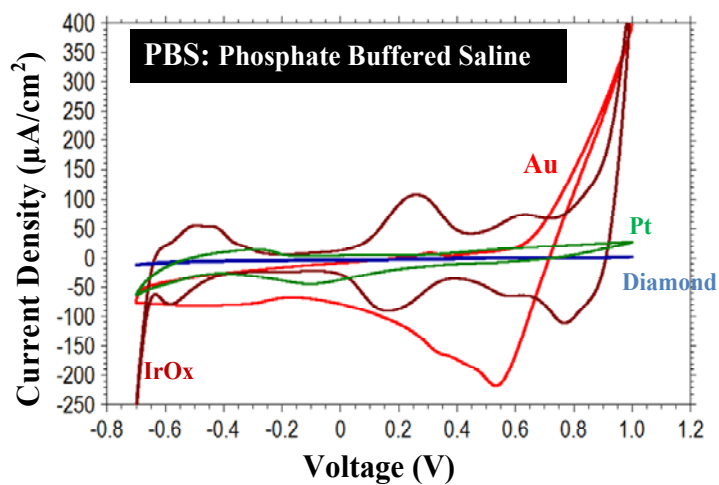
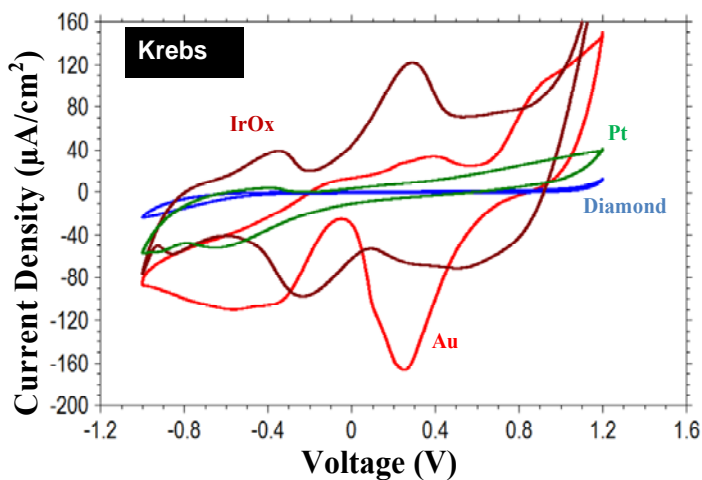
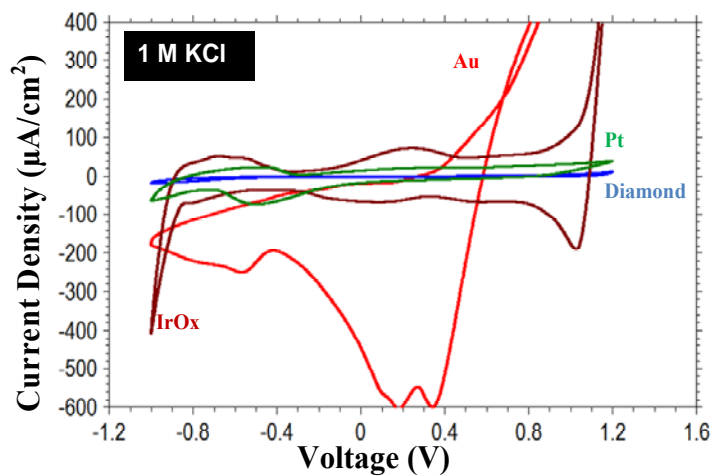


Figure 6-5. Voltammograms of Au, Pt, IrO<sub>x</sub> and diamond electrodes in (a) 1MKCl, (b) Krebs, and (c) PBS.

In addition to low background current, poly-C electrodes also exhibit a wide water potential window. The water potential window is defined as the range between those potentials where oxygen and hydrogen evolution take place. There is no charge transfer across the electrode/electrolyte interface within the potential window. In other words, it is the range of potential where an electrode behaves as an ideal polarized electrode. The potential window can be determined from CV curves recorded using an electrode in an aqueous solution. In an aqueous solution, water (H<sub>2</sub>O) acts as the source for the oxygen and hydrogen that will evolve.. The two chemical reactions are,



A species can only be detected if it undergoes redox reactions at potentials less than that of hydrogen evolution, or greater than oxygen evolution. Therefore, the wider the water potential window an electrode has, the more chemicals it can detect. The potential window of the poly-C site was recorded and is shown in Figure 6-6. The poly-C site on the probe reveals a potential window from -0.8 to 1.4 V in 1M KCl; these overpotentials for both oxygen and hydrogen evolution are relatively high. In other words, there is no current caused by oxygen and hydrogen evolution which would interfere with current from a target species undergoing redox reaction within this range. As a result, the poly-C site is useful in a wide range of potentials, and more species can be detected.

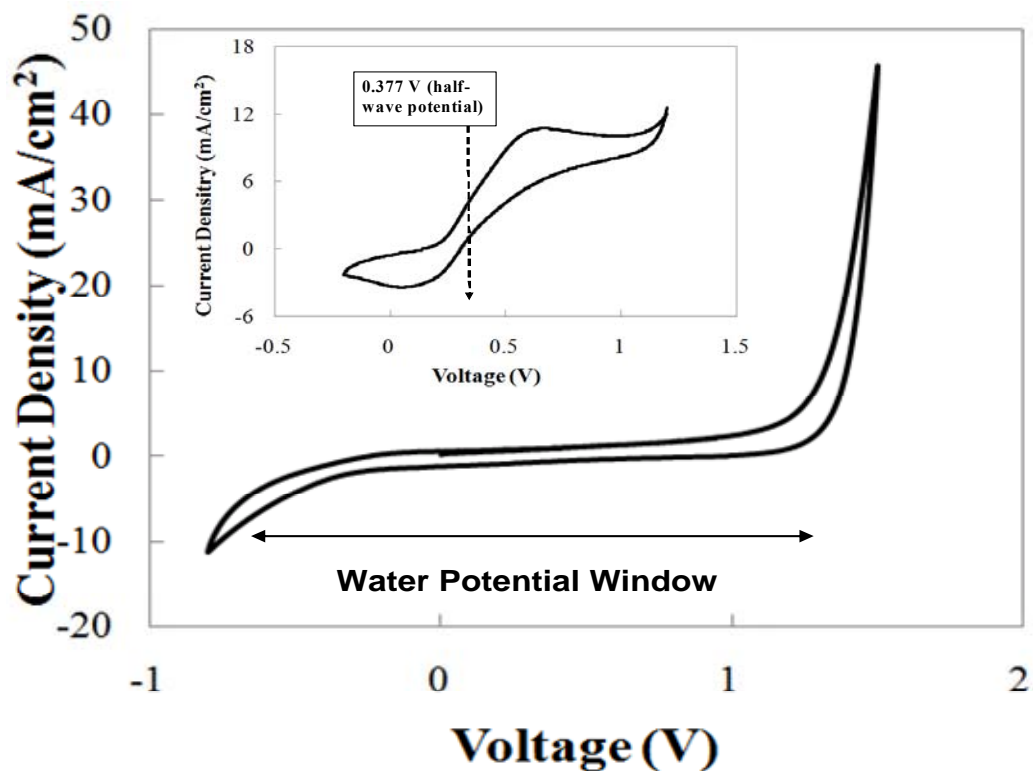


Figure 6-6. Cyclic voltammetry current-voltage curve for the diamond probe in 1M KCl. The insert is the CV of the diamond probe in 1 mM  $\text{Fe}(\text{CN})_6^{4-}$  in 1M KCl. The scan rate was 100 mV/s. The reference and counter electrodes are Ag/AgCl and platinum, respectively.

In diamond related electrochemistry, the  $\text{Fe}(\text{CN})_6^{-3/4}$  redox system has been widely used to evaluate the reactivity of electrodes as they undergo electron transfer via a simple outer-sphere mechanism. In addition, physical and chemical properties of the diamond electrode make the surface highly sensitive to this  $\text{Fe}(\text{CN})_6^{-3/4}$  redox system [25]. Thus, this redox system can be used to compare the quality of different diamond electrodes. The cyclic voltammogram of a poly-C site shown in Figure 6-6 (inset) reveals the half-wave potential  $E_{1/2}$  which is 377 mV (vs. Ag/AgCl). This is the potential at which the value of the current is one half of the difference between the peak current and the residual

current. This figure falls within the range (~ 250 mV to 450 mV) that a typical diamond electrode should exhibit.

### **6.2.3 EC Probes**

Having the success in the fabrication of poly-C electrodes on poly-C probes, two additional electrodes with different materials are integrated to the probe for advance electrochemical testing applications. The two additional electrodes are Ag/AgCl and Au, as discussed in chapter 5, which replace the two commercial metal electrodes used in electrochemical measurement. The main advantage of the EC probe is that the sizes of the three types of electrodes can be minimized, which allows electrochemical detection in small areas. It is especially important in the applications for neural studies.

Preliminary tests have been performed on the EC probe including the CV of the probe in KCl and  $\text{Fe}(\text{CN})_6^{-3/4}$ . Shown in the Figure 6-7 is a comparison of the CV in 1M KCl using (1) three electrodes on EC probe and (2) poly-C site on the probe and commercial CE and RE. It is shown that the shapes of the two curves are almost the same. This shows that the CE and RE on probe work the same as commercial electrodes. The lower in the current for the EC probe may due to the increase in lead resistances in the CE and the difference in the current path in the electrolyte side between the two cases.

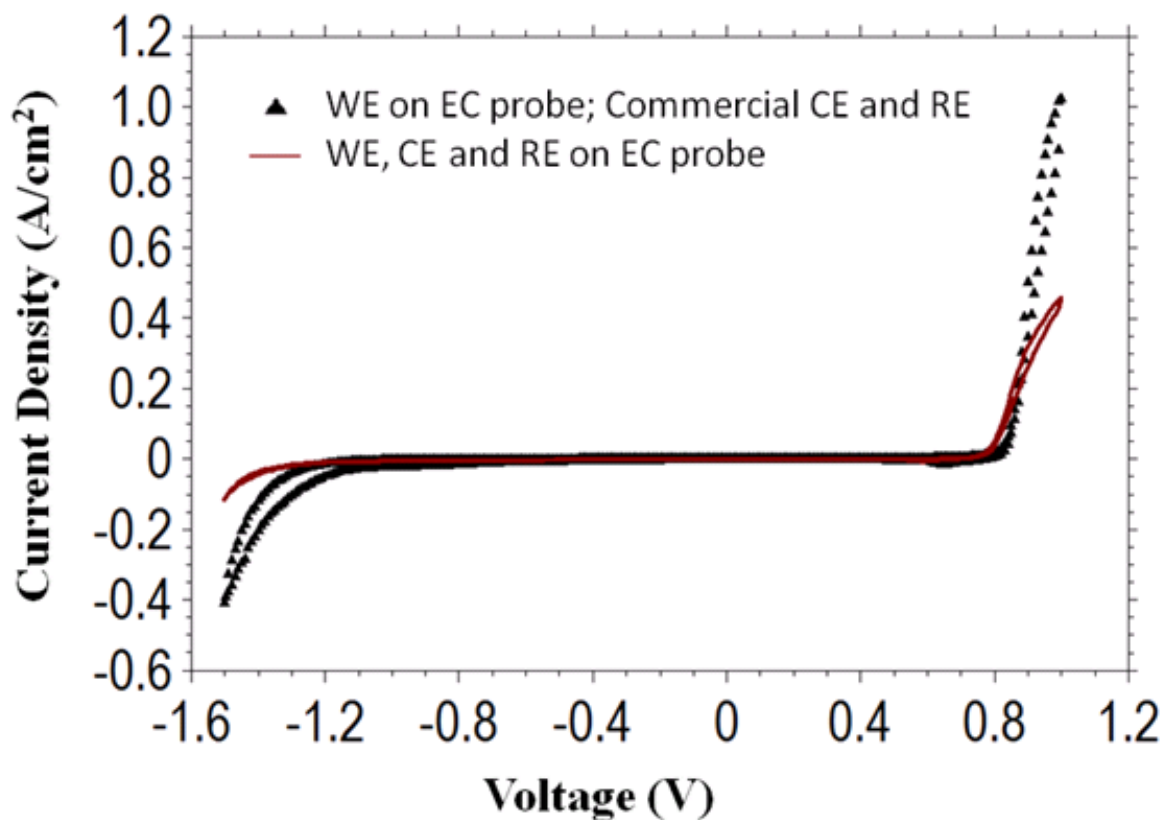


Figure 6-7. A comparison on the cyclic voltammograms in 1M KCl.

Shown in Figure 6-8 is the CVs of an EC probe on  $\text{Fe}(\text{CN})_6^{-3/4}$  (in 1M KCl) with different scan rate  $\nu$ . The diameter of the poly-C WE is 20  $\mu\text{m}$ . It can be extracted from the curves that the  $E_{1/2}$  is  $\sim 230$  mV, which confirms the diamond quality as discussed in the previous section. At scan rate of 0.05V/s, the shape of the curve is sigmoidal which a typical property of a microelectrode is. Its limiting current can be calculated by the following equation,

$$i_l = 4nFDCr \quad (24)$$

where  $n$  is the number of electrons involved in  $n$  electrode reaction ( $n=1$ ),  $F$  is the Faraday constant ( $F=95600$  C),  $D$  is the diffusion coefficient ( $D=6.5 \times 10^{-6}$   $\text{cm}^2 \text{s}^{-1}$ ),  $C$  is

the analyte concentration ( $C=1$  mM) and  $r$  is the radius of the electrode ( $r=10$   $\mu\text{m}$ ). The calculated  $i_l$  is 1.25 nA. This value matched with the measured value 1.1 nA ( $=1.6$  nA  $-$  0.5 nA), which is background subtracted. As the scan rate  $v$  increases, the shape of the curves becomes peak shape. It is because the time for the analytes to be diffused up to the electrode surface is shortened. There is not enough analyte for taking reaction. Therefore, peak shape is resulted.

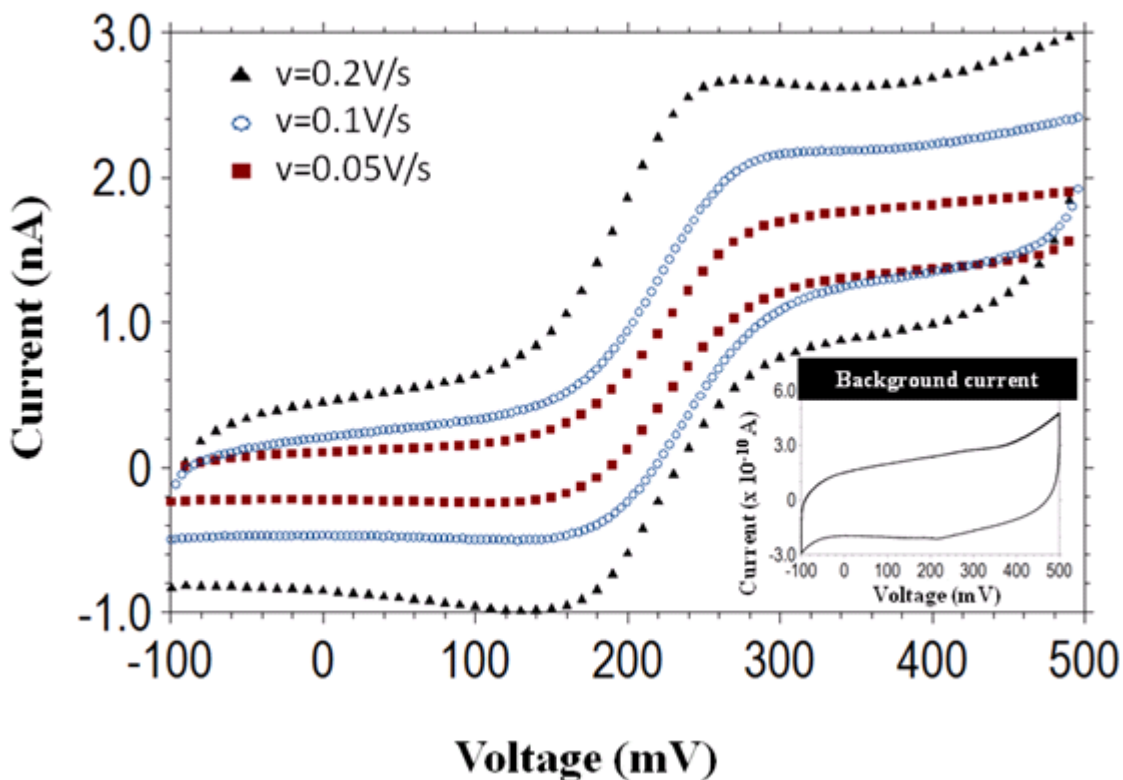


Figure 6-8. Cyclic voltammograms of the EC probe in 1mM  $\text{Fe}(\text{CN})_6^{3-/4}$  + 1M KCl.

## 6.3 Probe Applications

### 6.3.1 Electrical Detection

Poly-C EL probes are used for the first time to record *in vivo* neural activity by surgically inserting the probe into the auditory cortex area of a guinea pig brain as shown in Figure 6-9. The *in vivo* electrical detection was done in the Kresge Hearing Research Institute at the University of Michigan and performed on pigmented guinea pigs using approved animal use and care procedures. The poly-C probe was mounted on a probe connector which is precisely controlled by a sub-micron positioner. The poly-C probe was then placed in the auditory cortex of the guinea pig which is located in the right hemisphere of its brain. The probe was connected to a Plexon Neural Data Acquisition System to record the stimulated neural signals..

During the electrical data recording, a broadband sound signal (stimulus) was applied twice per second to stimulate the brain of the guinea pig. Each stimulus lasts for 200 ms. The all-diamond EL probe monitored the effect of the sound signal on the neural activity inside the cortex; an example of the recorded signal from one electrode of the EL probe is shown in Figure 6-10. The recorded electrical signal was amplified 20,000 times and filtered using a bandpass filter designed to pass frequencies in the 100 Hz - 10kHz range. It can be seen in Figure 6-10 (b) that the probe received a large signal of  $>25\mu\text{V}$  in response to the sound signal. It is demonstrated that the diamond probe received the stimulated neural signal at a signal to noise (S/N) ratio of  $\sim 2$ .

There are several possible reasons for the low S/N ratio. One of the possible reasons is that the probe position may not be close enough to the body of the firing

neurons. The strength of the neuron signal attenuates with increasing distance between the recording site and target neurons [151]. Increasing the SNR will be a priority in future work.

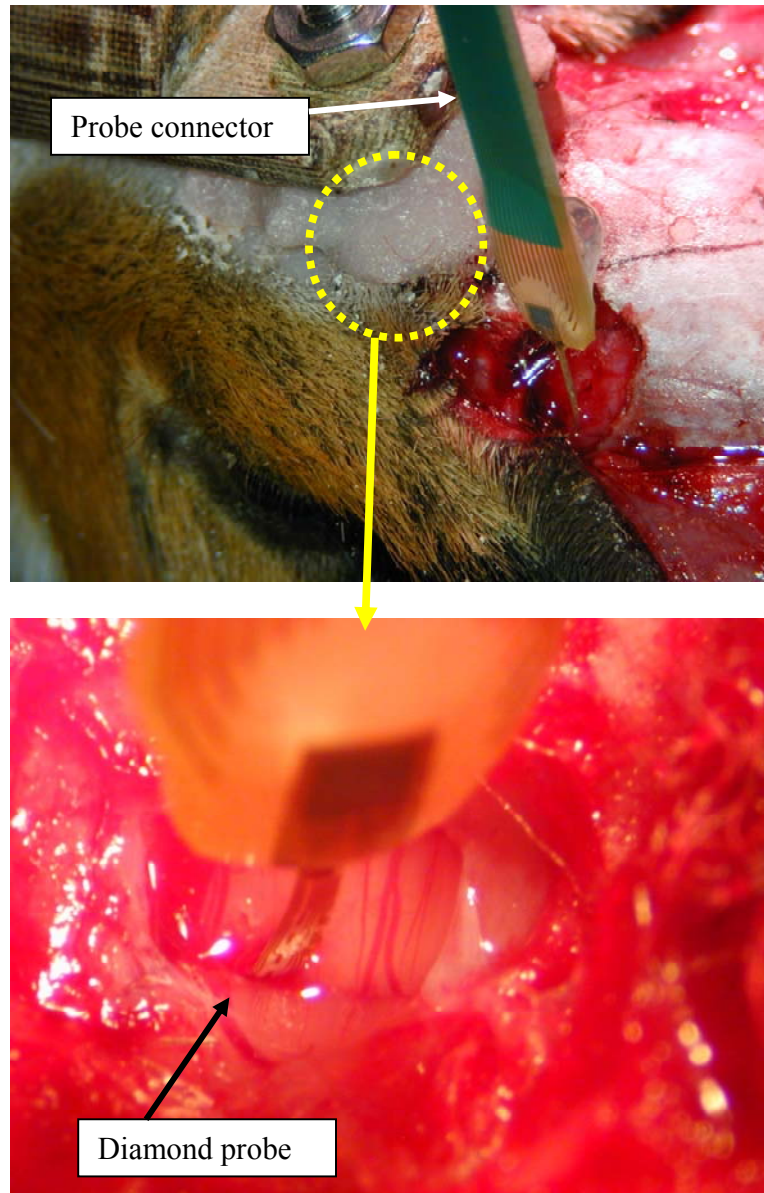


Figure 6-9. Acute recording of neural activity using the diamond probe.

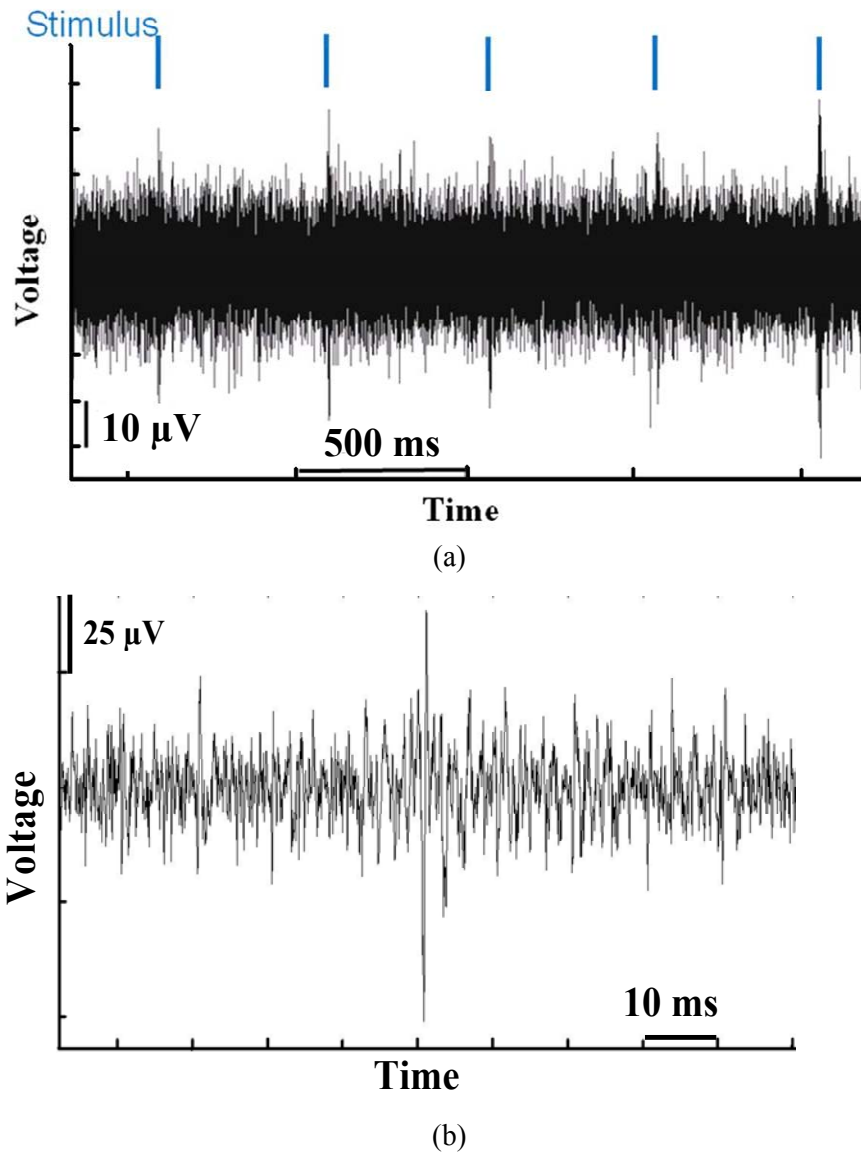


Figure 6-10. (a) Recorded neural activity in guinea pig's auditory cortex using the diamond probe with an electrode area of  $100\mu\text{m}^2$ , (b) A recorded neural spike.

Another recorded signal from an *in vivo* experiment using an all-diamond EL probe is shown in Figure 6-11. Again, the probe was placed in the auditory cortex of a guinea pig's brain. The signals recorded from each of the eight sites are shown along with

their corresponding positions on the probe.. It can be easily inferred from the signals that the most intense neural activity was taking place around sites 1, 2 and 3. The sites recorded a peak signal every half second which is consistent with the frequency of the stimulus signal. On the rest of the sites, it seems that there is no neural activity recorded or the induced signal amplitude is too low to be observed. Another way of representing the recorded signals is shown in Figure 6-12. This acts as further evidence that the probe can successfully record neural activities. These histograms, shown in the figure, represent the recorded signal which has amplitude larger than a preset threshold at a particular time interval called bin (=1 ms). In the plot, the onset of the stimulus always takes place at  $t=0$  and lasts for 200 ms. Therefore, the recorded signals beyond  $t = 200$  ms are noise from external sources or related to background brain activity. It is shown in the plots that site 1, 2, 3 and 4 were receiving neural activity caused by the stimulus. This is proven by the fact that most of the recorded neural signals were received just as the stimulus began. (i.e. higher counts/bin). Some signals were still recorded between the onset of the stimulus and 200 ms. The stimulus is still present at this time; it is seen that neural activity is more sensitive to the onset of a stimulus rather than its presence. Beyond 200 ms, little or no activity is recorded; these signals are considered noise. Sites 5, 6, 7 and 8 show little or no neural activity because the amplitude of all the recorded signals are around noise level.

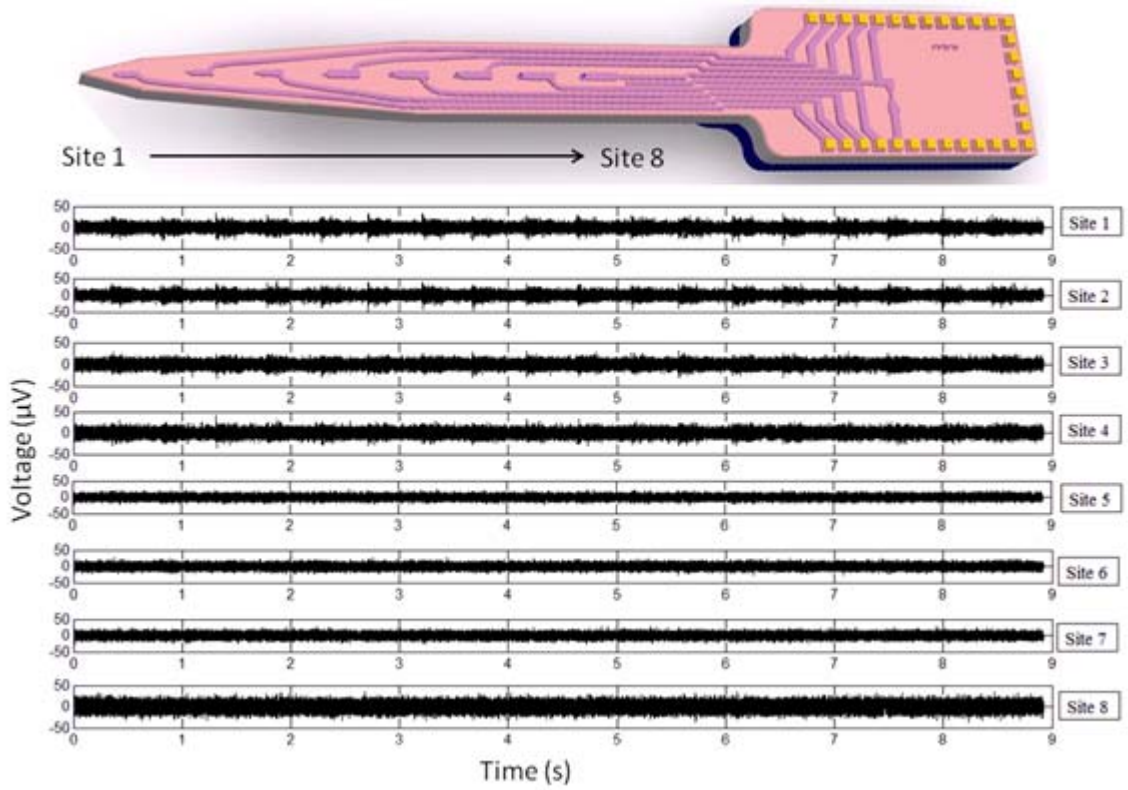


Figure 6-11. A recorded *in vivo* signal from an all-diamond EL probe.

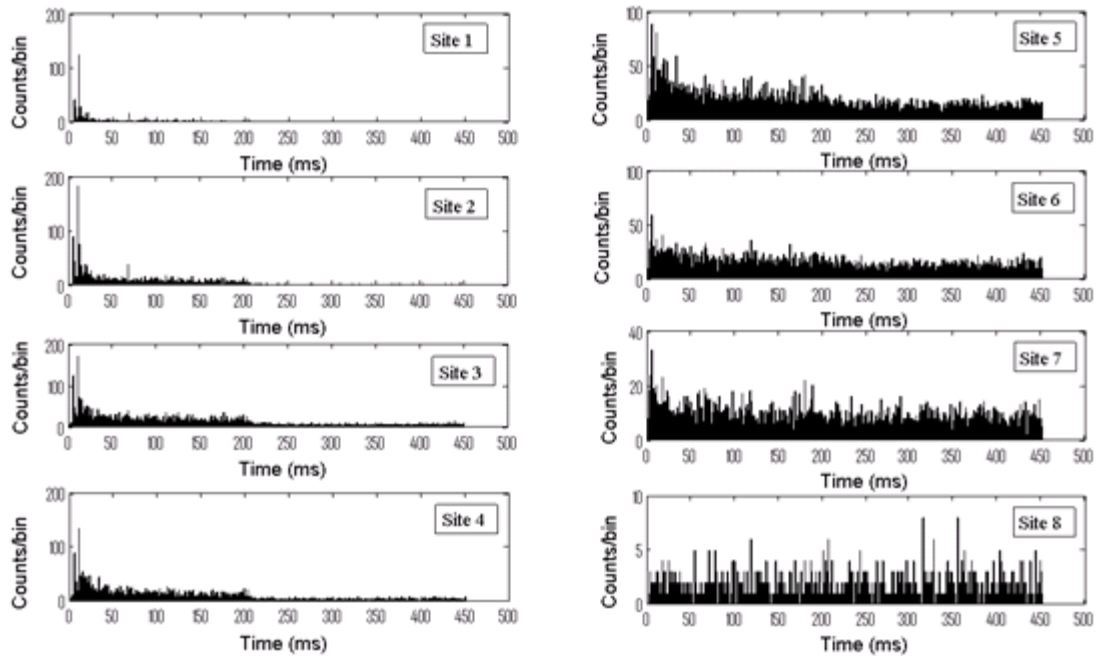
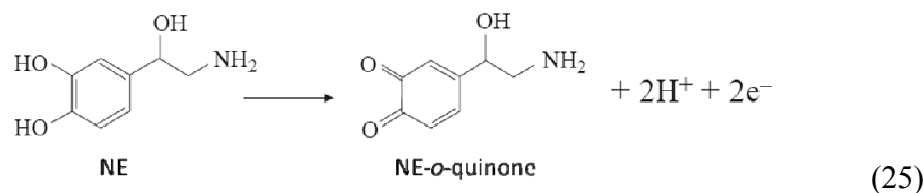


Figure 6-12. Histograms of the recorded neural signals shown in previous figure.

### 6.3.2 Electrochemical Detection

Norepinephrine (NE) is a neurotransmitter which can be found in the sympathetic nervous system and acts as a stress hormone. Norepinephrine, detected electrochemically according to the following  $2e^-/2H^+$  redox reaction, is oxidized to form NE-o-quinone.:



In a preliminary study focusing on the detection of NE in Krebs buffer solution, current density was recorded as a function of voltage applied to the poly-C electrode with respect to an Ag/AgCl reference electrode. The recorded data shown in Figure 6-13 are presented after subtracting the background current (as shown in the inset of Figure 6-13) as measured in Krebs buffer solution. The curves shown in Figure 6-13 are the currents recorded at different NE concentrations. The recorded current starts to increase when the applied voltage reached  $\sim 0.2$  V. The lowest detectable concentration of NE is roughly 10 nM. The results are similar to those reported in [36] for diamond coated electrodes but there is no peak observed in the recorded current using the poly-C electrode. One possible reason for this could be the variation in diamond quality which leads to a small heterogeneous rate constant  $k^0$  [27].

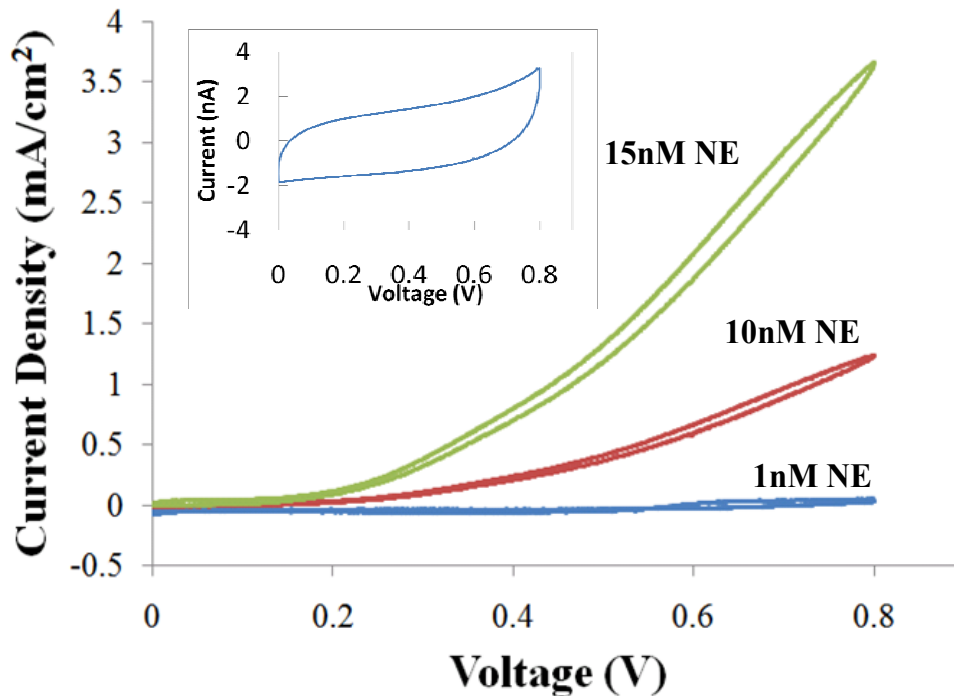


Figure 6-13. Measured cyclic voltammograms of the poly-C probe for different concentrations of NE in Krebs buffer solution using a scan rate of 100 mV/s. The inset shows the background current in Krebs solution.

In addition to NE detection, the detection of dopamine (DA), which is another important neurotransmitter, and is believed to be related to Parkinson's disease, is demonstrated. Shown in Figure 6-14 is a comparison of the detection of NE and DA with the same concentration. Clearly, there is a difference in the magnitude of the current density between the two neurotransmitters. However, it is difficult to identify  $E_{1/2}$  for the two curves as there is no clear plateau (i.e. limiting or saturated current). In fact, the reported  $E_{1/2}$  (vs. SCE) of DA and NE are 200 and 240 mV, respectively [152].

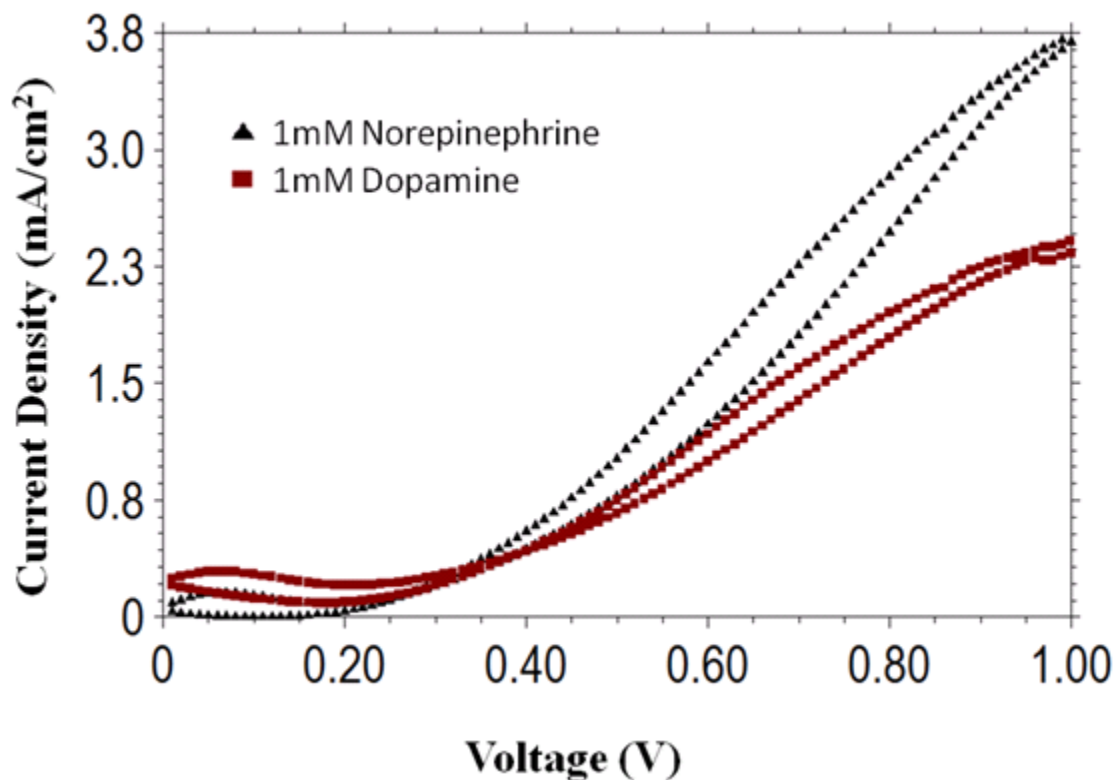


Figure 6-14. Detection of NE and DA with same concentration.

## 6.4 Summary

Poly-C probes are characterized using EIS and CV. It is found that the poly-C electrode acts similar to a capacitor and has a double layer capacitance of  $\sim 87 \mu\text{F}/\text{cm}^2$ . In addition, the poly-C electrode has the lowest background current (on the order of nA for a centimeter scale electrode) and a wider potential window (2.2V in total) as compared to Au, Pt and  $\text{IrO}_x$ . The EC probe is also characterized and shown to perform as well as commercial electrodes.

Poly-C probes are applied to *in vivo* electrical and *in vitro* electrochemical neural recording. The probes are successfully implanted in a guinea pig's brain and used to

recorded *in vivo* stimulated neural signal. It is also demonstrated that the poly-C probes are able to detect both NE and DA.

# Chapter 7

## Summary and Recommendations

### 7.1 Summary of Contributions

#### 1. Fundamental research on poly-C technology

Poly-C technologies used in this project, including seed nucleation, growth and patterning, have been studied and addressed. These poly-C technologies are developed specifically for later poly-C probe fabrication. Two issues, which are crucial in terms of the fabrication of poly-C probes, have been reported and discussed for the first time. They are unintentional SiO<sub>2</sub> or Si etching during poly-C growth and diamond etching. The corresponding solutions are discussed.

#### 2. Enabling technology development in poly-C probe fabrication

The integration of poly-C into neural probe technology has been successful. All-diamond probes, which use poly-C as the material for the probe shank, leads and electrodes, have been realized for the first time. With the development of the poly-C technologies in this study, two types of poly-C probes (i.e. EL and EC probes) are fabricated and reported for the first time. EL probes consist of a number of poly-C sites for electrical (physiological) detection. EC probes, on the other hand, consist of three different types of electrodes (i.e. RE, CE and WE) which are necessary for performing electrochemical detection.

### 3. Poly-C neural probe applications

Implementations of the poly-C probes in neuro-electrical and neuro-chemical recording have been studied. EL probes have been successfully implemented in a guinea pig's brain and acute electrical signals have been recorded *in vivo*. EC probes, on the other hand, have demonstrated the ability to detect neurotransmitters *in vitro*. This seminal and pioneer work on poly-C probes will provide a strong basis and guidance for future developments in poly-C neural probe technologies.

## 7.2 Future Research Areas

As for the long term development of the poly-C neural probe project, the following research areas must be addressed and discussed intensively in order to provide more promising performance of the poly-C neural probe.

1. Further improvements on the conductivity of undoped poly-C must be made. One possible way of accomplishing this is the introduction of oxygen during diamond growth. This may lead to having undoped poly-C packaging for the all-diamond probe.
2. Further study on the electrical and electrochemical properties of poly-C electrodes and the integration of carbon nanotubes with poly-C electrodes. With further development of the poly-C electrodes, it may be possible to have a poly-C electrode serve as a stimulating electrode.
3. Integration of ultra nanocrystalline diamond (UNCD) into the probe fabrication. This can provide a smoother surface that is easily built upon.

4. Improvement on the design of the EL and EC probes, for instance, minimization of the probe size, optimization of the layout of the three electrode sets on the EC probes and the integration of channels in the probes.
5. Further study of the chronic implantation of the poly-C probes. Investigation of the long term performance of the poly-C probes *in vivo*.
6. System integration of the poly-C probes with a microcontroller chip for signal recording, processing and transmission.
7. Exploration of the possible applications of poly-C probes. For instance, surface modification of poly-C electrodes for biosensing applications.

## APPENDIX

### A. Process Flow of the Fabrication of Diamond Probes

| <b>S</b><br><b>t</b><br><b>e</b><br><b>p</b> | <b>Process</b>           | <b>Operation</b>     | <b>M</b><br><b>a</b><br><b>s</b><br><b>k</b> | <b>Descript-</b><br><b>ion</b> | <b>Equipment</b> | <b>Parameters</b>  | <b>In-line</b><br><b>Measure-</b><br><b>ment</b> |
|--|--------------------------|----------------------|--|--------------------------------|------------------|--|--|
| 1  | Pattern probe<br>backend | Pre-furnace<br>clean |  |                                |                  |  |  |
| 2  |                          | Grow oxide           |  |                                | B2 tube          | Recipe:<br>DWD/TCA<br><br>Parameter<br>table:<br>DWDSKIN<br><br>4 h, 1000 °C | Oxide thickness<br>~1.2µm                        |
| 3  |                          | Spin 1813            |  | 1.4µm                          | Spinner          | 4000 rpm, 30<br>sec  |  |
| 4  |                          | Soft bake            |  | 95 °C                          | Hotplate         | 1 min  |  |
| 5  |                          | Expose               | B<br>D<br>F                                  | Define<br>backend              | MA6              | 5 sec  |  |
| 6  |                          | Develop              |  |                                | MIF 318          | 1 min  |  |
| 7  |                          | Oxide etch           |  |                                | BHF              | 17 mins (until<br>patterned areas<br>are<br>hydrophilic)                     |  |
| 8  |                          | Pre-furnace<br>clean |  |                                |                  |  |  |

|    |                        |                                |  |  |                           |  |         |
|----|------------------------|--------------------------------|--|--|---------------------------|--|---------|
| 9  |                        | Deep boron diffusion           |  | Define backend                         | A2 tube                   | Recipe: BEDEP99<br>Parameter table: BORON99<br>5 h, 1175°C   |         |
| 10 |                        | Drive-in                       |  |  | A4 tube                   | Recipe: N2ANL/OX<br>Parameter table: N2ANL/OX<br>5 h, 1175°C |         |
| 11 |                        | Strip deep boron masking oxide |  |  | HF:H <sub>2</sub> O (1:1) | 7mins  |         |
| 12 |                        | Pre-furnace clean              |  |  |                           |  |         |
| 13 | Dielectric deposition  | LPCVD oxide                    |  | Dielectric deposition                  | D4 tube                   | Recipe: HTO<br>3 h 17mins,<br>450°C                          | ~1.2 μm |
| 14 |                        | HF-dip                         |  | Refresh LPCVD oxide surface            | HF:H <sub>2</sub> O (1:7) | 5 sec  |         |
| 15 | Undoped diamond growth | Nucleation                     |  | Diamond powder loaded water (DW, 0.5%) | Spinner                   | 500rpm for 5 sec, 2000rpm for 30 sec                         |         |
| 16 |                        | Diamond growth                 |  |  | MPCVD                     | 20h, 750°C   | ~3 μm   |
| 17 | Dielectric deposition  | PECVD oxide                    |  |  | PECVD                     | 3 times (1 μm @deposition)                                   |         |
| 18 |                        | Annealing                      |  | 650°C                                  | RTP                       | 10 mins  |         |

|      |                             |                          |             |                                       |                           |                                      |   |  |
|------|-----------------------------|--------------------------|-------------|---------------------------------------|---------------------------|--------------------------------------|---|--|
| 19   |                             | Annealing                |             | 750°C                                 | RTP                       | 10 mins                              |   |  |
| 20   |                             | Annealing                |             | 970°C                                 | RTP                       | 3 mins                               |   |  |
| 21   | Doped diamond growth        | HF-dip                   |             | Refresh PECVD oxide                   | HF:H <sub>2</sub> O (1:7) | 5 sec                                |   |  |
| 22   |                             | Nucleation               |             | DW, 3.75%                             | Spinner                   | 500rpm for 5 sec, 2000rpm for 30 sec |   |  |
| 23   |                             | Diamond growth           |             |                                       | MPCVD                     | 13h, 750°C, TMB (2%)                 | ~1 μm   |  |
| 23 a |                             | Diamond etch             |             |                                       | PT790                     | 10mins                               |   |  |
| 24   | Pattern doped diamond layer | Spin 1827                |             | 3 μm                                  | Spinner                   | 3000rpm, 30 sec                      |   |  |
| 25   |                             | Soft bake                |             | 95 °C                                 | Hotplate                  | 1 min                                |   |  |
| 26   |                             | Expose                   | B<br>D<br>P | Define doped diamond electrode window |                           | MA6                                  | 17 sec  |  |
| 27   |                             | Develop                  |             |                                       |                           | MIF 318                              | 1 min   |  |
| 28   |                             | Masking layer deposition |             | Al (1 μm)                             |                           | Enerjet Evaporator                   |   |  |
| 29   |                             | Lift-off                 |             |                                       |                           | Acetone                              | 1 h   |  |
| 30   |                             | RIE                      |             |                                       |                           | Plasma-Therm 790                     | Recipe: CAO_NEW (mainly O <sub>2</sub> etch)<br>2 h |  |
| 31   |                             | HF-dip                   |             | Removing diamond whiskers             |                           | HF:H <sub>2</sub> O (1:7)            | 10 sec  |  |
| 32   |                             | Al removal               |             |                                       |                           | Al etchant                           |   |  |

|    |                                      |                          |             |                        |                    |                                    |   |
|----|--------------------------------------|--------------------------|-------------|------------------------|--------------------|------------------------------------|---|
| 33 | Etch backside oxide                  | Spin 9260                |             | 6 $\mu\text{m}$        | Spinner            | 4000rpm, 30 sec                    |   |
| 34 |                                      | Etch                     |             |                        | BHF                | 15mins (until hydrophobic surface) |   |
| 35 |                                      | PR remove                |             |                        | Acetone            |                                    |   |
| 36 | Pattern undoped diamond              | Masking layer deposition |             | Al (1 $\mu\text{m}$ )  | Enerjet Evaporator |                                    |   |
| 37 |                                      | Spin 5214                |             | 1.6 $\mu\text{m}$      | Spinner            | 3000rpm, 30 sec                    |   |
| 38 |                                      | Soft bake                |             | 95 $^{\circ}\text{C}$  | Hotplate           | 1 min                              |   |
| 39 |                                      | Expose                   | U<br>D<br>P |                        | MA6                | 4 sec                              |   |
| 40 |                                      | Hard bake                |             | 115 $^{\circ}\text{C}$ | Hotplate           | 1:30 mins                          |   |
| 41 |                                      | Flood Expose             |             |                        | MA6                | 1 min                              |   |
| 42 |                                      | Develop                  |             |                        | AZ300              | 40 sec                             |   |
| 44 |                                      | Mask etch                |             |                        | Al etchant Type A  |                                    |   |
| 45 |                                      | Diamond etch             |             |                        | Plasma-Therm 790   | Recipe: diamond (with F), 3 h      | It also etches the LPCVD oxide underneath. Check and etch until the expose surface is conducting. |
| 46 |                                      | Al removal               |             |                        | Al etchant         |                                    |   |
| 47 | Dielectric deposition and patterning | PECVD deposition         |             | 1 $\mu\text{m}$        | PECVD              | 500nm @                            |   |
| 48 |                                      | Spin 9260                |             | 6 $\mu\text{m}$        | Spinner            | 4000rpm, 30 sec                    |   |
| 49 |                                      | Soft bake                |             | 95 $^{\circ}\text{C}$  | Hotplate           | 2 ½ min                            |   |

|    |  |                 |             |                             |                                  |  |                                       |
|----|--|-----------------|-------------|-----------------------------|----------------------------------|--|---------------------------------------|
| 50 |  | Expose          | B<br>D<br>P | doped<br>diamond<br>pattern | MA6                              | 35 sec                                     |                                       |
| 51 |  | Develop         |             |                             | AZ400: H <sub>2</sub> O<br>(4:1) | 2 min                                      |                                       |
| 52 |  | RIE             |             |                             | Plasma-Therm<br>790              | Recipe:<br>n_SiO <sub>2</sub> , 50<br>mins | P.S. if 65mins<br>for 1.2 μm<br>PECVD |
| 53 |  | PR remove       |             |                             | Acteone                          |  |                                       |
| 54 |  | Ashing          |             |                             | March asher                      | 100W, 100 sec                              |                                       |
| 55 |  | Spin 5214       |             | 1.6 μm                      | Spinner                          | 3000rpm, 30<br>sec                         |                                       |
| 56 |  | Soft bake       |             | 95 °C                       | Hotplate                         | 1 min                                      |                                       |
| 57 |  | Expose          | U<br>D<br>P |                             | MA6                              | 4 sec                                      |                                       |
| 58 |  | Hard bake       |             | 115 °C                      | Hotplate                         | 1:30 mins                                  |                                       |
| 59 |  | Flood<br>Expose |             |                             | MA6                              | 1 min                                      |                                       |
| 60 |  | Develop         |             |                             | AZ300                            | 40 sec                                     |                                       |
| 61 |  | RIE             |             |                             | Plasma-Therm<br>790              | Recipe:<br>n_SiO <sub>2</sub> , 25<br>mins |                                       |
| 62 |  | PR remove       |             |                             | Acteone                          |  |                                       |
| 63 |  | Ashing          |             |                             | March asher                      | 100W, 100 sec                              |                                       |
| 64 |  | Spin 5214       |             | 1.6 μm                      | Spinner                          | 3000rpm, 30<br>sec                         |                                       |
| 65 |  | Soft bake       |             | 95 °C                       | Hotplate                         | 1 min                                      |                                       |
| 66 |  | Expose          | U<br>D<br>P |                             | MA6                              | 4 sec                                      |                                       |
| 67 |  | Hard bake       |             | 115 °C                      | Hotplate                         | 1:30 mins                                  |                                       |

|    |                             |                  |             |                                |                               |                                      |  |
|----|-----------------------------|------------------|-------------|--------------------------------|-------------------------------|--------------------------------------|--|
| 68 |                             | Flood Expose     |             |                                | MA6                           | 1 min                                |  |
| 69 |                             | Develop          |             |                                | AZ300                         | 40 sec                               |  |
| 70 |                             | RIE              |             |                                | Plasma-Therm 790              | Recipe: n_SiO <sub>2</sub> , 25 mins |  |
| 71 |                             | PR remove        |             |                                | Acetone                       |                                      |  |
| 72 |                             | Ashing           |             |                                | March asher                   | 100W, 100 sec                        |  |
| 73 | Pattern counter electrode   | Spin 9260        |             | 6 μm                           | Spinner                       | 4000rpm, 30 sec                      |  |
| 74 |                             | Soft bake        |             | 95 °C                          | Hotplate                      | 2 ½ min                              |  |
| 75 |                             | Expose           | C<br>E<br>P | Counter electrode              | MA6                           | 35 sec                               |  |
| 76 |                             | Develop          |             |                                | AZ400: H <sub>2</sub> O (4:1) | 2 min                                |  |
| 77 |                             | Metal deposition |             | Ti/Au (50 nm/ 400 nm)          | SJ20                          |                                      |  |
| 78 |                             | Lift-off         |             |                                | Acetone                       | 2 h                                  |  |
| 79 | Pattern reference electrode | Spin 9260        |             | 6 μm                           | Spinner                       | 4000rpm, 30 sec                      |  |
| 80 |                             | Soft bake        |             | 95 °C                          | Hotplate                      | 2 ½ min                              |  |
| 81 |                             | Expose           | R<br>E<br>P | Reference electrode            | MA6                           | 35 sec                               |  |
| 82 |                             | Develop          |             |                                | AZ400: H <sub>2</sub> O (4:1) | 2 min                                |  |
| 83 |                             | Metal deposition |             | Ti/Au/Ag (10 nm/ 8 nm/ 400 nm) | Enerjet Sputter               |                                      |  |
| 84 |                             | Lift-off         |             |                                | Acetone                       | Overnight                            |  |

|     |                            |                  |             |                             |                               |                                      |  |
|-----|----------------------------|------------------|-------------|-----------------------------|-------------------------------|--------------------------------------|--|
| 85  | Pattern metal interconnect | Spin 9260        |             | 6 $\mu\text{m}$             | Spinner                       | 4000rpm, 30 sec                      |  |
| 86  |                            | Soft bake        |             | 95 °C                       | Hotplate                      | 2 ½ min                              |  |
| 87  |                            | Expose           | I<br>P      | Lead pattern                | MA6                           | 35 sec                               |  |
| 88  |                            | Develop          |             |                             | AZ400: H <sub>2</sub> O (4:1) | 2 min                                |  |
| 89  |                            | Metal deposition |             | Ti/Au<br>(50 nm/<br>400 nm) | SJ20                          |                                      |  |
| 90  |                            | Lift-off         |             |                             | Acetone                       |                                      |  |
| 91  | Top oxide insulator        | PECVD deposition |             | 2 $\mu\text{m}$             | PECVD                         | 500nm @                              |  |
| 92  |                            | Spin 9260        |             | 6 $\mu\text{m}$             | Spinner                       | 4000rpm, 30 sec                      |  |
| 93  |                            | Soft bake        |             | 95 °C                       | Hotplate                      | 2 ½ min                              |  |
| 94  |                            | Expose           | T<br>I<br>P | Oxide insulator             | MA6                           | 35 sec                               |  |
| 95  |                            | Develop          |             |                             | AZ400: H <sub>2</sub> O (4:1) | 2 min                                |  |
| 96  |                            | RIE              |             |                             | Plasma-Therm 790              | Recipe: n_SiO <sub>2</sub> , 90 mins |  |
| 97  |                            | PR remove        |             |                             | Acetone                       |                                      |  |
| 98  |                            | Ashing           |             |                             | March asher                   | 100W, 100 sec                        |  |
| 99  | Probe release              | Wafer thinning   |             |                             | HF-Nitric                     | 30 mins                              |  |
| 100 |                            | Release          |             | 115 °C                      | EDP                           | 4 h                                  |  |

## B. Activation of Ir

- 1) Put 1 pack of P-5368 Phosphate Buffered Saline pH7.4 in 25mL of DI water. The solution is ~0.3M.
- 2) Use “amperometric i-t curve” to set the -3.0V for 5 mins.
- 3) Clean the bubbles on the surface of Ir
- 4) Use “amperometric i-t curve” to set the 2.5V for 5 mins.
- 5) Use “CV” to scan though -0.6 to 0.72 vs. Ag/AgCl. With 100mV/s for 100 cycles (=200 segments)
- 6) Use “Chronocoulometry” to set pulse width = 1sec, initE= -0.8 and finalE=0.7.

# BIBLIOGRAPHY

- [1] David Eagleman, "10 unsolved mysteries of the brain", *Discover*, August 2007.
- [2] N. B. Standen, P. T. A. Gray, and M. J. Whittaker, Microelectrode techniques, *The Plymouth workshop handbook*, Cambridge, 1987.
- [3] K. D. Wise, J. B. Angell and A. Starr, "An integrated-circuit approach to extracellular microelectrodes", *IEEE Trans. Biomed. Eng.*, v. 17, no. 3, pp. 238-247, 1970.
- [4] P. Norlin, M. Kindlundh, A. Mouroux, K. Yoshida and U. G. Hofmann, "A 32-site neural recording probe fabricated by DRIE of SOI substrates," *J. of Micromech. & Microeng.*, pp. 414-419, 2002.
- [5] D. R. Kipke, "Implantable neural probe systems for cortical neuroprosthesis", *Proc. of Int. Conf. of the IEEE Eng. in Med. and Bio. Soc.*, pp. 5344-5347, 2004.
- [6] Q. Bai and K. D. Wise, "Single-unit neural recording with active microelectrode arrays", *IEEE Trans. Biomed. Eng.*, v. 48, pp. 911-920, 2001.
- [7] C. Pang, J. G. Cham, Z. Nenadic, S. Musallam, Y. C. Tai, J. W. Burdick and R. A. Andersen, "A new multi-site probe array with monolithically integrated parylene flexible cable for neural prostheses," *Proc. of Int. Conf. of the IEEE Eng. in Med. and Bio. Soc.*, pp. 7114- 7117, 2005.
- [8] J. Chen and K. D. Wise, "A multichannel neural probe for selective chemical delivery at the cellular level", *IEEE Trans. Biomed Eng.*, v. 44, no. 8, pp. 760-769, 1997.
- [9] L. Lin and A. Pisano, "Silicon processed microneedles", *IEEE J. Micromech. Syst.*, v. 8, no. 1, pp. 78-84, 1999.
- [10] J. Wang, M. Gulari, P. T. Bhatti, B. Y. Arcand, K. Beach, C. R. Fredrich and K. D. Wise,, "A cochlear electrode array with built-in position sensing," *Proc. of Int. Conf. on MEMS*, pp. 786-789, 2005.
- [11] Y. Tang, D. M. Aslam, J. Wang and K. D. Wise, "Poly-Crystalline Diamond Piezoresistive Position Sensors for Cochlear Implant Probe", *Proc. of Solid-State Sensors, Actuators and Microsystems*, v.1, pp. 542-546, 2005.
- [12] Y. Yao, M. N. Gulari, J. A. Wiler and K. D. Wise, "A microassembled low-profile three-dimensional microelectrode array for neural prosthesis applications", *J. of Micro. Mech. Syst.*, v. 16, no. 4, pp. 977-988, 2007.
- [13] C. Pang, J. G. Cham, Z. Nenadic, Y. C. Tai, J. W. Burdick and R. A. Andersen, "A New Neural Recording Electrode Array with Parylene Insulating Layer", *Proc. of Int. Conf. on Miniaturized Syst. for Chemistry and Life Sciences*, pp. 675-677, 2005.
- [14] E. Patrick, M. Ordonez, N. Alba, J. C. Sanchez and T. Nishida, "Design and fabrication of a flexible substrate microelectrode array for brain machine interfaces", *Proc. of IEEE EMBS*, pp. 2966-2969, 2006.
- [15] Y. Kato, M. Nishino, I. Saito, T. Suzuki and K. Mabuchi, "Flexible intracortical neural probe with biodegradable polymer for delivering bioactive components", *Proc. of IEEE EMBS*, pp. 143-146, 2006.
- [16] S. Takeuchi, T. Suzuki, K. Mabuchi and H. Fujita, "3D flexible multichannel neural probe array", *J. Micomech. Microeng.*, v. 14, pp. 104-107, 2004.

- [17] H. Lu, S. H. Cho, J. B. Lee, L. Cauller, M. R. Ortega and G. Hughes, "SU8-based micro neural probe for enhanced chronic in-vivo recording of spike signals from regenerated axons", *IEEE Int. Conf. on Sensors*, pp. 66-69, 2006.
- [18] M. D. Johnson, R. K. Franklin, K. A. Scott, R. B. Brown and D. R. Kipke, "Neural probes for concurrent detection of neurochemical and electrophysiological signals in vivo", *Proc. of IEEE EMBS*, pp. 7325-7328, 2005.
- [19] K. L. Drake, K. D. Wise, J. Farraye, D. J. Anderson and S. P. Bement, "Performance of planar multisite microprobes in recording extracellular single-unit intracortical activity", *IEEE Trans. on Bio.Eng.*, v. 35, no. 9, pp. 719-732, 1988.
- [20] T. L. Rose, E. M. Kelliher and L. S. Robbless, "Assessment of capacitor electrodes: preliminary evaluation," *J. of Neurosci. Methods*, no. 12, pp. 181-193, 1985
- [21] D. J. Anderson, K. Najafi, S. J. Tanghe, D. A. Evans, K. L. Levy, J. F. Hetke, X. Xue, J. J. Zappia and K. D. Wise, "Batch-fabricated thin-film electrodes for stimulation of the central auditory system", *IEEE Trans. of Bio. Eng.*, v. 36, no. 7, 1989.
- [22] M. P. Hughes, K. Bustamante, D. J. Banks and D. J. Ewims, "Effects of electrode size on the performance of neural recording microelectrodes", *IEEE Conf. on Microtech. in Med. And Bio.*, pp. 220-223, 2000.
- [23] J. A. Stamford, P. P alij, C. Davidson, C. M. Jorm and J. Millar, "Simultaneous "real time" electrochemical and electrophysiological recording in brain slices with a single carbon-fibre microelectrode", *J. of Neuroscience Methods*, v. 50, pp. 279-290, 1993.
- [24] L. S. Pan, D. R. Kania, *Diamond: Electronic Properties and Applications*, Springer, 1994.
- [25] M. Hupert, A. Muck, J. Wang, J. Stotter, Z. Cvackova, S. Haymond, Y. Show and G. M. Swain, "Conductive diamond thin-films in electrochemistry," *Dia. and Rel. Mat.*, v. 12, pp. 1940-1949, 2003.
- [26] A.N. Ndao, F. Zenia, A. Deneuille, M. Bernard, C. L. le' ment, "Effect of boron concentration on the electrochemical reduction of nitrates on polycrystalline diamond electrodes", *Dia. and Rel. Mat.*, v. 9, pp. 1175-1180, 2000.
- [27] A. Bennett, J. Wang, Y. Show and G. M. Swain, "Effect of sp<sup>2</sup>-bonded nondiamond carbon impurity on the response of boron-doped polycrystalline diamond thin-film electrodes", *J. of Electrochem. Soc.*, v. 151, no. 9, pp. 306-313, 2004.
- [28] C. E. Nebel, H. Kato, B. Rezek, D. Shin, D. Takeuchi, H. Watanabe and T. Yamamoto, "Electrochemical properties of undoped hydrogen terminated CVD diamond", *Dia. and Rel. Mat.*, v. 15, pp. 264-268, 2006.
- [29] G. M. Swain and R. Ramesham, "The electrochemical activity of boron-doped polycrystalline diamond thin film electrode", *Anal. Chem.*, v. 65, pp. 345-351, 1993.
- [30] L. Tang, C. Tsai, W. W. Gerberich, L. Kruckeberg and D. R. Kania, "Biocompatibility of chemical-vapour-deposited diamond", *Biomaterials*, v. 16, pp. 483-488, 1995.
- [31] R. A Freitas, *Nanomedicine, Vol. IIA: Biocompatibility*, Landes Bioscience, 2003

- [32] E. W. Salzman, J. Linden, G. McManama and J. A. Ware, "Role of fibrinogen in activation of platelets by artificial surfaces," *Annals N. Y. Acad. Sci.*, v. 516, pp. 184-195, 1987
- [33] A. Kraft, "Doped diamond: A Compact Review on a new, versatile, electro material", *Int. J. Electrochem. Sci.*, v. 2, pp. 355-385, 2007.
- [34] J. Cvacka, V. Quaiserova, J. W. Park, Y. Show, A. Muck and G. M. Swain, "Boron-doped Diamond Microelectrodes for Use in Capillary Electrophoresis with Electrochemical Detection", *Anal. Chem.*, v.75, pp. 2678-2687, 2005.
- [35] J. M. Halpern, S. Xie, G. P. Sutton, B. T. Higashikubo, C. A. Chestek, H. Liu H. J. Chiel, and H. B. Martin, "Diamond electrodes for neurodynamic studies in *Aplysia californica*", *Dia. and Rel. Mat.*, v. 15, pp. 183-187, 2006.
- [36] J. Park, V. Q. Mocko, K. Peckova, J. J. Galligan, G. D. Fink and G. M. Swain, "Fabrication, characterization, and application of a diamond microelectrode for electrochemical measurement of norepinephrine release from the sympathetic nervous system", *Dia. and Rel. Mat.*, v. 15, pp. 761-772, 2006.
- [37] P. T. Bhatti, B. Y. Arcand, J. Wang, N. V. Butala, C. R. Friedrich and K. D. Wise, "A high-density electrode array for cochlear prosthesis", *Proc. of Int. Conf. on Solid State Sensors, Actuators and Microsystems*, pp. 1750-1753, 2003.
- [38] P. Norlin, M. Kindlundh, A. Mouroux, K. Yoshida, W. Jensen, U. G. Hofmann, "A 32-site neural recording probe fabricated by double-sided deep reactive ion etching of silicon-on-insulator substrates", *Proc. of the Micromechanics Europe Workshop*, 2001.
- [39] J. Wang, M. Gulari, P. T. Bhatti, B. Y. Arcand, K. Beach, C. R. Friedrich and K. D. Wise, "A cochlear electrode array with built-in position sensing," *Proc. of Int. Conf. on Micro Electro Mechanical Systems*, pp. 786-789, 2005.
- [40] Y. Tang, D. M. Aslam, J. Wang and K. D. Wise, "Poly-Crystalline Diamond Piezoresistive Position Sensors for Cochlear Implant Probe", *Proc. of Solid-State Sensors, Actuators and Microsystems*, v.1, pp. 542-546, 2005
- [41] C. Pang, J. G. Cham, Z. Nenadic, S. Musallam, Y. C. Tai, J. W. Burdick and R. A. Andersen, "A new multi-site probe array with monolithically integrated parylene flexible cable for neural prostheses," *Proc. of Int. Conf. of the IEEE Eng. in Med. and Bio. Soc.*, pp. 7114- 7117, 2005.
- [42] S. Takeuchi, T. Suzuki, K. Mabuchi and H. Fujita, "3D flexible multichannel neural probe array," *J. of Micromech. and Microeng.*, v.14, pp. 104-107, 2004.
- [43] D. R. Kipke, "Implantable neural probe systems for cortical neuroprosthesis," *Proc. of Int. Conf. of the IEEE Eng. in Med. and Bio. Soc.*, 5344-5347, 2004.
- [44] Q. Bai and K. D. Wise, "Single-unit neural recording with active microelectrode arrays," *IEEE Trans Biomed. Eng.*, v. 48, pp. 911-20, 2001.
- [45] P. Norlin, M. Kindlundh, A. Mouroux, K. Yoshida, W. Jensen, U. G. Hofmann, "A 32-site neural recording probe fabricated by double-sided deep reactive ion etching of silicon-on-insulator substrates," *Proc. of the Micromechanics Europe Workshop*, 2001.
- [46] P. K. Campbell, K. E. Jones, R. J. Huber, K. W. Horch and R. A. Normann, "A silicon-based three-dimensional neural interface: manufacturing process for an intracortical electrode array," *IEEE Trans. Biomed. Eng.*, v. 38, no. 8, pp.758-768, 1991.

- [47] M. K. Kindlundh, P. Norlin, U. G. Hofmann, "A neural probe process enabling variable electrode configurations," *Sensors and Actuators B: Chemical*, v. 102, pp. 51-58, 2004.
- [48] T. H. Yoon, E. J. Hwang, D. Y. Shin, S. J. Parl, S. J. Oh, S. C. Jung, H. C. Shin and S. J. Kim, "A micromachined silicon depth probe for multichannel neural recording," *IEEE Trans. Biomed. Eng.*, v. 47, no. 8, pp. 1082-1087, 2000.
- [49] W. L. C. Rutten, H. J. vanWier and J. H. M. Put, "Sensitivity and selectivity of intraneural stimulation using a silicon electrode array," *IEEE Trans. Biomed. Eng.*, v. 38, no. 2, pp.192-198, 1991.
- [50] D. T. Kewley, M. D. Hills, D. A. Borkholder, I. E. Opris, N. I. Maluf, C. W. Stormont and G. T. A. Kovacs "Plasma-etched neural probes," *Sens. Actuators A*, v. 58, pp. 27-35, 1997.
- [51] K. Chueng, L. Gun, K. Djupsund, D. Yang and L. P. Lee, "A new neural probe using SOI wafers with topological interlocking mechanism," *Proc. of IEEE Int. Conf. on Microtechnologies in Medicine & Biology*, pp. 507-511, 2000.
- [52] P. S. Motta and J. W. Judy, "Multielectrode microprobes for deep-brain stimulation fabricated with a customizable 3-D electroplating process," *IEEE Trans. On Biomed. Eng.*, v. 52, no. 5, 2005
- [53] J. Wu, L. Yan, W. C. Tang and F. G. Zeng, "Micromachined electrode arrays with form-fitting profile for auditory nerve prostheses," *Proc. of IEEE Eng. in Medicine and Biology*, 2005.
- [54] K. D. Wise, A. M. Sodagar, Y. Yao, M. N. Gulari, G. E. Perlin and K. Najafi, "Microelectrode, microelectronics, and implantable neural microsystems", *Proc. of the IEEE*, v. 96, no. 7, pp. 1184-1202, 2008
- [55] P. S. Motta and J. W. Judy, "Multielectrode microprobes for deep-brain stimulation fabricated with a customizable 3-D electroplating process," *IEEE Trans. on Biomed. Eng.*, v. 52, no. 5, 2005www.plexoninc.com
- [56] G. T. A. Kovacs, C. W. Stormont and J. M. Rosen, "Regeneration microelectrode array for peripheral nerve recording and stimulation," *IEEE Trans. on Biomed.Eng.*, v. 39, no. 9, pp. 893-902, 1992.
- [57] M. D. Johnson, R. K. Franklin, K. A. Scott, R. B. Brown, D. R. Kipke, "Neural probes for concurrent detection of neurochemical and electrophysiological signals in vivo", *Prof. of IEEE Eng. In Med. And Bio*, pp. 7325-7328, 2005
- [58] R. K. Franklin, M. D. Johnson, K. A. Scott, J. H. Shim, H. Nam, D. R. Kipke and R.B. Brown, "Iridium oxide reference electrodes for neurochemical sensing with MEMS microelectrode arrays", *IEEE Sensors*, pp. 1400-1403, 2005.
- [59] H. Lu, S. H. Cho, J. B. Lee, L. Cauller, M. R. Ortega and G. Hughes, "SU8-based micro neural probe for enhanced chronic in-vivo recording of spike signals from regenerated axons", *Proc. of IEEE SENSORS*, pp. 65-69, 2006.
- [60] Y. Kato, M. Nishino, I. Saito, T. Suzuki and K. Mabuchi, "Flexible intracortical neural probe with biodegradable polymer for delivering bioactive components", *Proc. of IEEE Microtech. in Med. And Bio.*, pp. 143-146, 2005.
- [61] J. C. Sanchez, N. Alba, T. Nishida, C. Batich and P. R. Carney, "Structural modifications in chronic microwire electrodes for cortical neuroprosthetics: A case study", *IEEE Trans. on Neural systems and rehabilitation Eng.*, pp. 217-221, 2006.

- [62] H. P. Neves and P. Ruther, "The neuroprobes project", *Proc. of the IEEE EMBS*, pp. 6442-6444, 2007.
- [63] J. Chen and K. D. Wise, "A multichannel neural probe for selective chemical delivery at the cellular level," *IEEE Trans. Biomed Eng.*, v. 44, no. 8, pp. 760-769, 1997.
- [64] L. Lin and A. P. Pisano, "Silicon processed microneedles," *IEEE J. Micromech. Syst.*, v.8, no.1, pp. 78-84, 1999.
- [65] N. H. Talbot and A. P. Pisano, "Polymolding: two wafer polysilicon micromolding of closed-flow passages for microneedles and microfluidic devices," *Tech. Dig. IEEE Solid-State Sens. Actuator Workshop*, pp. 265-268, 1998.
- [66] J. D. Brazzle, I. Papautsky, A. B. Frazier, "Fluid-coupled hollow metallic micromachined needle arrays," *Proc. SPIE Conf. Microfluidic Dev. Syst.*, pp.116-124, 1998.
- [67] A.J. Bard and L. R. Faulkner, *Electrochemical methods: Fundamentals and applications*, John Wiley & Sons. Inc., 2001.
- [68] J. Wang, *Analytical Electrochemistry*, Wiley-VCH, 2000.
- [69] D. T. Fagan, I. F. Hu and T. Kuwana, "Vacuum heat treatment for activation of glassy carbon electrodes," *Anal. Chem.*, v. 57, pp. 2759-2763, 1985.
- [70] G. M. Swain, "The susceptibility of surface corrosion in acidic fluoride media: a comparison of diamond, HOPG, and glassy carbon electrodes," *J. Electrochem. Soc.*, v. 141, no. 12, pp. 3382-3393, 1994.
- [71] T. N. Rao, I. Yagi, T. Miwa, D. A Tryk and A. Fujishima, "Electrochemical oxidation of NADH at highly boron-doped diamond electrodes," *Anal. Chem.*, v. 71, pp. 2506-2511, 1999.
- [72] R. Declements and G. M. Swain, "The formation and electrochemical activity of microporous diamond thin film electrodes in concentrated KOH," *J. Electrochem. Soc.*, v. 144, pp. 856-866, 1997.
- [73] Y. V. Pleskov, "Synthetic diamond in electrochemistry," *Russian Chemical Reviews*, v. 68, no. 5, pp. 381-392, 1999.
- [74] H. B. Martn, A. Argoitia, U. Landau, A. B. Anderson and J. C. Angus, "Hydrogen and oxygen evolution on boron-doped diamond electrodes," *J. Electrochem. Soc.*, v. 143, no. 6, pp 133-136, 1996.
- [75] P. A. Michaud, E. Mahe, W. Haenni, A. Perret and C. Cominellis, "Preparation of peroxydisulfuric acid using boron-doped diamond thin film electrodes", *Electrochem. Solid-State Lett.*, v. 3, pp.77-79, 2000.
- [76] J. Wang, G. Chen and M. P. Chatrathi, "Microchip capillary electrophoresis coupled with a boron-doped diamond electrode-based electrochemical detector," *Anal. Chem.*, v. 75, pp. 935-939, 2003.
- [77] B. V. Sarada, T. N. Rao, D. A Tryk and A. Fujishima, "Electrochemical oxidation of histamine and serotonin at highly boron-doped diamond electrodes," *Anal Chem.*, v. 72, pp. 1632-1638, 2000.
- [78] O. Herlambang, B. V. Sarada, T. N. Rao and A. Fujishima, "Miniaturization of diamond microsensor system for in vivo detection", *Proc. of the Chemical Sensor*, v. 18, pp. 121-123, 2002.

- [79] S. Xie, G. Shafer, C. G. Wilson and H. B. Martin, "In vitro adenosine detection with a diamond-based sensor," *Diamond & related material*, v. 15, pp. 225-228, 2005.
- [80] J. M. Halpern, S. Xie, G. P. Sutton, B. T. Higashikubo, C. A. Chestek, H. Lu, H. J. Chiel and H. B. Martin, "Diamond electrode for neurodyanmice studies in *Aplysia californica*," *Diamond & related material*, v. 15, pp.183-187, 2006.
- [81] A. K. Engel, C. K. E. Moll, I. Fried and G. A. Ojemann, "Invasive recordings from the human brain: clinical insights and beyond", *Nature review: neuroscience*, v. 6, pp. 35- 47, 2005.
- [82] P.Mitra, C. R. Keese and I. Giaever, "Electrical measurements can be used to monitor the attachment and spreading of cells in tissue culture", *BioTechniques*, v. 11, pp. 504-510, 1991.
- [83] Y. Jimbo and A. Kawanna, "Electrical stimulation of cultured neural cells by planar electrode array", *Proc. of IEEE Eng. in Med. And Bio. Soc.*, v. 12, pp. 1741-1742, 1990.
- [84] G. W. Gross, E. Rieske, G. W. Kreutzberg and A. Meyer, "A new fixed-array multi-electrode system designed for long-term monitoring of extracellular single unit neuronal activity in vitro", *Neuroscience Lett*. V. 6, pp. 101-105, 1977.
- [85] J. E. B. Randles, "Kinetics of rapid electrode reactions. Part 3. – electron exchange reactions," *KW Somerton Trans. of the Faraday Society*, v. 48, pp. 937-950, 1952.
- [86] <http://www.lhsc.on.ca/critcare/ucicu/educate/orient/neuroap.htm>
- [87] D. T. Kewley, M. D. Hills, D. A. Borkholder, I. E. Opris, N. I. Maluf, C. W. Storment, J. M. Bower and G. T. A. Kovacs, "Plasma-etched neural probe", *Sensors and Actuators A*, v. 58, pp. 27-35, 1997.
- [88] [www.plexoninc.com](http://www.plexoninc.com)
- [89] K. D. Wise, A. M. Sodagar, Y. Yao, M. N. Gulari, G. E. Perlin and K. Najafi, "Microelectrode, microelectronics, and implantable neural microsystems", *Proc. of the IEEE*, v. 96, no. 7, pp. 1184-1202, 2008.
- [90] C. Nicholson, "Diffusion and related transport mechanisms in brain tissue", *Rep Prog Phys*, v. 64, pp. 815-884, 2001.
- [91] D. R. Wur, J. L. Davidson, W. P. Kang and D. L. Kinser, "Polycrystalline diamond pressure sensor", *J. of MEMS*, v. 4, no. 1, pp. 34-41, 1995.
- [92] X. Zhu, D. M. Aslam, Y. Tang, B. H. Stark and K. Najafi, "The Fabrication of all-diamond packaging panels with built-in interconnects for wireless integrated microsystems", *J. of MEMS*, v. 13, no. 3, 2004.
- [93] A. Aleksov, M. Kubovic, M. Kasu, P. Schmid, D. Grobe, S. Ertl, M. Schreck, B. Stritzker and E. Kohn, "Diamond-based electronic for RF applications", *Diamond & Related Materials*, v. 13, pp. 233-240, 2004.
- [94] T. Ando, X. Li, S. Nakao, T. Kasai, M. Shikida and K. Sato, "Effect of crystal orientation fracture strength and fracture toughness of single crystal silicon," *Proc. of Int. Conf. on MEMS*, pp. 177-180, 2004.
- [95] T. Ando, X. Li, S. Nakao, H. Tanska, M. Shikida, K. Sato, "Fracture toughness measurement of thin-film silicon," *Fatigue & fracture of engineering materials and structure*, v. 28, no. 8, pp. 687-694, 2005.

- [96] S. Kamiya, M. Sato, M. Saka and H. Abe, "Fracture toughness estimation of thin chemical vapor deposition diamond films based on the spontaneous fracture behavior on quartz glass substrates," *J. Appl. Phys.*, v. 81, no. 12, pp. 6056-6061, 1997.
- [97] M. D. Drory, R. H. Dauskardt, A. Kant and R. O. Ritchie, "Fracture of synthetic diamond", *J. Appl. Phys.*, v. 78, pp. 3083-3088, 1995.
- [98] I. Dion, C. Baquey, J.R. Monties, "Diamond: the biomaterial of the 21st century?" *Int. J. Artif. Organs*, v.16, 623-627, 1993.
- [99] R. F. Davis, *Diamond films and coatings: Development, properties, and applications*, Noyes Publications, pp. 1-30, 1993.
- [100] D. P. Dowling, P. V. Kola, K Domelly and T. C. Kelly, "Evaluation of diamond-like carbon coated orthopaedic implants", *Dia. Rel. Mat.*, no. 6, pp. 380-393, 1997.
- [101] S. Affatato, M. Frigo, A. Toni, "An in vitro investigation of diamond-like carbon as a femoral head coating", *J. Biomed. Mat. Res.*, no. 53, pp. 221-226, 2000.
- [102] T. Tatsuma, H. Mori and A. Fujisjhma, "Electron transfer from diamond electrode to heme peptide and peroxidase", *Ana. Chem.*, v. 72, pp. 2919-2924, 2000.
- [103] W. Yang, J. E. Butler, J. N. Russell and R. J. Hamers, "Direct electrical detection of antigen-antibody binding on diamond and silicon substrates using electrical impedance spectroscopy", *The Analst*, v. 132, pp. 296-306, 2007.
- [104] A. Lettington and J. W Steeds, *Thin film diamond*, Chapman and Hall, pp. 117-125, 1994.
- [105] M. Pinneo, "Diamond growth: Today and tomorrow", *Proc. of the 1st general conf. on Nanotechnology*, pp. 147-172, 1995.
- [106] L. Tang, C. Tsai, W.W. Gerberich, L. Kruckeberg, D.R. Kania, "Biocompatibility of chemical-vapor-deposited diamond," *Biomaterials*, v. 16, pp. 483-488, 1995.
- [107] J. Grabarczk, D. Batory, P. Louda, P. Couvrat, I. Kotela and K. Bakowicz-Mitura, "Carbon coatings for medical implants", *J. of Achievements in Mat. and Manuf. Eng.*, v. 20, pp. 107-110, 2007.
- [108] R. A. Freitas, *Nanomedicine, Vol IIA: Biocompatibility*, Landes Bioscience, 2003.
- [109] R. Hauert, "A review of modified DLC coatings for biological applications", *Dia. and Rel. Mat.*, v. 12, pp. 583-589, 2003.
- [110] A. Grill, "Diamond-like carbon coatings as biocompatible materials-an overview", *Dia. and Rel. Mat.*, v.12 , pp. 166-170, 2003
- [111] M. Amaral, P. S. Gomes, M. A. Lopes, J. D. Santos, R.F. Silva and M. H. Femandes, "Nanocrystalline diamond as a coating for joint implants: cytotoxicity and biocompatibility assessment", *J. of Nanomaterials*, accepted, 2008.
- [112] G. M. Swain, A. B. Anderson, J. C. Augus, "Application of diamond thin films in electrochemistry," *MRS bulletin*, v.23, no. 9, pp. 56-60, 1998.
- [113] J. A. Bennett, J. Wang, Y. Show and G. M. Swain, "Effect of sp<sup>2</sup>-bonded nondiamond carbon impurity on the response of boron-doped polycrystalline diamond thin-film electrodes", *J. of the Electrochem. Soc.*, v. 151, no.9, pp. 306-313, 2004.
- [114] J. Xu, Q. Chen and G. M. Swain, "Anthraquinedisulfonate electrochemistry: A comparison of glassy carbon, hydrogenated glassy carbon, highly oriented

- pyrolytic graphite, and diamond electrodes," *Anal. Chem.*, v. 70, pp. 3146-3154, 1998.
- [115] A. Fujishima, Y. Einaga, T. N. Rao and D. A. Tryk, *Diamond electrochemistry*, Elsevier, 2005.
- [116] A. A. Morrish and P. E. Pehrsson, "Effects of Surface Pretreatments on Nucleation and Growth of Diamond Films on a Variety of Substrates," *Appl. Phys. Lett.*, vol. 59, pp. 417-419, 1991.
- [117] L. Demuynck, J. C. Arnault, C. Speisser, R. Polini and F. LeNormand, "Mechanisms of CVD diamond nucleation and growth on mechanically scratched and virgin Si(100) surfaces," *Diamond and Related Materials*, vol. 6, pp. 235-239, 1997.
- [118] P. A. Dennig, H. Shiomi, D. A. Stevenson and N. M. Johnson, "Influence of Substrate Treatments on Diamond Thin-Film Nucleation," *Thin Solid Films*, vol. 212, pp. 63-67, 1992.
- [119] E. J. Bienk and S. S. Eskildsen, "The Effect of Surface Preparation on the Nucleation of Diamond on Silicon," *Diam. and Rel. Mat.*, vol. 2, pp. 432-437, 1993.
- [120] F. S. Lauten, Y. Shigesato and B. W. Sheldon, "Diamond Nucleation on Unscratched SiO<sub>2</sub> Substrates," *Appl. Phys. Lett.*, vol. 65, pp. 210-212, 1994.
- [121] M. J. Chiang and M. H. Hon, "Positive dc bias-enhanced diamond nucleation with high CH<sub>4</sub> concentration," *Diam. and Rel. Mat.*, vol. 10, pp. 1470-1476, 2001.
- [122] [28] M. D. Irwin, C. G. Pantano, P. Gluche and E. Kohn, "Bias-enhanced nucleation of diamond on silicon dioxide," *Appl. Phys. Lett.*, vol. 71, pp. 716-718, 1997.
- [123] A. Masood, M. Aslam, M. A. Tamor and T. J. Potter, "Techniques for Patterning of CVD Diamond Films on Non-Diamond Substrates," *J. of the Electrochemical Society*, vol. 138, pp. L67-L68, 1991.
- [124] G. S. Yang, M. Aslam, K. P. Kuo, D. K. Reinhard and J. Asmussen, "Effect of Ultrahigh Nucleation Density on Diamond Growth at Different Growth-Rates and Temperatures," *J. of Vacuum Science & Technology B*, vol. 13, pp. 1030-1036, 1995.
- [125] A. P. Malshe, R. A. Beera, A. A. Khanolkar, W. D. Brown and H. A. Naseem, "Initial results of a novel pre-deposition seeding technique for achieving an ultra-high nucleation density for CVD diamond growth," *Diam. and Rel. Mat.* vol. 6, pp. 430-434, 1997.
- [126] Y. X. Tang and D. M. Aslam, Polycrystalline diamond technology and piezoresistive sensor application for cochlear prosthesis, *Ph.D. Thesis*, Michigan State University, 2006.
- [127] K. Hermansson, Ulf Lindberg, Bertill Hok and Goran Plamskog, "Wetting properties of silicon surfaces", *IEEE Int. Conf. on Solid-state Sensors and Actuators*, pp. 193-196, 1991
- [128] E. Snidero, D. Tromson, C. Mer, P. Bergonzo, J. S. Foord, C. Nebel, et al., "Influence of the postplasma process conditions on the surface conductivity of hydrogenated diamond surfaces," *J. of Applied Physics*, vol. 93, pp. 2700-2704, 2003.

- [129] J. Ristein, M. Riedel, F. Maier, B. F. Mantel, M. Stammer and L. Ley, "Surface doping: a special feature of diamond," *J. of Physics-Condensed Matter*, vol. 13, pp. 8979-8987, 2001.
- [130] M. I. Lanstrass and K. V. Ravi, "Resistivity of chemical vapor deposited diamond films", *Appl. Phys. Lett.*, v. 55, no. 10, pp. 975-977, 1989.
- [131] B. J. Lee, B. T. Ahn, J. K. Lee, Y. J. Baik, "A study on the conduction path in undoped polycrystalline diamond films", *Diamond and Related Materials*, v. 10, *Appl. Phys. Lett.*, pp. 2174-2177, 2001.
- [132] M. C. Rossi, "Micro-Raman fingerprint of grain boundary in [100] oriented diamond films stress distribution and diamond phases", *Appl. Phys. Lett.*, v. 73, no. 9, 1998.
- [133] Y. Ando, Y. Niishibayashi, K. Kobashi, T. Hirao and K. Oura, "Smooth and high-rate reactive ion etching of diamond", *Diam. and Rel. Mat.*, v. 11, pp. 824-827, 2002.
- [134] I. Bell, M. K. Fung, W. J. Zhang, K. H. Lai, Y. M. Wang, Z. F. Zhou, R. K. W. Yu, C. S. Lee and S. T. Lee, "Effects at reactive ion etching of CVD diamond", *Thin Solid Films*, v. 368, pp. 222-226, 2000.
- [135] G. F. Ding, H. P. Mao, Y. L. Cao, Y. H. Zhang, X. Yao and X. L. Zhao, "Micromachining of CVD diamond by RIE for MEMS applications", *Dia. and Rel. Mat.*, v. 14, pp. 1543-1548, 2005.
- [136] O. Dorsch, M. Werner and E. Obermeier, "Dry etching of undoped and boron doped polycrystalline diamond films", *Diam. and Rel. Mat.*, v. 4, pp. 456-459, 1995.
- [137] Z. L. Cao, H. Y. Chan and D. M. Aslam, "Diamond technology", in preparation
- [138] H. -Y. Chan, D. M. Aslam, S. Wang, G. M. Swain and K. D. Wise, "Fabrication and testing of a novel all-diamond neural probe for chemical detection and electrical sensing applications," *Proc. of Int. Conf. on MEMS*, pp. 244-247, 2008
- [139] Y. Tang and D. M. Aslam, "Technology of polycrystalline diamond thin films for microsystems applications", *J. Vac. Sci. Tech.*, V. 3, pp. 1088-1095, 2005.
- [140] B. J. Polk, A. Stelzenmuller, G. Mijares, W. MacCrehan and M. Gaitan, "Ag/AgCl microelectrodes with improved stability for microfluidics", *Sensors and Actuators B*, v. 114, pp. 239-247, 2006.
- [141] T. Matsumoto, A. Ohashi and N. Ito, "Development of a micro-planar Ag/AgCl quasi-reference electrode with long-term stability for an amperometric glucose sensor", *Anal. Chim. Acta*, v. 462, pp. 253-259, 2002.
- [142] J. S. Lee, S. D. Lee, G. Cui, J. J. Lee, J. H. Shin, G. S. Cha and H. Nam, "Hydrophilic polyurethane coated silver/silver chloride electrode for the determination of chloride in blood", *Electroanalysis*, v. 11, pp. 260-267, 1999.
- [143] L. Y. Huang, R. S. Huang and L. H. Lo, "Improvement of integrated Ag/AgCl thin-film electrodes by KCl-gel coating for ISFET applications", *Sens. Actuators B*, v. 94, pp. 53-64, 2003.
- [144] M. A. Nolan, S. H. Tan and S. P. Kounaves, "Fabrication and characterization of a solid state reference electrode for electroanalysis of natural waters with ultramicroelectrode", *Anal. Chem.*, v. 69, pp. 1244-1247, 1997.
- [145] A. J. Bard and L. R. Faulkner, *Electrochemical methods: fundamentals and applications*, Wiley Publishers, 2000.

- [146] J. Xu, Q. Chen and G. M. Swain, "Anthraquinonedisulfonate electrochemistry: A comparison of glassy carbon, hydrogenated glassy carbon, highly oriented pyrolytic graphite, and diamond electrodes," *Anal. Chem.*, v. 70, pp. 3146-3154, 1998.
- [147] R. Ramesham and M. F. Rose, "Cyclic voltammetric, a. c. and d. c. polarization behavior of boron-doped CVD diamond," *Thin Solids Films*, v. 300, pp. 144-153, 1997.
- [148] A. Fujishima, Y. Einaga, T. N. Rao and D. A. Tryk, *Diamond electrochemistry*, Elsevier, 2005.
- [149] J. D. Weiland, "Electrochemical properties of iridium oxide stimulating electrodes," *Ph.D. dissertation*, University of Michigan, 1997
- [150] L. S. Robbless, J. L. Lefko and S. B. Brummer, "Activated Ir: An electrode suitable for reversible charge injection in saline solution," *J. Electrochem. Soc.*, v. 130, no. 3, pp. 731-732, 1983
- [151] V. S. Polikov, P. A. Tresco, W. M. Reichert, "Response of brain tissue to chronically implanted neural electrodes," *J. of Neuroscience Method*, v. 148, pp. 1-18, 2005
- [152] G. M. Swain, *Lecture note*, Michigan State University.